EVOLUTION OF FAULT STRENGTH FROM MICROSCOPIC ASPERITY SCALE TO MACROSCOPIC FAULT ZONE SCALE

by

JIANGZHI CHEN

A DISSERTATION

Presented to the Department of Geological Sciences
and the Graduate School of the University of Oregon
in partial fulfillment of the requirements
for the degree of
Doctor of Philosophy

September 2014

DISSERTATION APPROVAL PAGE

Student: Jiangzhi Chen

Title: Evolution of Fault Strength from Microscopic Asperity Scale to Macroscopic Fault Zone Scale

This dissertation has been accepted and approved in partial fulfillment of the requirements for the Doctor of Philosophy degree in the Department of Geological Sciences by:

Alan Rempel	Chair
Eugene Humphreys	Core Member
David Schmidt	Core Member
James Isenberg	Institutional Representative

and

J. Andrew Berglund	Dean of the Graduate School

Original approval signatures are on file with the University of Oregon Graduate School.

Degree awarded September 2014

DISSERTATION ABSTRACT

Jiangzhi Chen

Doctor of Philosophy

Department of Geological Sciences

September 2014

Title: Evolution of Fault Strength from Microscopic Asperity Scale to Macroscopic Fault Zone Scale

Fault strength is of key importance to geological and geophysical processes over a vast range of scales, from the microscopic interactions at asperities to the macroscopic behavior of plates. In this dissertation, I present my work on the evolution of fault strength. I first use a micromechanical model of flash heating that describes how shear resistance evolves at the asperity scale as a result of distributed deformation over a weak layer that grows during the brief lifetime of each asperity contact. The model predicts that after the initial rate-weakening stage, the friction becomes rate-strengthening. A comparison with published experimental data from a range of mineral systems shows good agreement with the model predictions. The parameter choices that ensure good model fits to the laboratory friction data are consistent with a priori estimates for the onset of asperity melting at high contact normal stresses. Next, considering the role of friction in fluid-saturated gouge, a linear stability analysis shows that rate-strengthening friction favors broader shear zone widths that lower strain rate for a given total slip rate. However, geologic and laboratory observations suggest that finite shear zones can persist even with rate-weakening friction. I describe a model that incorporates the interactions between variations in pore pressure of saturated porous media and the localization-pressurization phenomenon. During co-seismic slip in a plane-strain configuration, the stress variation caused by poroelasticity promotes the mechanical instability of previously undeformed

regions. The frictional strength varies throughout the mechanically unstable region. To maintain momentum balance during slip, I argue that multiple transient slip events must take place to accommodate the overall macroscopic shear. I introduce a strain-rate function that describes the overall influence on energy dissipation and fault strength as the model shear zone thickness expands. The model is used to predict the evolution of shear zone thickness, temperature, pore pressure, and fault strength during model earthquakes along a mature fault. These two components of my dissertation build from the very small scale of asperities, to granules, and finally to the finite shear zones that are observed in the fields.

This dissertation includes previously published and unpublished co-authored material.

CURRICULUM VITAE

NAME OF AUTHOR: Jiangzhi Chen

GRADUATE AND UNDERGRADUATE SCHOOLS ATTENDED:

University of Oregon, Eugene, OR
Peking University, Beijing, China

DEGREES AWARDED:

Doctor of Philosophy, University of Oregon, 2014
Bachelor of Science, Peking University, 2008

AREAS OF SPECIAL INTEREST:

Coseismic fault mechanics
Subduction zone processes
Numerical modelling of geological process

PROFESSIONAL EXPERIENCE:

Graduate Teaching Fellow, University of Oregon, 2008–2014

PUBLICATION:

Chen, J. and Rempel, A.W., 2014, Progressive flash heating and the evolution of high-velocity rock friction. *Journal of Geophysical Research: Solid Earth*.

ACKNOWLEDGMENTS

I wish to thank all those who helped me. Without them, I could not have survived the six-year long Ph.D. program.

Alan Rempel not only served as my supervisor but also encouraged and challenged me throughout my academic program. He and other committee members, Gene Humphreys and David Schmidt, provided valuable help in my dissertation.

I also want to thank Randy, Rob, Max, and past student Stephenie Weaver, who gave useful suggestion for my projects. A special thanks to the department staff, Shari and Dave.

Most especially to my family on the other side of the Pacific ocean, for their understanding, encouraging, and heart-warming chat through the internet.

For my family, who warmed my heart in all these years.

TABLE OF CONTENTS

Chapter Page

LIST OF FIGURES

Figure Page

LIST OF TABLES

CHAPTER I

INTRODUCTION

The evolution of fault strength during the coseismic and interseismic period has long been a critical question for geologists and seismologists. Better understanding of fault strength will greatly facilitate the study on the earthquake initialization, rupture propagation, and aseismic slip. In the plate scale, the fault strength plays a important role in plate bending, and determines the strength of the lithosphere.

To explain fault strength evolution, researchers have devoted much effort toward this goal ever since the birth of modern seismology. Field observations of exhumed fault cross-sections provide first-hand information on the geometry and petrology of the core and surrounding rocks ruptured during previous earthquakes; laboratory examinations of samples from these faults give detailed data that help to constrain the temperature and pressure during earthquakes. Numerical models are needed to provide further insight and help to interpret observations from the field and the laboratory. In this dissertation, I present my contribution to the field, with the aim of interpreting the results from field and laboratory studies for which previous theories have difficulty providing simple and consistent explanations. I start from a micro-mechanical model of shear resistance at the asperity scale, and then advance the work to the macroscopic evolution of fault strength

The strength of faults first emerged as a key topic after the elastic rebound theory was proposed. When the accumulated strain is large enough to overcome the strength

somewhere along a fault, an earthquake occurs. Whether the fault subsequently behaves as strong or weak is a critical control on seismogenic and rupture processes. The static strength of fault rocks is typically quite strong. But the lack of high thermal anomalies evidence from temperature measurements near faults suggests that faults are weakened during earthquakes. In Chapter II, I describe a new model that treats the shear resistance of a contact surface as the collective effect of the strength of numerous asperities. Unlike previous models, this model is built upon a relatively rigorous physical setup that accounts for material properties and phase behavior that can, in principle, be measured, and reveals key information about the parameters that controls the contact strength. To test this model, I fit the model with published experimental data of several rocks to constrain some parameters, which were found to be consistent with a priori estimates. This model offers new insights on the strength evolution of the contact surfaces.

Fault strength, however, is not the same as the strength of a contact surface. The fault shears over a zone that consists of granules ($\sim 10^{-3}$ m), where the friction between the granules are determined by the strength of the asperities ($\sim 10^{-6}$ m). The strength of a fault is also affected by the increase of pore fluid pressure caused by the expanded fluid. In Chapter III, I analyze the porothermoelastic effects, incorporate them together with the Mohr-Coulomb criterion and develop a model that predicts the evolution of shear zone width. I use this treatment to simulate the evolution of the temperature, pore pressure, and strength along a fault. This model predicts that the shear zone can expand during an earthquake, which lowers the maximum temperature on the fault. The high pore pressures developed in this model are especially relevant to the conditions along subdution zones, and the modeled results are consistent with the lack of observations of frictional melt, as well as with the recent observations from the drill core samples of the Tohoku-Oki fault zone.

A natural extension of this work will involve applying the fault strength evolution to

a plate scale ($> 10^3$ m) and simulating the outcome for comparison with observations. The Cascadia subduction zone is an excellent test-bed for such work. I am working on a project focused on using finite element modeling to study the stress variation of the Cascadia subduction interface, which is supervised by Eugene Humphreys. At present this work is not yet sufficiently polished for the implementation of a fault strength model, and the preliminary technical details are summarized in Appendix C.

Fault strength is the key connecting concept within this dissertation, which connects geophysical processes across a broad range of length scales, from the microscopic weakening of asperities, to the meso-scale of fault shear zones, and in the end to the much larger scale of the subduction interface. My dissertation contributes to the goal of improving our understanding of fault strength evolution under different conditions.

Chapter II and III are co-authored by my advisor, Alan Rempel, who offered guidance and editorial assistance throughout this work.

Chapter II was accepted by *Journal of Geophysical Research: Solid Earth*, and Chapter III is in the final stages of preparation for submission to the same journal.

CHAPTER II

PROGRESSIVE FLASH HEATING AND THE EVOLUTION OF HIGH-VELOCITY ROCK FRICTION

This chapter was accepted by *Journal of Geophysical Research: Solid Earth* and was published in April 2014. I was the leading author, doing the model development, theoretical analysis, numerical calculation, and writing. The second author Alan Rempel served as advisors for this project, helping with model development, as well as manuscript editing. This publication came directly from my dissertation research and thus belongs in my dissertation. Along with the parts in the paper, there are some related work of this project which is not in the published version, but they will serve as useful supplementary information, which will also be included in my dissertation.

II.1. Introduction

Changes in fault strength play an important and well-established role in controlling the mechanics of earthquake nucleation and coseismic slip (Scholz, 1998), yet opportunities to place firm constraints on the underlying physical interactions are limited. Indirect evidence, such as the absence of interseismic heat anomalies along mature faults (e.g., the San Andreas) (Henyey and Wasserbu, 1971; Lachenbruch and Sass, 1980, 1992) and the stress state on and around faults inferred from hydraulic fracturing and wellbore breakouts

(Zoback et al., 1987), have motivated investigations into weakening mechanisms that would reduce fault strength at the high slip rates that characterize earthquakes. Since the heat produced during coseismic slip is expected to cause large temperature increases, much theoretical effort has been devoted toward understanding potential weakening mechanisms that have a thermal origin (e.g., Bowden and Thomas, 1954; Lachenbruch, 1980; Rice, 2006; Sibson, 1973). Indeed, field geologists have long reported evidence for excessive local temperature rise, recorded in rocks that deformed during frictional heating (e.g., Holland, 1900; Scott and Drever, 1954). This has prompted numerous high-velocity rock friction (HVRF) experiments using the industrial friction-welding apparatus (e.g., Spray, 1987, 1988, 1993, 1995), rotary-shear devices (e.g., Brown and Fialko, 2012; Di Toro et al., 2004; Erismann et al., 1977; Goldsby and Tullis, 2002, 2011; Hirose and Shimamoto, 2005; Tsutsumi and Shimamoto, 1997), and other techniques (e.g., Yuan and Prakash, 2008b,a, 2012) at slip rates, durations, and normal stresses that approach conditions on faults during earthquakes. The process of "flash" heating, whereby temperatures at points of true contact can increase far above the average surface temperature gains increasing importance at such high slip speeds (e.g., Bowden and Tabor, 1950; Bowden and Thomas, 1954; Archard, 1959). Here we examine how recently published laboratory HVRF data can be used to constrain the choice of controlling parameters in a simple model for changes in the friction coefficient that result from high temperatures at microscopic asperity contacts.

Above the brittle-ductile transition zone, the macroscopic fault strength that resists coseismic slip is the net consequence of the resistance to shear along numerous asperities where true contact between the sliding surfaces is achieved (e.g., Bowden and Tabor, 1950; Dieterich and Kilgore, 1994; Logan and Teufel, 1986; Scholz, 1998). Our focus is on examining how alterations to this bulk frictional behavior can result from localized heating and weakening (Rice, 1999, 2006; Rempel, 2006; Beeler et al., 2008; Goldsby and Tullis, 2011; Brown and Fialko, 2012). In detail, weakening at highly-stressed contacts

might be attributed to the transient growth of melt layers (Rempel and Weaver, 2008; Brown and Fialko, 2012), solid-state transitions that produce weaker mineral phases (Kohli et al., 2011), or enhanced plastic yielding at elevated temperatures (Brown and Fialko, 2009). Though not necessarily requiring such extreme temperatures, mechanical lubrication by silica gel (Di Toro et al., 2004; Goldsby and Tullis, 2011) or nanoparticles (Han et al., 2011) that form as a result of high-speed comminution are also expected to lower the local friction coefficient, and may produce macroscopic frictional behavior that is similar to that caused by other "flash" processes.

Building upon the pioneering work of earlier experiments that were largely aimed at investigating how sliding surfaces become coated with through-going frictional melts (see Spray, 2010, for a review), recent advances have made it possible to conduct controlled rock friction experiments at the high slip velocities that are typical of coseismic deformation. Most HVRF experiments use initially cohesive, cylindrical samples that are often comminuted during shear to form an intervening gouge layer as the change in friction coefficient is measured (Di Toro and Pennacchioni, 2004; Di Toro et al., 2004; Hirose and Shimamoto, 2003, 2005; Del Gaudio et al., 2009; Brown and Fialko, 2012). These studies suggest that macroscopic melting across the entire slip surface occurs only after a stage of pronounced weakening that has been attributed to high flash temperatures at localized contacts. Some experiments also exhibit strengthening after the initial weakening stage (Hirose and Shimamoto, 2005; Spray, 2005; Del Gaudio et al., 2009; Yuan and Prakash, 2012; Brown and Fialko, 2012), leading to the suggestion that melt patches can smear out and increase the total contact area so that the net viscous resistance is progressively enhanced. Although we do not test this mechanism here, in Section II.4 below we briefly discuss the potential roles of some of the processes that our model neglects.

Goldsby and Tullis (2011) report the rate dependence of the macroscopic friction coefficient for several rock types at sliding velocities up to 0.36 m/s, with experimental

durations short enough that the average ambient temperature along the sliding surface remains nearly constant, and gouge generation is minimal. Here we show that this friction data are consistent with a model in which the sliding resistance begins to evolve once a threshold-weakening temperature is exceeded locally along microscopic contacts, with progressive weakening at the asperity scale controlled by distributed "viscous" deformation. Using the observed low-speed friction coefficient together with independent literature values for all other model parameters fits to the observed frictional behavior enable us to infer values for the weakening temperature, effective viscosity, and asperity size that compare favorably with a priori estimates (Rempel and Weaver, 2008). Extending calculations to higher sliding rates and/or elevated temperatures, our model predicts that the frictional rate dependence can transition from velocity weakening to become velocity strengthening, even without invoking changes to the total contact area. Instead, rate strengthening occurs in our model because the increased dissipation with slip rate is not able to cause the weakened layer to grow fast enough to produce continued reductions to the average viscous resistance over the progressively shorter contact lifetimes that characterize sufficiently elevated slip speeds.

II.2. Dimensional Analysis

It is instructive to examine the implications of dimensional constraints on the general parameter dependencies that can be expected. This helps to place earlier efforts in context before describing the details of our new model for the changes in frictional resistance that result from high flash temperatures. Our goal is to develop an understanding of the most basic set of physical interactions that can generate observed HVRF behavior, in particular the pronounced weakening that has been attributed to flash heating. To that end, for the moment we ignore complications associated with gouge production

and granular mechanics, before returning to discuss some potential influences of such neglected processes in the Section II.4 below.

We seek a relationship between the macroscopic effective friction coefficient μ and the sliding velocity V. Our conceptual picture hinges on the idea that the macroscopic frictional resistance results from changes in the resistance to shear at numerous asperity contacts that are heated beyond a threshold weakening temperature. Before that weakening threshold is reached, the local friction coefficient is controlled by the ratio of the contact shear strength τ_c to the asperity strength σ_c so that $f_0 = \tau_c/\sigma_c$. The energy needed to raise a unit volume of material an increment ΔT to the weakening temperature can be compared with the initial contact shear strength to obtain another dimensionless parameter $\rho C \Delta T/\tau_c$, where ρC is the heat capacity per unit volume. Energy is conducted away at a rate governed by the thermal diffusivity α, so that for asperities of characteristic size D, the dimensionless Peclet number that gauges this heat transport is VD/α.

The simplest models of flash weakening propose that at the weakening temperature the contact shear strength drops abruptly to some level τ_w and subsequently remains constant. If we identify τ_w as the seventh and final dimensional parameter that controls the system behavior together with the others listed above (i.e., V, τ_c, σ_c, $\rho C \Delta T$, α, and D), then since they are characterized by only three independent sets of units (e.g., energy, distance, and time), Buckingham's Pi theorem (e.g., Middleton and Wilcock, 1994, pp. 69–99) predicts that the macroscopic friction can be expressed as

$$\mu = g_1 \left(f_0, f_w, \rho C \Delta T/\tau_c, VD/\alpha \right), \tag{II.1}$$

where $f_w = \tau_w/\sigma_c$ and g_1 represents some as-yet undetermined functional form.

By considering the one-dimensional heat transport away from a shearing asperity contact, Rice (1999) identified

$$V_w = \frac{\pi \alpha}{D} \left(\frac{\rho C \Delta T}{\tau_c} \right)^2 \tag{II.2}$$

as the minimum sliding velocity that is required to increase the temperature by ΔT on the contact surface over its finite lifetime. Recognizing that the scaled velocity V/V_w involves a simple combination of the last two dimensionless parameters on the right side of equation (II.1), the special case adopted in many early models of flash weakening (Rice, 1999, 2006; Beeler et al., 2008) defines g_1 so that

$$\mu = f_w + (f_0 - f_w)\,\frac{V_w}{V}, \tag{II.3}$$

when $V \geq V_w$. The right side of equation (II.3) depends on only three dimensionless parameters that are combined from the four listed in the general functional form written in equation (II.1). In fact, although it is not explicit in the friction law itself, we note that the validity of the one dimensional heat transport used to define V_w also requires that the Peclet number $VD/\alpha \gg 1$ so that the thermal diffusion distance normal to the slip plane is much smaller than the asperity size.

The assumption of a constant weakened contact shear strength τ_w is sensible if the subsequent frictional resistance is controlled by sliding along a thermally weakened surface whose properties are insensitive to continued heating beyond the weakening threshold, as can be expected to result from certain solid-state phase transformations. (For example, X-ray diffraction analyses by Kohli et al. (2011) revealed the presence of the notoriously slippery mineral talc following the apparent frictional dehydration of antigorite in HVRF experiments with $V > V_w \approx 0.1$ m/s.) Perhaps more generally, one might expect the contact shear strength to evolve with further heat input that causes the weakening temperature to be reached at progressively further distances from the original slip plane. Our simple model for such changes invokes the development of a weakened layer that resists deformation in proportion to an effective viscosity η. If the energy per unit volume required to create the weakened layer is ρL, then this can be compared with the energy required to raise the temperature by ΔT to define a dimensionless Stefan

number $S = \rho L / \rho C \Delta T$. Replacing τ_w with η and ρL implies that the system is described by eight independent dimensional parameters that can be combined to describe the macroscopic friction as

$$\mu = g_2 \left(f_0, \rho C \Delta T / \tau_c, V D / \alpha, S, \alpha \rho C \Delta T / \eta V^2 \right). \tag{II.4}$$

The last dimensionless parameter in equation (II.4) motivates the definition of a characteristic velocity

$$V_p = \sqrt{\frac{\pi \alpha \rho C \Delta T}{\eta}}. \tag{II.5}$$

In the special limit where $VD/\alpha \gg 1$ and $V_w < V \ll V_p$, the simple model for "flash melting" developed by Rempel and Weaver (2008) predicts that the macroscopic friction tends toward the asymptotic form

$$\mu_s = f_0 \frac{V_w}{V} \left\{ 1 + 2S \left[\sqrt{\frac{V}{V_w}} - 1 + (1 - S) \ln \left(1 + \frac{\sqrt{\frac{V}{V_w}} - 1}{S} \right) \right] \right\}, \tag{II.6}$$

whereas when $V > V_w$ is comparable to V_p, the friction tends toward

$$\mu_l = f_0 \frac{V_w}{V} \left[1 + \frac{S V^2}{V_p^2} \left(\sqrt{1 + \frac{2 V_p^2}{S V^2} \left(\frac{V}{V_w} - 1 \right)} - 1 \right) \right]. \tag{II.7}$$

These limits compare favorably with the results of an approximate numerical treatment of weak-layer growth when the macroscopic frictional behavior is assigned from equations (II.6) and (II.7) with

$$\mu \approx \max \left(\mu_s, \mu_l \right). \tag{II.8}$$

Equation (II.8) defines a particular functional form for g_2 where the second and third dimensionless terms on the right side of equation (II.4) are combined in the form V/V_w, and the final dimensionless term is represented in the form V/V_p, so that together

with S and f_0, these are the only factors that control μ. In effect, equation (II.8) replaces an empirical parameter f_w from equation (II.3) that has a firm conceptual basis only when the high-temperature contact shear strength can be considered constant, with the combination of two parameters, S and V/V_p, that are both defined from combinations of physical properties that can be estimated from independent measurements. In the next section we describe our improved model for progressive flash heating and demonstrate its utility through comparisons with published HVRF data (Goldsby and Tullis, 2011).

II.3. A Model for Progressive Flash Heating

We seek to describe how the macroscopic friction coefficient μ is affected by the evolution of shear resistance along numerous microscopic asperity contacts that are each characterized by a time-varying local friction coefficient $f(t)$. This local friction coefficient is defined so that the contact shear strength $\tau(t) = f(t)\sigma_c$, where the normal stress σ_c is treated as constant. When the asperity temperature T is less than the weakening temperature T_w, the local friction coefficient is constant at f_0. After the weakening temperature is reached, the asperity strength decreases with the progressive development of a weakened layer (see Figure II.1). For simplicity we consider a single constant asperity size D and assume that the time spans over which the asperities in a representative fault area have been in contact t are distributed uniformly between zero and the total lifetime θ. This implies that the spatial average that defines the instantaneous macroscopic friction μ is equivalent to the temporal average of the strength of a single asperity so that (e.g., Rempel and Weaver, 2008)

$$\mu = \frac{1}{\theta} \int_0^\theta f(t)\, \mathrm{d}t, \tag{II.9}$$

where $\theta = D/V$ is the total asperity lifetime for slip at velocity V.

To evaluate equation (II.9), we must know both the time span t_w over which the

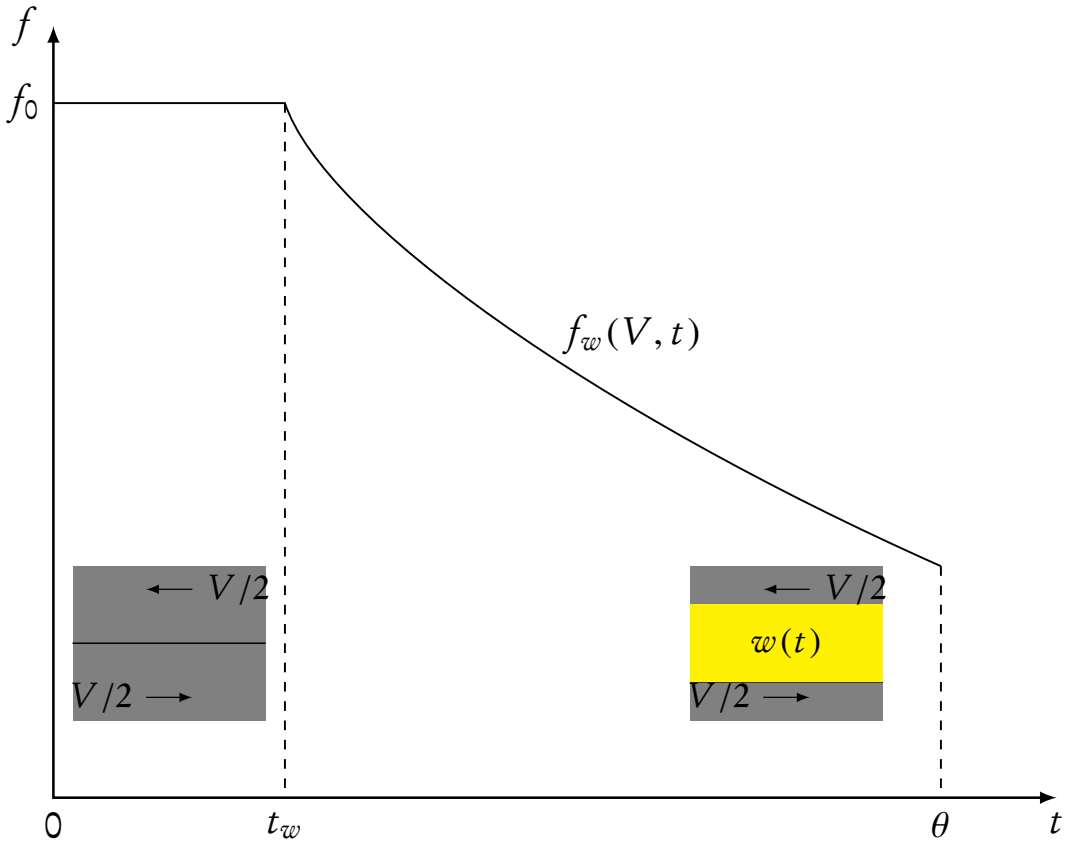

Figure II.1: A schematic diagram showing the development of a weakened layer and the consequent evolution of the local friction coefficient f over its lifetime θ. As the sliding contact time increases beyond the weakening time t_w, the thickness w of the weakened layer increases and f drops.

asperity strength is constant at $\tau_c = f_0\sigma_c$, and the subsequent evolution in thickness w of a weakened layer that deforms with shear resistance $\tau(t) = \eta V/w(t)$. In common with earlier flash-weakening models, this involves solving for the temperature evolution at the asperity scale but with the added complication that we are interested in how the flow of heat governs the growth of a weak layer after t_w. Here this growth is assumed to consume energy and limit subsequent temperature increases within the weakened layer as it expands after time t_w.

II.3.1. Weakening Onset

Consider two asperity blocks that slide in opposite directions with relative velocity V, as shown in Figure II.1. We treat the case where the sliding speed is fast enough that the thermal diffusion distance is much smaller than the asperity size (i.e., $DV/\alpha \gg 1$), so a one-dimensional treatment is appropriate for describing the heat transport. Prior to the onset of weakening, the early temperature profile varies with distance y normal to an asperity contact of strength τ_c according to (Carslaw and Jaeger, 1959, pp. 75)

$$T = T_{\text{amb}} + \frac{\tau_c V}{\alpha \rho C}\left[\sqrt{\frac{\alpha t}{\pi}}\exp\left(\frac{-y^2}{4\alpha t}\right) - \frac{y}{2}\text{erfc}\left(\frac{y}{2\sqrt{\alpha t}}\right)\right], \tag{II.10}$$

where T_{amb} is the ambient temperature and we identify $\tau_c V$ as the initial rate of heat production along the surface $y = 0$.

Previous models (e.g., Beeler et al., 2008; Rice, 2006; Rempel and Weaver, 2008) have assumed that the onset of weakening occurs when the temperature on the sliding surface reaches the weakening temperature $T_w = T_{\text{amb}} + \Delta T$, so that equation (II.10) gives the weakening time as

$$t_w \approx \frac{\pi\alpha}{V^2}\left(\frac{\rho C \Delta T}{\tau_c}\right)^2 = \frac{V_w D}{V^2}. \tag{II.11}$$

HVRF experiments seem to indicate a continuous transition from roughly constant low-speed friction to the lower values that are measured when V exceeds the weakening velocity V_w. Since we treat the resistance $\tau(t \geq t_w)$ as inversely proportional to the thickness of a weakened layer w, here we adopt a finite value for the initial weakened thickness w_0 to regularize the behavior of $f(t)$ at t_w. We note the precedent set by Sirono et al. (2006), who modeled shear heating and the development of macroscopic melt layers that were assumed to initiate at an arbitrary initial thickness chosen as $w_0 = 4.75\,\mu$m, recognizing that the late-stage behavior is not sensitive to this initial value. While the insensitivity to w_0 should also apply in our model when the contact lifetime θ greatly exceeds the weakening time t_w, the smooth transition in frictional behavior that is

observed when V is only slightly greater than V_w (so that θ and t_w remain close) suggests that w_0 be chosen more judiciously. Building upon an analogy with other systems that exhibit changes in deformation mechanisms (e.g., Brace and Kohlstedt, 1980; Hirth and Kohlstedt, 2003), we assume that the transition from frictional to viscous behavior takes place at a threshold that leads to a reduction in the resistance to shear. Accordingly, we assign $w_0 = \eta V/\tau_c$ so that a weak layer with uniform strain rate V/w_0 has the same strength as exhibited at earlier times (Rempel and Weaver, 2008) and further growth of the layer results in progressive weakening. To be consistent with this choice, we take t_w as the time at which equation (II.10) predicts the weakening temperature is reached at $|y| = w_0/2$; the required choices for w_0 are small enough in our calculations that the value of t_w determined in this way is always well-approximated by equation (II.11).

At the onset of weakening when $t = t_w$, we use equation (II.10) to describe the temperature profile outside the deforming layer for $|y| \geq w_0/2$. However, symmetry considerations require that the subsequent temperature evolution inside the deforming layer must produce no net heat flux at $y = 0$. This condition (i.e., $\mathrm{d}T/\mathrm{d}y = 0$ at $y = 0$) is incompatible with the profile given by equation (II.10) so we specify a modified temperature profile for $|y| < w_0/2$. In fact, when the development of a finite-thickness weakened layer consumes energy, as assumed here, the onset of spatially distributed shear should coincide with an abrupt drop in temperature. Moreover, in order for the weakened layer to experience monotonic growth so that the shear resistance does not momentarily increase above τ_c immediately after t_w, it is necessary that the heat flux at $\pm w_0/2$ not fall below a value consistent with the predictions of equation (II.10). Since the initial layer thickness is small, we use a Taylor series expansion to approximate the temperature profile $T(t_w, y) = T_i(y)$ for $|y| \leq w_0/2$ as

$$T_i(y) \approx T_i(0) + \frac{1}{2}\frac{\mathrm{d}^2 T_i}{\mathrm{d}\, y^2}\bigg|_{y=0} y^2 + O(y^3).$$

Truncating after the first two nonzero terms, we assign the values of T_i and its second derivative at $y = 0$ so that both the temperature and the heat flux are continuous at $\pm w_0/2$ when $t = t_w$, giving

$$T_i(y) \approx T_w + \frac{\tau_c V (w_0^2 - 4y^2)}{8\alpha\rho C w_0} \operatorname{erfc} \frac{w_0}{4\sqrt{\alpha t_w}} \tag{II.12}$$

for $|y| \leq w_0/2 = \eta V/(2\tau_c)$.

II.3.2. Frictional Evolution

For simplicity, we assume that the thermal properties are uniform and constant and that since the system is symmetric with respect to $y = 0$; it- suffices to consider only the region $y > 0$. After weakening begins, the weakened zone is characterized by thickness $w(t)$ and viscosity η. The heat production rate per unit volume is

$$Q(y,t) = \tau(t) V / w(t), \tag{II.13}$$

where the shear stress is $\tau(t) = \eta V/w(t)$. Incorporating this into the heat balance, the evolution of temperature is described by

$$\begin{aligned} &\frac{\partial T}{\partial t} = \alpha \frac{\partial^2 T}{\partial y^2} + \frac{Q}{\rho C}, \quad 0 \leq y \leq w/2 \\ \text{and} \quad &\frac{\partial T}{\partial t} = \alpha \frac{\partial^2 T}{\partial y^2}, \quad y > w/2. \end{aligned} \tag{II.14}$$

The energy per unit volume required to grow the weakened layer is taken as ρL. This implies that the layer growth-rate $\mathrm{d}w/\mathrm{d}t$ depends on the difference in conductive flux across the boundary according to

$$\frac{\rho L}{2} \frac{\mathrm{d}w}{\mathrm{d}t} = \rho C \alpha \left.\frac{\partial T}{\partial y}\right|_{y=w/2^+} - \rho C \alpha \left.\frac{\partial T}{\partial y}\right|_{y=w/2^-}. \tag{II.15}$$

Symmetry requires that the heat flux vanish at $y = 0$, while fixed temperature conditions are applied at the weakened boundary and at large y so that

$$\left.\frac{\partial T}{\partial y}\right|_{y=0} = 0, \quad T|_{y=w/2} = T_w, \quad \text{and} \quad T|_{y\to\infty} = T_{\mathrm{amb}}. \tag{II.16}$$

Equation (II.14) is solved subject to the initial conditions at t_w described above and the boundary conditions in equations (II.15) and (II.16) using the numerical scheme outlined in Appendix A. This yields predictions for the evolution of temperature and the thickness $w(t)$ of the weakened layer that are substituted into equation (II.9) while noting that $f(t > t_w) = \tau(t)/\sigma_c = [\eta V/w(t)]/(\tau_c/f_0)$ so that the macroscopic friction coefficient can be written as

$$\mu = \frac{f_0 t_w V}{D} + \frac{f_0 \eta V^2}{D\tau_c} \int_{t_w}^{D/V} \frac{\mathrm{d}t}{w(t)}, \tag{II.17}$$

when the contact lifetime $\theta = D/V > t_w$.

II.3.3. Model Parameters

We assume that T_{amb} and V are reasonably well known and can be regarded as constant over the short lifetimes of each asperity contact. The local friction coefficient f_0 that gauges strength at low contact temperatures can be inferred from friction data collected at low speeds. With these three parameters known, we are left with seven others that must be specified in order to calculate the macroscopic friction, namely: ρC, ρL, α, τ_c, T_w, η, and D. Estimates for the first four are taken from the literature and summarized in Table II.1 for a number of different sliding systems (Rempel and Weaver, 2008). The values of T_w, η, and D are considered more uncertain, so we use the fitting procedure described below to infer values that are consistent with the friction data presented by Goldsby and Tullis (2011). Table II.2 summarizes the resulting values (we treat the novaculite and quartzite as both being composed entirely of quartz) and also gives a priori property estimates from Rempel and Weaver (2008). Two sets of estimates for T_w and η are provided, with T_{wa} and η_a corresponding to the weakening temperature and viscosity based upon the melting behavior at atmospheric pressure, and $T_{w\sigma}$ and η_σ based upon the estimated melting temperature at normal stress $\sigma_c = \tau_c/f_0$.

Table II.1: Thermal and mechanical properties used in model calculations

Property	Albite	Gabbro	Granite	Quartz
ρC (MJ/m^3/°C)	2.02	3.83	3.24	1.94
ρL (MJ/m^3)	645	1026	517	392
α (mm^2/s)	0.67	0.58	0.77	2.22
τ_c (GPa)	6.5–7.1	5.0–8.3	5.6–8.0	7.3–9.4

Thermal properties are taken from Rempel and Weaver (2008) and references therein. The lower values in the ranges for τ_c are from Rempel and Weaver (2008), based on mineral hardness correlations (Broz et al., 2006; Beeler et al., 2008). The upper values in the ranges for τ_c are from nanoindentation tests described by Goldsby and Tullis (2011).

Table II.2: Parameters (S, V_w, and V_p) chosen to fit frictional data, corresponding physical properties (T_w, η, and D) inferred from these parameter choices, and a priori estimates of these properties from Rempel and Weaver (2008)

Rock	Fit Parameters			Inferred Properties			A Priori Property Estimates		
	S	V_w (m/s)	V_p (m/s)	T_w (°C)	η (Pa s)	D (μm)	$T_{wa}, T_{w\sigma}$ (°C)	η_a, η_σ (Pa s)	D (μm)
Albite	0.20	0.15	5	1620	260	3–4	1100	3.0×10^7	10–20
							1710	1.1×10^3	
Gabbro	0.19	0.09	12	1430	70	9–23	1200	1.2×10^3	10–20
							1400	29	
Granite	0.11	0.12	19	1500	30	7–14	900	1.3×10^{10}	10–20
							1800	98	
Novaculite	0.08	0.13	17	2550	120	15–24	1710	1.8×10^5	10–20
							2800	12	
Quartzite	0.08	0.08	17	2550	120	28–45	1710	1.8×10^5	10–20
							2800	12	

T_{wa} and η_a are based upon estimates of melt onset at atmospheric confining pressure $\sigma_c = \tau_c / f_0$, calculated using the lower-range values for τ_c given in Table II.1.

II.3.4. Experimental Constraints and Model Results

Figure II.2 shows comparisons between the experimental data measured for each of the five sliding systems examined by Goldsby and Tullis (2011) and the predictions of equation (II.17) calculated using the parameter values summarized in the legends. In each case, the model curve shows a monotonic decrease in μ with sliding rate V that matches the trend exhibited by the data.

For a given sliding system, in addition to f_0, only three parameters must be specified to predict the macroscopic friction at a given sliding rate V. The values of S, V_w, and V_p can be calculated from the properties listed in Table II.1 and the a priori estimates in Table II.2; however, the latter values have large uncertainties (Rempel and Weaver, 2008). To better constrain these three controlling parameters we fit the model predictions to the experimental data reported by Goldsby and Tullis (2011). For each of the five sliding systems (albite, gabbro, granite, novaculite, and quartzite) we ran a separate Monte Carlo simulation of 2000 samples. Representing S, V_w, and V_p as ψ_i, with $i = 1$, 2, or 3, the samples for ψ_i were chosen to follow a normal distribution with the mean $\bar{\psi}_i$ assigned using the averaged parameters implied by the a priori property estimates, and a standard deviation of $\sigma_{\psi i} = \bar{\psi}_i/3$. These choices were made to ensure broad coverage of parameter space while at the same time limiting the spread in the model results. The misfit Δ is the difference between the experimental results and the model predictions weighted by a moving standard deviation. If the predicted friction for sliding velocity V with N data points is $\hat{\mu}$, then the misfit Δ against the observed friction μ is defined as

$$\Delta = \frac{1}{N}\sqrt{\sum_{j=1}^{N}\left[\frac{\hat{\mu}(V_j) - \mu(V_j)}{\sigma_\mu(V_j)}\right]^2},$$

where σ_μ is the moving standard deviation of μ with a window length set to 20 for the calculations reported here.

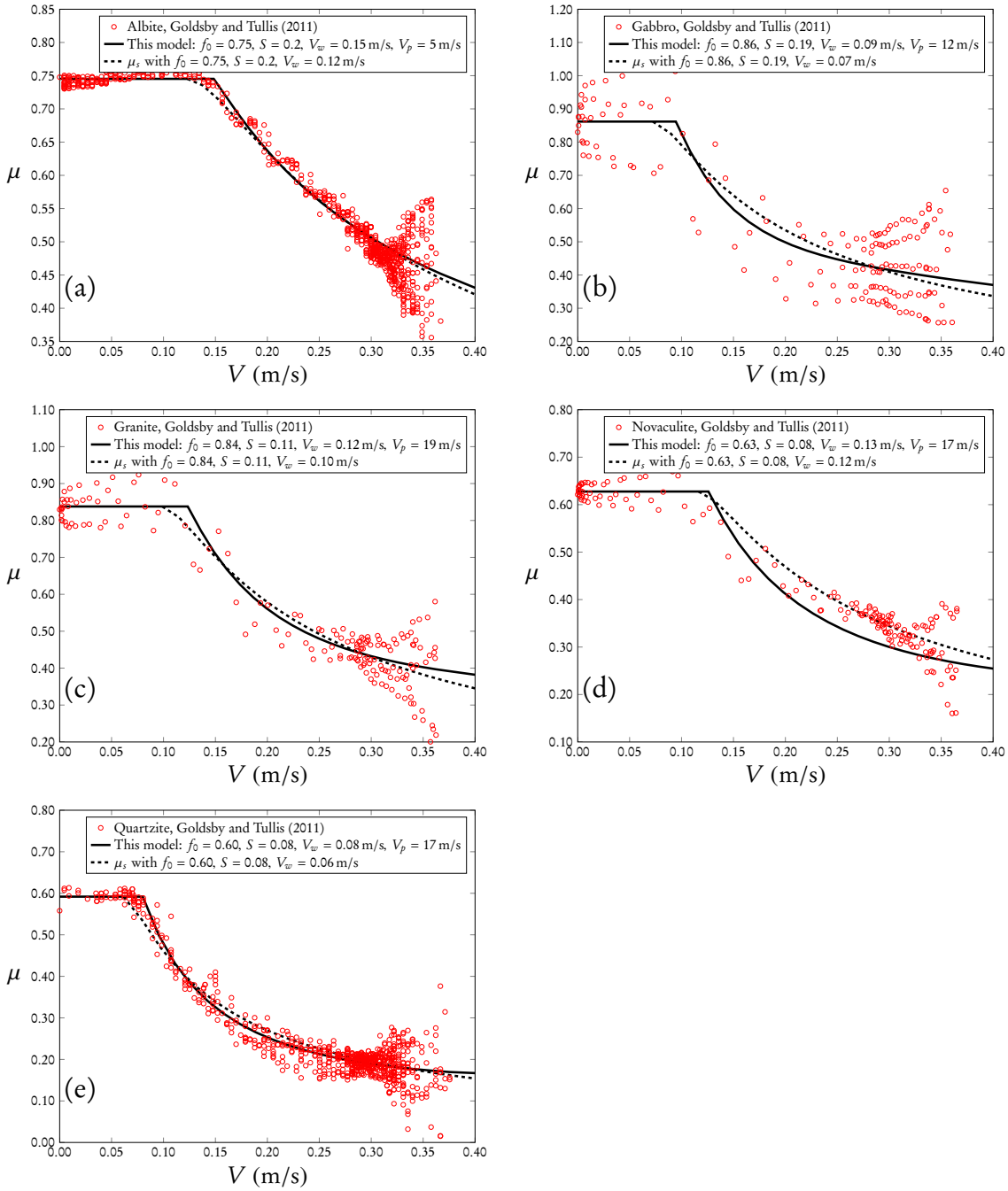

Figure II.2: Measured effective friction coefficient μ as a function of slip rate V reported by Goldsby and Tullis (2011) for (a) albite, (b) gabbro, (c) granite, (d) novaculite, and (e) quartzite. Solid lines show comparisons against our model, with values for f_0, S, V_w, and V_p given in the legend. For reference, the dashed lines show the predictions of equation (II.6) using the same Stefan numbers but smaller weakening velocities.

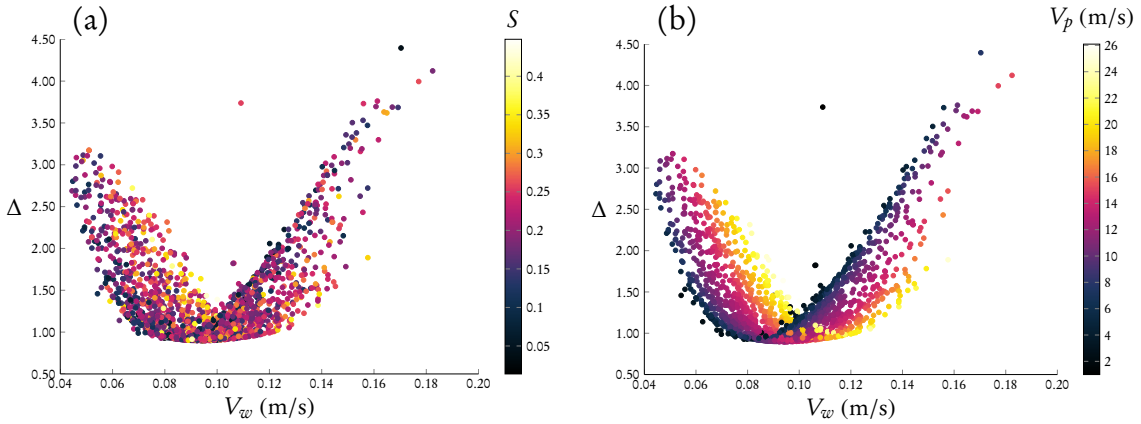

Figure II.3: The misfit for the gabbro data fit, shown as a function of V_w and color coded with (a) S and (b) V_p. The misfit is minimized when V_w is between 9 cm/s and 11 cm/s; V_p is approximately 8 –14 m/s, and S is approximately 0.15–0.25. Note that V_w is well constrained but that relatively large ranges of S and V_p can still result in a small misfit.

The values of S and V_p are not well constrained, both because only a relatively modest range of sliding velocities greater than V_w is used for our comparisons and because the standard deviation of measured frictional resistance increases when S and V_p are more important, toward the maximum slip speeds shown in Figure II.2. Indeed, Figure II.3 suggests that the simulation is robust in V_w, but that different combinations of S and V_p result in similar misfits. Acknowledging this important source of uncertainty, it is instructive to nevertheless use these fit parameters to infer values of T_w, η, and D that-are consistent with the observed frictional data given the further constraints imposed by accepting the physical property values that are summarized in Table II.1. In particular, assuming ρC and ρL are accurate, the value of S is used to infer ΔT and hence the weakening temperature T_w; we then use the value of V_w to infer the asperity size D and the value of V_p to infer the viscosity η (see Table II.2). We discuss the comparison between these best fit results and the a priori property estimates further in Section II.4 below. Figure II.4 shows the distribution of misfit Δ calculated for each sliding system in our Monte Carlo sampling of parameter space.

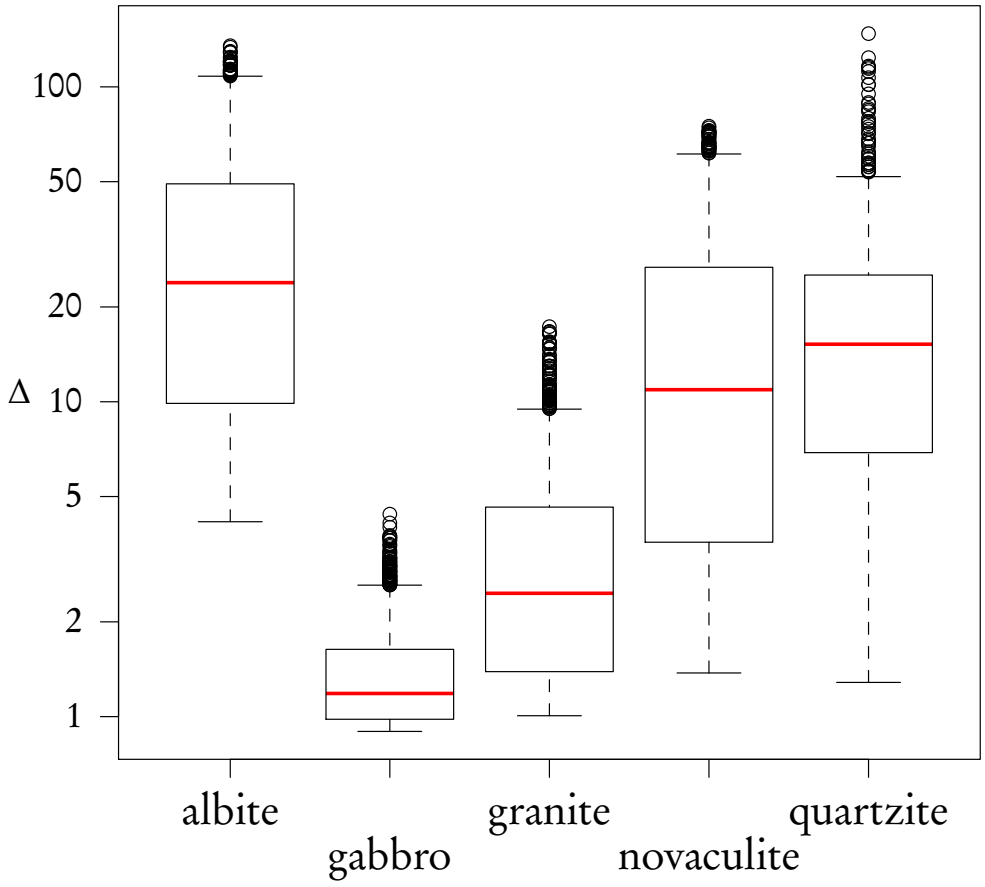

Figure II.4: Distribution of the misfit Δ for the five materials. The median is marked by the horizontal line near the center of each box, which is plotted to cover from the 25th percentile to the 75th percentile. The whiskers are drawn to encompass the range of the vast majority of misfits.

With the fit results used to constrain the controlling parameters, the model can be used to predict the behavior of $\mu(V, T)$ at higher sliding rates and ambient temperatures outside the range of laboratory values. As an example, Figure II.5a shows predictions for novaculite friction at a range of background temperatures using the best fit parameters summarized in Table II.2. The uppermost line shows the predicted extrapolation to

high slip speeds for the macroscopic friction with ambient room temperature. After V_w is exceeded, further increases in slip speed cause the heat production rate described by equation (II.13) to rise; the thickening of the weak layer that results causes μ to decrease rapidly with slip speed at first. At higher V, however, the progressive decrease in contact lifetime D/V causes the time-averaged layer thickness to actually decrease as V is increased further. Figure II.5b demonstrates that the predicted transition from rate-weakening to rate-strengthening behavior occurs at lower V when the ambient temperature T_{amb} is higher. We discuss this rate dependence further in Section II.4 below. Figure II.5c shows the evolution of the local friction $f(t)$ at different sliding velocities with $T_{\text{amb}} = 20°\text{C}$; recall that the macroscopic friction μ is defined by the average value of f and consistent with the changing areas under the curves for f, Figure II.5a shows that μ increases once the velocity exceeds a transition near 2.2 m/s.

II.4. Discussion

The model predictions shown in Figure II.2 demonstrate that distributed "viscous" deformation through weak layers that form and grow along asperity contacts can produce macroscopic frictional behavior similar to that observed experimentally. As with other models for the effects of flash heating on macroscopic friction (e.g., Rice, 1999, 2006; Rempel and Weaver, 2008; Beeler et al., 2008), in the current treatment the low-speed friction coefficient f_0 and the weakening velocity V_w exert the strongest controls on changes in μ with slip rate when V is only moderately faster than V_w.

II.4.1. Inferred Asperity-Scale Parameters

Using literature values for the volumetric heat capacities ρC, thermal diffusivities α, and contact strengths τ_c of each sliding system (see Table II.1), the only remaining

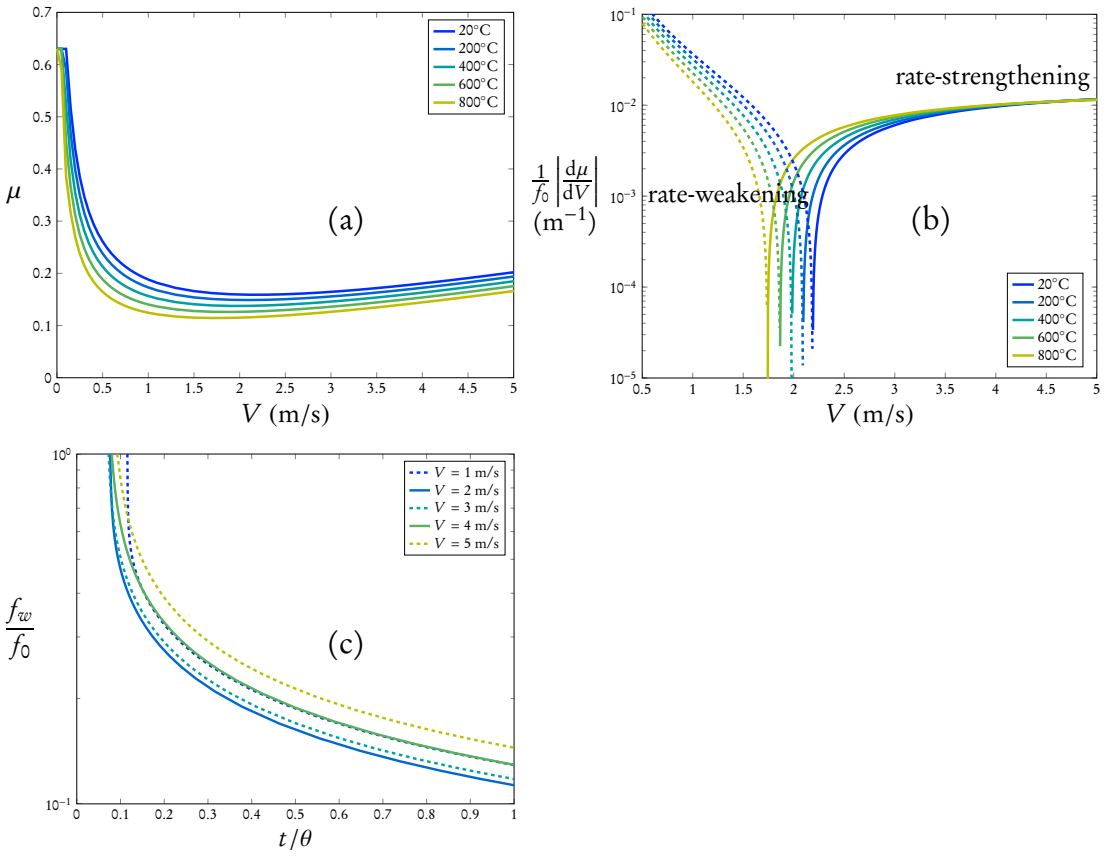

Figure II.5: (a) Modeled novaculite friction extrapolated to high slip speeds at the range of background ambient temperatures listed in the legend. (b) Rate dependence of modeled friction shown in Figure II.5a. At higher ambient temperature, the transition from rate weakening to rate strengthening occurs at a lower sliding velocity. (c) The macroscopic rate dependence is controlled by the time averaged local friction f, and is proportional to the area under each curve.

physical parameters that control the value of V_w appear as the square of the temperature rise to weakening onset divided by the asperity contact size, so that $V_w \propto \Delta T^2/D$. The energy required to grow the weak layer and its shear resistance, characterized by the effective viscosity η, imply that the Stefan number $S \propto 1/\Delta T$ and the characteristic velocity $V_p \propto \sqrt{\Delta T/\eta}$ should also influence the macroscopic friction. These parameters are admittedly less well constrained by the experiments but still enable us to examine whether the conditions at the asperity scale that can be inferred from the model are

consistent with independent estimates.

For the Stefan number, the proportionality constant relating S to $1/\Delta T$ depends linearly on the energy input needed to create the weak layer ρL. Here we follow Rempel and Weaver (2008) in quoting estimates in Table II.1 based upon the energy required to break chemical bonds and produce a melt. If the weak layer were able to grow with less energy input, the inferred ΔT values listed in Table II.2 would overestimate the actual temperature increase required for flash behavior. As listed, however, for each of the sliding systems we examined the inferred values of ΔT are close to the higher end of a priori estimates, which are based upon the expected melting behavior at confining pressure σ_c (the phase behavior of each of these systems is discussed in some detail by Rempel and Weaver (2008)). Consistent with these relatively high inferred weakening temperatures, the inferred viscosities η derived from the fitted values of V_p are close to the lower ends of the estimated ranges. For albite and granite, the inferred viscosities are actually a factor of 5 and 3, respectively, below the lowest a priori estimates, but we note that these discrepancies are small in comparison to the orders of magnitude in viscosity variations expected over a span of plausible weakening temperatures between melting at one atmosphere (1100°C for albite, 900°C for granite at the eutectic) and the estimated temperature at melt onset (1710°C and 1800°C) for $\sigma_c = \tau_c / f_0$ (8.7 GPa and 6.7 GPa) with these sliding systems. Since the viscosities of silicate melts are strongly influenced by the concentration of volatiles and other minor constituents, we view the order-of-magnitude agreement between inferred values of η and the η_σ estimates for all five sliding systems as suggestive of a high pressure melt origin for the controls on asperity strength during these experiments.

With ΔT obtained from the fit for S, the data-constrained weakening velocity is used to infer the asperity size D. By their very nature, HVRF experiments subject rock samples to extreme conditions that produce significant damage along carefully prepared sliding

surfaces. The a priori estimates for D listed in Table II.2 are nevertheless reasonably close to the inferred values from the model fits. Somewhat surprisingly, the largest of the inferred contact sizes are for novaculite and quartzite, which are both made from the mineral that is hardest at room temperature. Because the mineral content of these sliding systems is virtually the same (in Goldsby and Tullis (2011), Table S1, note that the novaculite contains minor calcite, in addition to quartz), for the model curves shown in Figures II.2d and II.2e we fixed the values of S and V_p to be identical and used our fitting procedure to choose the values of V_w that agree best with the data. Figure II.6 shows how the misfit Δ varies with D for these two sliding systems and requires that the quartzite asperities be roughly twice the dimension of the asperities inferred for the novaculite. For comparison, the quartzite grain size is listed in Goldsby and Tullis (2011), Table S1 as 2–3 mm, whereas the novaculite grain size is only 5 μm, several times smaller than the values of D inferred here. Clearly, grain size and asperity size should not be equated, and it is unclear how either relates to the typical particle diameter in the minor amounts of gouge produced by comminution during these experiments (Goldsby and Tullis, 2011). A comparison of the lower limits on Δ in Figure II.6 against the overall misfit distributions shown in Figure II.4 reveals that the quartzite fit does admit slightly lower values of Δ when S and V_p are not constrained to be consistent with the novaculite values, but the improvement is minimal. Further calculations demonstrate that as long as the parameters are chosen to place Δ within the lower 25th percentile of the distribution, the curves of $\mu(V)$ appear to be acceptable fits to the experimental data.

For consistency with the one-dimensional treatment of heat transport used here and in previous flash models, the asperity size should be large enough that the Peclet number $VD/\alpha \gg 1$. Using our inferred asperity sizes, we find that $VD/\alpha \sim 1$ at slip speeds near V_w, and in fact that for albite $V_w D/\alpha < 1$. At seismic slip rates of $V \sim 1$ m/s, the Peclet number is large enough that the heat transport should be well approximated by our

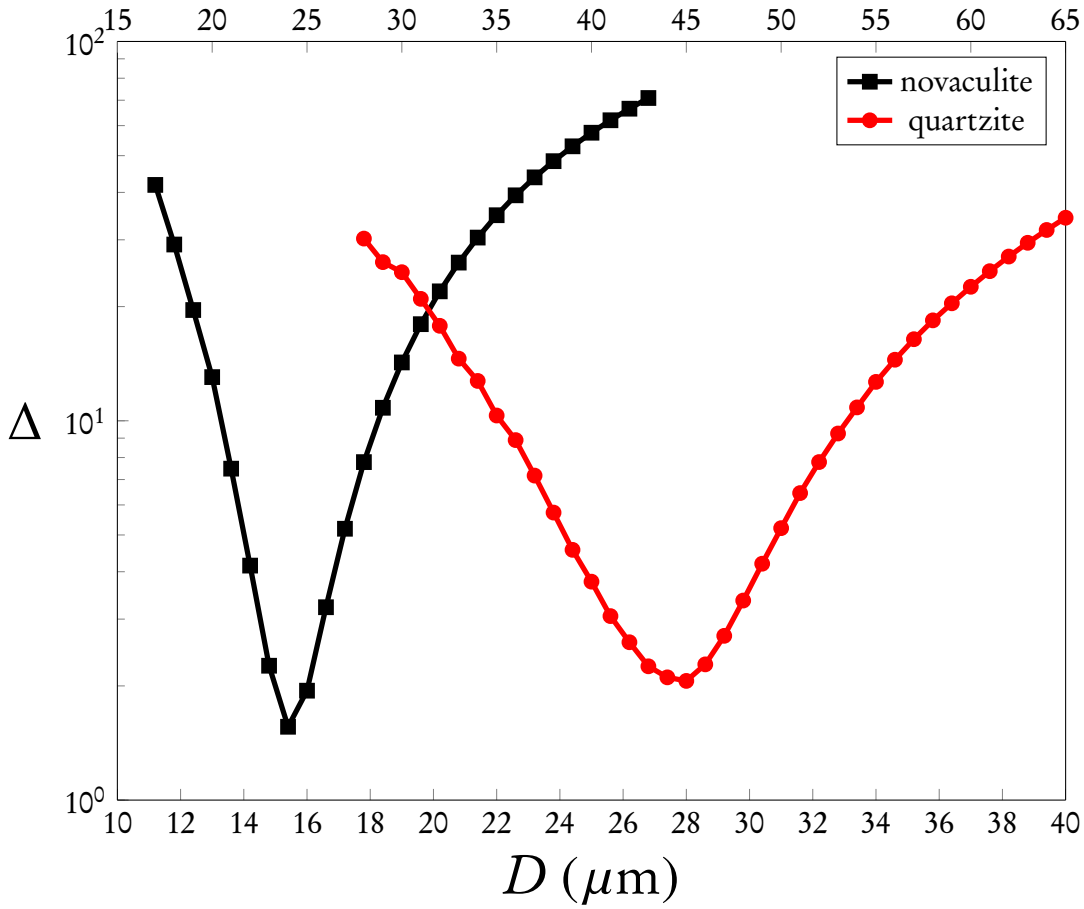

Figure II.6: Comparison between novaculite and quartzite misfits using identical parameter choices except for the asperity sizes D. The lower axis for D corresponds with τ_c = 9.4 GPa, which is the higher value in the range quoted in Table II.1; the upper axis corresponds with τ_c = 7.3 GPa.

one-dimensional model. The neglect of heat transport parallel to the slip plane could be justified even with $VD/\alpha < 1$ if lateral boundary conditions prevent significant heat loss. Moreover, for describing the heat transport in the weakened layer itself, the condition that $D \gg w$ should ensure that a one-dimensional approximation is reasonable; this condition is satisfied by all the model calculations reported here. For the general case where a significant fraction of the dissipated heat is conducted in the plane of the sliding surface at relatively low V (~0.01–0.1 m/s), the sliding velocity at the onset of weakening would

be expected to exceed the effective velocity V_w that characterizes changes in frictional behavior at much higher slip speeds V that cause the Peclet number to be large. With the published experimental data that are currently available to test theoretical predictions, we view efforts to develop more elaborate three-dimensional descriptions of the heat transport as premature.

The overall agreement between the inferred parameters and the a priori estimates suggests that our model captures the essential physical processes reasonably well, despite the simplifying assumptions that we have made. However, the elevated data variability at high sliding velocities does produce considerable ambiguity in determining the best choices for S and V_p. Additional high-quality data at sliding rates $V \gg V_w$ would further increase confidence in the values of asperity-scale parameters that can be inferred from the macroscopic frictional behavior.

II.4.2. Rate Dependence of Friction

Our model builds upon earlier work (Rice, 1999, 2006; Beeler et al., 2008; Rempel and Weaver, 2008) in which the controls on friction at a microscopic level are described in terms of a local friction coefficient f that takes some value f_0 when asperities first make contact but transitions to a weaker level f_w once the time of contact reaches $t = t_w(V)$, so that

$$f(V,t) = f_0 + (f_w - f_0)H(t - t_w), \tag{II.18}$$

where H is the Heaviside step function and t_w is well-approximated by equation (II.11). Substituting equation (II.18) into equation (II.9) and differentiating with respect to slip speed gives the macroscopic rate dependence as

$$\begin{aligned}\frac{\partial \mu}{\partial V} = {} & \frac{1}{V}\left[\mu - f_w\left(V,\theta\right)\right] - 2\frac{t_w}{D}\left[f_0 - f_w\left(V,t_w\right)\right] \\ & + \frac{1}{\theta}\int_{t_w}^{\theta}\frac{\partial f_w}{\partial V}\,\mathrm{d}t.\end{aligned} \tag{II.19}$$

The first term on the right side of equation (II.19) is the difference between the macroscopic friction coefficient μ and the local friction coefficient f_w at the end of asperity contact. When asperities weaken in response to high flash temperatures, we expect the local friction to be lower at the end of an asperity's lifetime than the average friction over its entire lifetime, so $\mu > f_w(V, \theta)$, and this term gives a positive contribution to $\partial\mu/\partial V$. The second term on the right side of equation (II.19) represents an instantaneous change in friction when the threshold-weakening temperature is reached. The final term accounts for changes in contact strength at later times. Together these last two terms are associated with velocity-weakening behavior.

For the flash-weakening model introduced by Rice (1999, 2006) (see also (Beeler et al., 2008; Goldsby and Tullis, 2011)) f drops abruptly at t_w from f_0 to a lower value f_w and subsequently remains constant. In this case the integral term disappears, and the other two terms in equation (II.19) simplify to

$$\frac{\partial \mu}{\partial V} = -\frac{V_w}{V^2}(f_0 - f_w). \tag{II.20}$$

Importantly, since $f_0 > f_w$, this microphysical model always implies that the predicted macroscopic friction weakens with increases in slip rate (i.e., $\partial\mu/\partial V < 0$ for all $V > V_w$).

Changes to the nature of the rate dependence are possible when f_w is able to continue to evolve after the weakening time t_w is reached. Indeed, an evolution in the local frictional properties was anticipated in earlier work (e.g., see the discussion by Rice (2006)), and the constant empirical value for f_w that has been adopted should be regarded in this context as a convenient approximation for describing the available laboratory data. The current model stipulates that shear resistance is continuous at t_w, as might be expected if the weaker of two processes governs the instantaneous level of shear resistance at the asperity scale. With this simplification $f_w(V, t_w) = f_0$, so the middle term in

equation (II.19) drops out, and the rate dependence of friction satisfies

$$\frac{\partial \mu}{\partial V} = \frac{1}{V}[\mu - f_w(V, \theta)] + \frac{1}{\theta}\int_{t_w}^{\theta} \frac{\partial f_w}{\partial V}\, \mathrm{d}t. \tag{II.21}$$

Whether the asperity-scale interactions lead to velocity strengthening or velocity-weakening macroscopic friction depends on the relative magnitudes of the two terms on the right. The experimental data clearly demonstrate that $\partial\mu/\partial V < 0$ when θ is only moderately larger than t_w (i.e., when V is moderately larger than V_w), and this is consistent with equation (II.21) as long as $\partial f_w/\partial V$ is sufficiently large and negative when $\theta > t > t_w$. However, the decrease in f_w with slip speed must eventually become more gradual to keep $f_w \geq 0$, and the potential arises for rate strengthening to take place at higher V. Such rate strengthening can occur even when the local asperity-scale frictional resistance decreases monotonically with contact time.

Figure II.5 illustrates the transition from rate weakening to rate strengthening predicted by the current model using the best fit parameters for novaculite from Figure II.2d. Such high-speed rate-strengthening behavior may affect the degree of shear localization in the thick gouge layers that are characteristic of mature faults (e.g., Brantut and Sulem, 2012; Rice et al., 2005a; Platt et al., 2010). Keeping all other parameters constant, Figure II.5b shows that decreases in V_w and V_p with reduced ΔT cause the transition from rate weakening to rate strengthening to take place at lower slip velocities V as the ambient temperature T_{amb} is increased. If rate strengthening causes shear-zones to broaden at high T_{amb}, then frictional heat will be dissipated over greater gouge volumes, and this may limit the ultimate temperature rise experienced during earthquakes. We note that granular dynamics studies (e.g., Kuwano and Hatano, 2011) exhibit rate strengthening at low effective stresses and high slip rates, which may also tend to cause shear zone broadening that slows the rate of temperature increase as thermal pressurization raises the pore pressure, and conditions are approached for the bulk melting of mineral grains that

would otherwise produce pseudotachylytes.

In our model formulation we have assumed constant values for the asperity size D and contact strength σ_c, whereas previous workers have highlighted a role for increases to the total area of contact in producing elevated μ just prior to the onset of macroscopic melting in HVRF experiments conducted to large (i.e., > 1 m) slip distances (e.g., Brown and Fialko, 2012; Hirose and Shimamoto, 2005; Spray, 2005; Tsutsumi and Shimamoto, 1997). The physical mechanisms responsible for the changing rate dependence predicted by our model are illustrated through the plots in Figure II.5c of the local friction coefficient f as a function of normalized time t/θ. Since the average macroscopic friction μ is the time average of f, $\mu(V)$ is proportional to the area under the corresponding curve for f. What determines the predicted rate dependence of friction is how the average strength of an asperity over its short lifetime changes with sliding speed V. After the weakening time, the asperity strength evolves as the weakened layer thickness $w(t)$ increases. A higher sliding speed always causes the weakened layer to grow more quickly since it increases the strain rate V/w, which helps determine the rate of heat input; however, higher speeds also reduce the lifetime during which this growth can take place before contact ceases. Moreover, the enhanced energy dissipation that enables faster layer growth is only possible because the weakened contact strength $\eta V/w$ at any given layer thickness is slightly stronger than it would be if the strain rate were reduced. Putting this together highlights three essential components of the problem: (1) the effect of velocity in causing the weakened layer to evolve (higher V increases the rate of energy input Q and makes growth $\mathrm{d}w/\mathrm{d}t$ faster), (2) the effect of velocity on increasing the strength of a weakened layer with a given thickness w (higher V makes strength $\eta V/w$ higher), and (3) the effect of velocity on the time over which weakening accumulates (higher V reduces contact lifetime θ). Rate weakening requires that the first effect dominates the other two, and rate strengthening requires that the second two effects dominate the first. Figure II.5c shows

that the average value of f becomes smaller at first as V increases to modest multiples of the weakening velocity V_w, but that the average f increases with V once slip velocity is sufficiently high.

II.4.3. Changes in Physical Properties

We have constructed an idealized model that treats physical parameters as constants even though the sliding systems we seek to describe are populated by heterogeneous asperity contacts that experience large changes in temperature over their lifetimes. The potential limitations of our approximate treatment deserve further mention.

The specific heats of different minerals vary over a relatively wide range, but the volumetric heat capacities ρC fall within more narrow bounds because the specific heats and densities of solids tend to be inversely correlated (e.g., Kobranova, 1990). As the temperature increases, the classic Einstein-Debye model predicts that the heat capacity rises toward a high-temperature limit, as confirmed by laboratory measurements (Robie and Hemingway, 1995). The largest changes in ρC occur over the first several hundred degrees centigrade of temperature rise above ambient room temperature, giving typical increases on the order of 50% (Robertson, 1988) followed by much more gradual increases subsequently. This variation, while appreciable, is not significant in comparison to the changes and variability expected from some of the other controlling parameters.

For simplicity in the current model we have characterized each sliding system with a single value of the thermal diffusivity α that should be viewed as an average property of the many different asperities that are in contact at a given instant. The differences between the thermal conductivities of different minerals tend to be larger than the corresponding differences in ρC (Clauser and Huenges, 1995; Robertson, 1988). Even in a monominerallic rock, the thermal conductivity can vary by more than a factor of 2 depending on the orientation of the grains relative to the direction of heat flow, with

a notably large degree of anisotropy exhibited by quartz. Laboratory results indicate that as the temperature increases, this anisotropy becomes less pronounced, and the thermal conductivity tends to decrease (Kanamori et al., 1968; Robertson, 1988). Since α is defined as the ratio of the conductivity (which decreases with T) to the volumetric heat capacity (which increases with T), fractional changes in α are larger than fractional changes in ρC over the same temperature range. Reductions in α at high temperatures would be expected to retard the rate of heat transport away from the central plane and increase the growth rate of the weak layer. However, the overall character of the predicted frictional evolution is unlikely to be affected by these modifications, and the use of a lower, thermal-history-averaged value of α (e.g., Rice, 2006) could provide an acceptable way of approximating these effects. More notable are the expected heterogeneities associated with different contact mineralogies and orientations. These will violate the symmetry condition applied here along the central plane and also lead to differences between the weak layer development from one contact to the next. Weakening temperatures, contact strengths, layer viscosities, and even asperity sizes are all expected to be sensitive to the particular combination of minerals that make brief contact during rapid slip. A stochastic modeling approach, for example, with a large number of asperities whose properties are assigned based upon the known modal compositions, could be employed to address these complications in a more elaborate numerical treatment constrained by a more extensive suite of HVRF data.

The volumetric latent heat ρL is the energy required to form the weak layer. The values listed in Table II.1 are based upon the enthalpy change measured in melting experiments at one atmosphere pressure (Rempel and Weaver, 2008). At the high confining pressures σ_c along asperity contacts, if given sufficient time, many minerals will undergo a series of solid-state phase transitions before reaching temperatures that are hot enough for melting to begin (Rempel and Weaver, 2008). It seems unlikely that such equilib-

rium phase behavior is followed during the brief lifetimes of individual asperity contacts. Laboratory calorimetric experiments suggest that the value of ρL does not vary greatly as the melting temperature of the same mineral increases with more modest variations in pressure (Stebbins et al., 1983). Without compelling evidence to support alternative choices, we view the values of ρL adopted here as the most defensible values that are currently available.

Two estimates of initial asperity strength $\tau_c = f_0 \sigma_c$ are provided in Table II.1, the lower values compiled by Rempel and Weaver (2008) are based on mineral hardness correlations (Broz et al., 2006; Beeler et al., 2008), and the higher values are obtained from nanoindentation tests by Goldsby and Tullis (2011). In fact, both sets of values are first derived for σ_c, and then multiplied by the observed low-speed friction f_0 to obtain τ_c. The Goldsby and Tullis (2011) measurements were performed on single crystals of the most abundant minerals in these systems and then averaged to obtain the values listed for gabbro and granite. The Rempel and Weaver (2008) estimates derived from a slightly more elaborate averaging procedure that attempts to account for contributions from more of the rock constituents but is based only on correlations rather than direct measurements. On balance, the Goldsby and Tullis (2011) values are likely more accurate, so the lower inferred asperity sizes given in Table II.2 are our preferred estimates. Mineral hardness is expected to decrease with increases to the ambient temperature, and since "Byerlee's law" suggests that values of f_0 should not alter appreciably, this suggests that lower values of τ_c may become important at higher ambient temperatures.

To simplify the model treatment, we have neglected variations in normal stress and assumed that the contact stress σ_c is also constant. This implies that there is no mechanism for the total contact area to evolve in our model, and we have further simplified our treatment by considering the case of a single representative asperity size D. Beeler et al. (2008) showed that accounting for a distribution of asperity sizes modifies predicted flash

weakening behavior by smoothing out the initial rapid variation in μ once V_w is first exceeded. We expect that similar qualitative effects would result from adopting a range of weakening temperatures to account for the different compositions and orientations of mineral grains that make contact at asperities. For example, although novaculite, quartzite, and albite are all monomineralic, the assumption of a single weakening temperature for gabbro and granite is rather crude, and a more detailed model would account for progressive thermal breakdown at increasingly refractory mineral contacts (e.g., Spray, 1995).

The development of gouge layers during HVRF experiments suggests a potential role for changes in friction that could be sourced to asperity evolution or localization phenomena that are not captured in our simple model. Indeed, the role of comminution and the presence of gouge are prominent both for their ubiquity in field settings and their absence from most theoretical treatments, including ours. Our modeling strategy emphasizes the inclusion of only those factors that are essential to describing the dramatic drop in frictional resistance that has been attributed to the effects of flash heating. The agreement with the data shown in Figure II.2 (Goldsby and Tullis, 2011) using parameters consistent with a priori estimates (Rempel and Weaver, 2008) makes it possible to argue that the processes we have neglected are of secondary importance. It is worth noting that, unlike many other HVRF experiments that employ slip distance of many meters or tens of meters, the Goldsby and Tullis (2011) experiments were conducted with total slip distances of only a few centimeters. Goldsby and Tullis (2011) found that comminution affected their quartz experiments most and produced gouge thicknesses of up to 30 μm in thickness, with an average over the reported experimental runs of just 20 μm. These small gouge thicknesses, together with the consistency of frictional measurements in both continuously varying velocity tests and velocity stepping tests, further suggest that gouge evolution and localization phenomena likely did not greatly influence the data

displayed in Figure II.2. In contrast, Brown and Fialko (2012) have provided evidence to suggest a prominent role for submillimeter scale contact heterogeneities in HVRF experiments conducted to many meters of slip with more significant gouge production. These experiments exhibited pronounced late-stage frictional strengthening after an initial weakening that they showed to be consistent with the flash-weakening formulation of Rice (2006). Analyzing the asperity-size dependence of our model, following a similar procedure to the rate-dependence arguments in Section II.4.2, suggests that larger asperities should be associated with lower macroscopic friction when our modeling assumptions apply. We infer that the late-stage strengthening observed by Brown and Fialko (2012) may have involved additional physical interactions that caused the behavior at asperity contacts to evolve in ways not captured by our treatment. This highlights the need for new predictive models that fully describe the strengthening that commonly accompanies the formation of the macroscopic frictional melts, ultimately resulting in the formation of pseudotachylyte (e.g., Brown and Fialko, 2012; Hirose and Shimamoto, 2005; Tsutsumi and Shimamoto, 1997; Spray, 1995).

The effective viscosity plays a critical role in governing the evolution of shear strength. The viscosities of silicate melts with known compositions can be calculated from established correlations (e.g., Hui and Zhang, 2007), but the results are sensitive to the temperature. In the model developed here, since $w_0 \ll \sqrt{\alpha t_w}$, the temperature profile at time t_w described by equation (II.12) predicts that the maximum temperature in the weakened layer exceeds T_w by approximately $\tau_c V w_0/(8\alpha\rho C) = (\pi/8)(V/V_p)^2\Delta T$, which tends to be small when V only modestly exceeds V_w. Most of the heat that is generated after the weak layer forms is either conducted away or consumed during layer growth so that the subsequent temperature rise is limited. Hence, we have treated the viscosity in the layer as a constant for all calculations presented to this point. It is instructive to briefly examine how our predictions change when we account for the temperature dependence

of viscosity.

At higher sliding rates we expect decreases in viscosity with temperature to become more significant. To examine the net effect of these changes on the macroscopic friction, we generalize the heat source formulation from equation (II.13) so that

$$Q(y,t) = \tau(t)^2/\eta(y), \tag{II.22}$$

where

$$\tau(t) = V\eta(T_w)\left(2\int_0^{w(t)/2}\frac{\mathrm{d}y}{\tilde{\eta}(y)}\right)^{-1}, \tag{II.23}$$

with $\tilde{\eta} \equiv \eta/\eta(T_w)$ and η a prescribed function of temperature. For a specific illustration, we focus on the case of novaculite and use a varying-viscosity formulation adapted from the temperature dependence described in Hui and Zhang (2007) so that

$$\log\tilde{\eta}(T) = \frac{B_\eta}{T} - \frac{B_\eta}{T_w} + \exp C_\eta\left(\exp\frac{D_\eta}{T} - \exp\frac{D_\eta}{T_w}\right). \tag{II.24}$$

The parameters $B_\eta \approx 1.81\times10^4$ K, $C_\eta = 0$, and $D_\eta \approx 2.16\times10^3$ K for molten quartz are taken from Table II.2 of Rempel and Weaver (2008) (the table also provides values relevant to the other sliding systems we have examined). In our calculations, since $|T - T_w| \ll TT_w/D_\eta$, the viscosity variation with temperature is dominated by the first term in equation (II.24), which is the same as for a simple Arrhenius model.

Figure II.7 compares the predictions of our constant viscosity model and the varying viscosity formulation just described. As expected, at low sliding rates the two curves are almost identical because the temperature variation in the weakened layer is small. The relative difference between the two sets of predictions shown in Figure II.7b increases at higher sliding velocities, particularly in the rate-strengthening regime. Intuitively, one might expect the reduced viscosities at higher temperatures to cause the overall macroscopic friction to be lower than the predictions of the constant-viscosity model. However, because the reduced viscosity generates less heat, the weakened layer grows

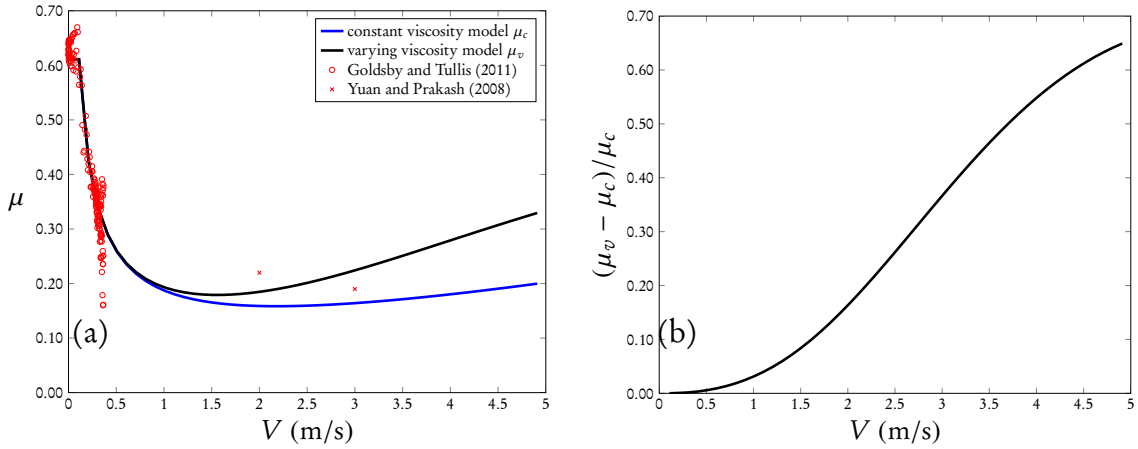

Figure II.7: (a) Comparison between the novaculite results of the constant-viscosity calculation and a temperature-dependent varying-viscosity formulation. The two curves are almost the same at low velocities, but (b) shows that the difference between them becomes significant at high slip rates. The two data points at high slip rates in Figure II.7a are from the experiments of Yuan and Prakash (2008a).

more slowly, and for the example shown here this effect dominates and actually causes a net strengthening in comparison with the predictions derived using a higher, constant viscosity. For reference, the two HVRF experimental data points shown in Figure II.7a with $V \sim 2$ and 3 m/s are from Yuan and Prakash (2008a).

II.4.4. Initial Weak Layer Formation

The dynamic shear strengths of rocks at coseismic slip rates have a complex evolution and alternative weakening mechanisms that do not involve the production of melt are certainly possible. Several HVRF experiments that have detected the formation of melt patches have associated flash heating with their presence (Brown and Fialko, 2012; Yuan and Prakash, 2008a; Hirose and Shimamoto, 2005). In our model, equation (II.15) accounts for the consumption of energy required to form a weak layer, and the shear stress formulation generalized in equation (II.23) describes the subsequent dissipation (with $\tilde{\eta} = 1$ for all displayed results except Figure II.7). If alternative weakening mechanisms

dominate, these components of the energy balance might need to be reconsidered, but we are encouraged by the agreement we have shown between our model predictions and the experimental data.

Assuming that the development of a viscous layer is responsible for flash weakening, it is nevertheless difficult to model the initial stages of weak-layer development. We assume that $w_0 = \eta V/\tau_c$ so that the shear stress remains continuous at the weakening time; to guard against immediate strengthening subsequently, we further assume an abrupt temperature drop within the layer from T_s to T_i. To more precisely satisfy energy balance considerations, the temperature drop should actually correspond with the energy consumption required to form a weak layer of the initial thickness. A comparison of the difference between these quantities with the total energy dissipated prior to the weakening time indicates that

$$\begin{aligned} &\frac{1}{\tau_c V t_w}\left|\rho C \int_{-w_0/2}^{w_0/2} (T_s - T_i)\ \mathrm{d}y - \rho L w_0\right| \\ &\approx \frac{w_0}{\sqrt{\pi\alpha t_w}}\left|\frac{\pi w_0}{6\sqrt{\pi\alpha t_w}} - S\right|, \end{aligned} \tag{II.25}$$

where the approximation for $T_s - T_i$ used to evaluate the integral on the left is accurate to leading order in $w_0/\sqrt{\alpha t_w}$. Since $w_0/\sqrt{\pi\alpha t_w} \approx \left(V/V_p\right)^2$ and S are both much smaller than unity in the regime of interest, the approximate treatment we have employed does not introduce substantial errors to the energy balance.

Alternative flash treatments have assumed different conditions at the onset of weakening. For example, equation (II.6) derives from an approximate treatment of weak-layer growth where the weakening onset is assumed to take place once the temperature on the sliding plane reaches T_w (Rempel and Weaver, 2008). The dashed lines in Figure II.2 show that the closed-form expression for μ_s does a reasonable job of matching the experimental data using the same value for S as derived from the fit for our model. Lower values of V_w are necessary, however, because the approximate treatment of conductive losses from

the growing layer that leads to μ_s implies a more gradual weakening onset (it can be shown that $\partial\mu_s/\partial V = 0$ at $V = V_w$) than predicted by the current formulation. It should be noted that weakened layers are predicted to extend only a few tens of nanometers, and hence, following the grinding damage incurred during HVRF experiments, detection of melt products is likely to be even more challenging than the notoriously elusive macroscopic pseudotachylytes (Kirkpatrick and Rowe, 2013).

II.5. Conclusion

We have shown that our micromechanical model, which attributes macroscopic frictional resistance to the development of microscopic weakened layers, agrees with experimental HVRF data. Using independent literature values for all other properties, the weakening temperatures and layer viscosities that ensure the best model fits to HVRF data are consistent with anticipated melting temperatures and melt viscosities at the high confining pressures ($\sim$ 1–20 GPa) expected at asperity contacts with sizes comparable to a priori estimates. The model formulation is easily extended beyond the parameter range spanned by current experiments to predict the frictional behavior under different ambient temperatures and siding velocities. At moderate sliding rates the model predictions resemble the closed-form expression for μ_s given by equation (II.6) (Rempel and Weaver, 2008). At higher sliding rates the model predicts a transition to rate-strengthening behavior because higher sliding rates result in shorter contact lifetimes, causing a reduction in the maximum thickness that asperity-scale weak layers can achieve. At higher ambient temperatures the transition from rate weakening to rate strengthening is expected to occur at lower sliding rates.

II.6. Bridge

The nature of friction resistance can become quite complicated, and phenomenological laws such as the widely used rate-state relationship are not designed to address the friction evolution at high slip speeds based upon the underlying physical interactions. In this chapter, we view the friction as the average effect from the local resistance on asperities, and obtain the effective frictional resistance along a contact surface. From the perspective of scales, we start from the microscopic scales of asperities (D is usually several microns) and build toward a mesoscopic description applicable along granular contact surfaces. Follow similar reasoning, we can view the actual fault zone as a large collection of granules, and the overall fault strength as the average of friction on the contact surfaces between them. In the next chapter, we will explore how macroscopic fault strength can be addressed in view of an averaged treatment of mesoscale transient granular slip.

CHAPTER III

SHEAR ZONE BROADENING CONTROLLED BY THERMAL PRESSURIZATION AND POROELASTIC EFFECTS DURING MODEL EARTHQUAKES

This chapter is in the final stage of preparation for submission to *Journal of Geophysical Research: Solid Earth*. In this work we developed a model of coseismic fault strength that incorporates the interactions between variations in pore pressure of saturated porous media and the localization-pressurization phenomenon. As the leading author I developed this model, and did the numerical simulations. Alan Rempel provided constructive advice for the work and helped with the manuscript.

III.1. Introduction

Mature faults are characterized by thick layers of pulverized gouge that result from the comminution that takes place over numerous earthquake cycles. There is abundant evidence, however, that during a single earthquake the active shear zone typically occupies only a small fraction of the total gouge thickness. Both the physical interactions that determine earthquake behavior and their geologic signatures recorded in fault rocks depend on shear-zone width. For example, the rate with which coseismic heating is able to cause the pore fluid pressure to rise and lower fault strength during the process

of thermal pressurization depends on the width of the zone that accommodates shear (Sibson, 1973; Lachenbruch, 1980; Rice, 2006; Rempel and Rice, 2006; Brantut et al., 2010; Ujiie and Tsutsumi, 2010; Garagash and Germanovich, 2012). Similarly, shear width exerts a strong control on the maximum temperature rise, and hence the potential for melting fault constituents and producing the records of past earthquake activity known as pseudotachylytes (Cowan, 1999; Otsuki et al., 2003; Spray, 1987, 1995, 2010). In addition, the high-speed frictional behavior referred to as "flash weakening", along with any other velocity-dependent mechanism for changing the friction coefficient itself, should generally be expected to depend on the total thickness over which shear strain is distributed (Brown and Fialko, 2012; Chen and Rempel, 2014; Di Toro et al., 2004; Goldsby and Tullis, 2011; Han et al., 2011; Kohli et al., 2011; Rempel and Weaver, 2008; Rice, 2006).

Tremendous progress has been made in developing numerical models to track the evolution of fault strength, often including the effects of thermal pressurization and flash heating. Most treatments set the shear width as a fixed parameter (sometimes zero) without attempting to treat the physical interactions that control it. The process by which static regions begin to deform, granules accelerate, and fractures develop demands further examination in light of its importance for fault-zone behavior. Intuition suggests that mechanisms causing increased weakening at higher slip rates should favor thinner shear zones, whereas rate-strengthening is expected to result in thicker shear zones that could allow the relative velocities between shear-zone particles to remain lower. This tendency is consistent with the results of a recent detailed analysis that shows how stabilization by frictional rate-strengthening and dilatancy competes with the localizing influence of thermal pressurization in model predictions of shear-zone width (Rice et al., 2014; Platt et al., 2014). When dilatancy is neglected and rate-weakening or rate-independent friction combine with thermal pressurization to control the shear-zone strength according to the Terzaghi effective stress rule (Terzaghi, 1936), the only configuration that is stable

to infinitesimal perturbations involves slip on a mathematical plane. Nevertheless, as discussed further below (see also, Appendix A of Rice, 2006), the evolving stress state produced by porothermoelastic effects leads to the development of a broadening zone in which increases in pore pressure and temperature cause the shear stress to exceed the local strength. This suggests an apparent contradiction in that the zone poised for shear failure becomes progressively wider even as the width predicted from momentum balance considerations for the shear-zone itself localizes dramatically. Here, we present an alternative formulation that attempts to address this discrepancy by considering the net effect of multiple transient localized slip events within a broadening shear zone whose boundaries are defined by balancing the gouge frictional strength and the shear stress according to the Mohr–Coulomb criterion.

III.2. Background

Before delving into the analysis and presenting our model results, we first provide a brief summary of pertinent observations from the field and the laboratory, as well as some important insights into the controls on shear-zone width that emerge from force balance considerations.

III.2.1. Field observations

There is abundant field evidence to suggest that the relatively thick (i.e., meter-scale) gouge layers that characterize mature faults are in fact comprised of complex internal structures, including numerous fine-scale features that appear to record deformation that occurred during different seismic events. For example, observations made along the San Gabriel and Punchbowl faults in Southern California show that decimeter-scale layers of ultracataclasite are hosted within foliated cataclasite that extends to several meters in

thickness (Chester et al., 1993; Chester and Chester, 1998; Chester et al., 2004). Detailed analysis of ultracataclasite samples from the San Gabriel fault suggests that extreme coseismic shear occurred within still narrower zones that are less than 5 mm thick. Further work along the Punchbowl fault by Chester et al. (2003) revealed that, within a $\sim$ 1 mm zone of comminuted gouge, there is internal structure to indicate that much of the shearing actually took place in a layer of approximately $100 - 300\,\mu$m thickness. Lockner et al. (2000) and Otsuki et al. (2003) studied the Nojima fault in Japan which ruptured in the 1995 Kobe earthquake, and found mm-scale layers of very fine gouge ($< 30\,\mu$m), alongside several thin bands of pseudotachylyte. The microscopic structure of the 1999 Chi-Chi earthquake fault-zone shows an approximately 3 mm-thick primary shear zone, characterized by a foliated gouge displaying an alternation of clay-rich and clast-rich layers (Boullier et al., 2009).

In the narrow shear zones described above, thermal pressurization should produce elevated pore pressures on seismic time scales (i.e., $O(1\,\mathrm{s})$). Indeed, Noda and Shimamoto (2005) measured the permeability of fault rocks from the active Hanaore fault near Kyoto, Japan, and concluded that the extremely low values ($< 10^{-17}$ m^2), especially in the clayey foliated fault gouge and a finer zone which they referred to as "black clayey gouge", enabled thermal pressurization to reduce the heat dissipation enough to prevent coseismic melting. However, as pointed out by Rice (2006), coseismic damage can disrupt pore-scale microstructure so that both heat and fluid escape from sufficiently thin shear zones become important in modifying the strength evolution during earthquakes. Temperature and pore pressure changes can activate other mechanisms, which might offset the localizing effects of thermal pressurization and lead to shear zone broadening. Field evidence has not placed firm constraints on the potential for coseismic shear zone changes between the narrowest foliations and the much broader surrounding gouge zones. However, there are suggestions that the deforming zone might migrate during an earthquake, resulting in

a network of shear zones that link multiple foliated structures (Ben-Zion and Sammis, 2003; Schrank et al., 2008).

III.2.2. Laboratory experiments

A more finely resolved temporal window into shear zone behavior is provided by laboratory observations. Mair and Marone (2000) conducted experiments to investigate shear heating in granular layers. Their results were consistent with the expectation that rate strengthening is associated with distributed shear, while rate weakening is associated with localized deformation. These experiments were later complemented by 3D numerical simulations of fault gouge evolution (Mair and Abe, 2008; Abe and Mair, 2009) that suggested strain localization may have been promoted by grain-size reduction and development of a structural fabric. Han et al. (2011) observed shear localized in a $\sim$ 2 μm-thick zone in granular periclase samples. Other experiments (Kuwano and Hatano, 2011; Sone and Shimamoto, 2009) suggest that most strain during high-speed slip accumulates in narrow shear zones of several tens to hundreds of microns in width, which is roughly an order of magnitude greater than the characteristic particle size (see also Morgenstern and Tchalenko, 1967; Muir Wood, 2002). Laboratory experiments are typically conducted at much lower confining stresses than are typical of seismogenic depths, suggesting the possibility that inertia may be much more important in laboratory settings (Rice et al., 2014) so that shear-zone width might take longer to evolve than during coseismic slip. Nevertheless, over a broad range of reported conditions, observed shear-zone thicknesses typically exceed a minimum width in the range of 10–20 particle diameters.

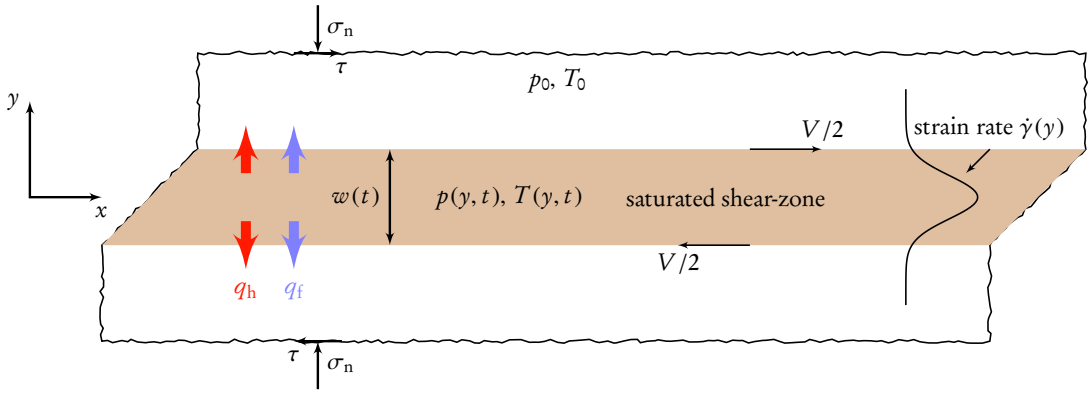

Figure III.1: A schematic of the model.

III.2.3. Force Balance Considerations

An analysis of the stability of uniform, undrained, adiabatic shear can be used to gain some insight into the controls on the preferred shear zone thickness w and how it depends on thermal and hydraulic properties, including the volumetric heat capacity ρC, and the diffusivities for temperature α_{th} and pore pressure α_{hy} (see Figure III.1). Applying the Terzaghi effective stress rule (Terzaghi, 1936), the fault strength τ is expressed as the product of an effective friction coefficient f with the effective stress $\sigma_n - p$. Since inertial effects are expected to be small, the momentum balance condition implies that forces must balance so τ is spatially uniform at a given instant within the shear zone. Following a common approximation to the energy balance, we assume that all of the work performed during shear at strain rate $\dot{\gamma}$ is converted to heat at rate $\tau\dot{\gamma} = f\,(\sigma_n - p)\,\dot{\gamma}$. Treating the total normal stress σ_n as constant, then with all other material properties fixed, a drop in shear thickness w increases the strain rate $\dot{\gamma}$, thereby raising the temperature faster to enhance the pressurization of pore fluid and weaken the fault. This localizing influence of thermal pressurization can be counteracted by frictional behavior that is rate-strengthening so that $\partial f/\partial V > 0$. For rate-weakening or rate-independent friction, this idealized treatment predicts that localization decreases the shear thickness to zero so

that slip takes place on a mathematical plane.

As described further in Appendix B.1 and consistent with previous treatments (Rice et al., 2005a; Platt et al., 2010; Brantut and Sulem, 2012; Platt et al., 2014; Rice et al., 2014), when the friction is rate-strengthening the maximum thickness of a layer undergoing uniform shear that is stable to infinitesimal plane-wave perturbations can be expressed as

$$w_{\mathrm{cr}} \approx \frac{4\pi^2 \rho C (\alpha_{\mathrm{hy}} + \alpha_{\mathrm{th}})}{f\Lambda \left[2V \left(\partial f / \partial V\right) + f\right] - \tau \left(\partial f / \partial T\right)} \frac{\partial f}{\partial V}, \tag{III.1}$$

where $\Lambda = \left(\lambda_f - \lambda_n\right) / (\beta_f + \beta_n)$, and λ and β are the expansivities and compressibilities of the fluid phase (subscript f), and pore volume (subscript n). Equation (III.1) gives a useful estimate of the shear zone width w with uniform strain rate $\dot{\gamma} = V/w$, when the effective friction coefficient f is assumed to depend only on the temperature T and slip rate V. Increases in temperature T are accompanied by increases in the pore pressure p (i.e., reduced effective stress), because the thermal expansivity of water λ_f is greater than typical values for gouge minerals, whose expansion causes the void space to increase with temperature by an amount proportional to the coefficient $\lambda_n < \lambda_f$. The greater the expansion factor Λ, the stronger the localizing influence of thermal pressurization and the smaller the predicted shear width w_{cr}. By contrast, the greater the combined diffusivity $\alpha_{\mathrm{hy}} + \alpha_{\mathrm{th}}$, the more rapidly thermal and pore pressure anomalies expand outwards to reduce the strength further from the central plane and facilitate larger shear widths.

As shear progresses and changes in fault-zone conditions cause parameters such as the hydraulic diffusivity α_{hy} and the expansion factor Λ to evolve, equation (III.1) can provide some intuition for the expected response of shear width. Figure III.2 illustrates how w_{cr} depends on the hydraulic diffusivity α_{hy}, which is expected to increase as effective stress drops over the course of an earthquake. Each curve is calculated using the different values of $\partial f / \partial V$ and Λ that are noted on the plot. The figure suggests that both the decreases in Λ and increases in α_{hy} that are expected to result from coseismic changes

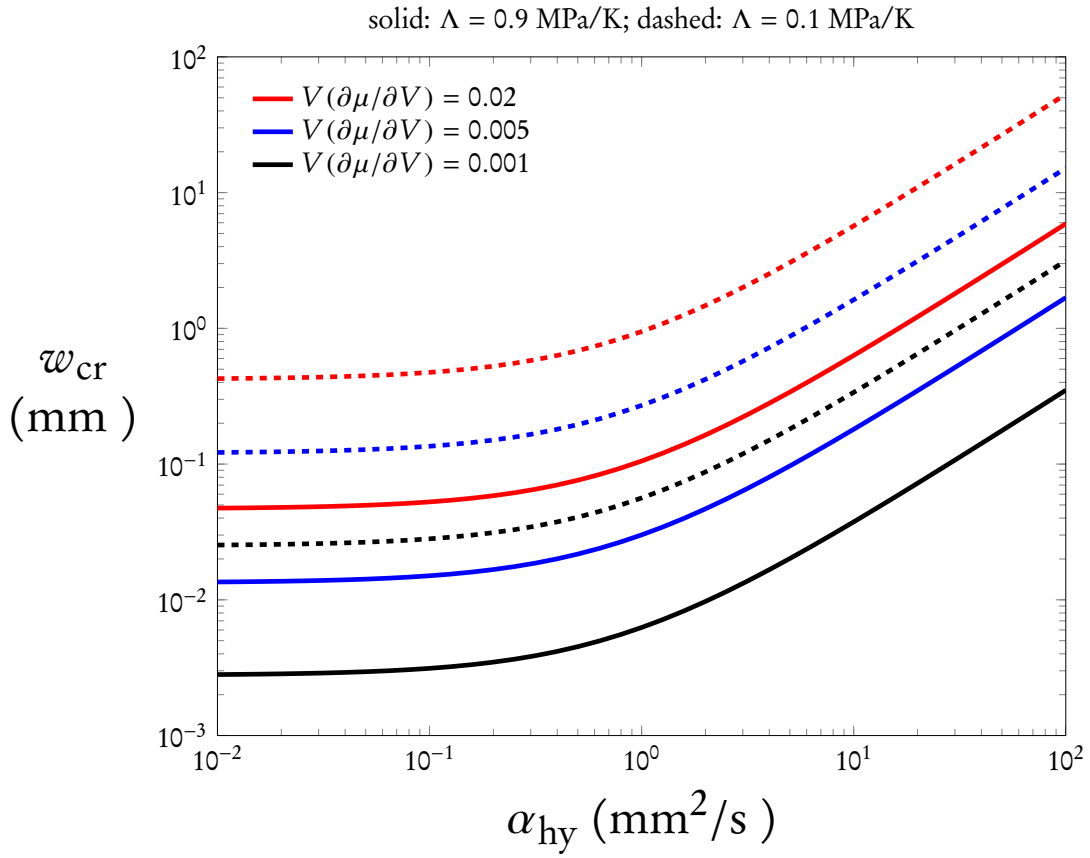

Figure III.2: Predicted shear zone thickness dependence on the hydraulic diffusivity.

in fault properties (e.g., Rempel, 2006) should produce increases in w_{cr} for any fixed value of V $(\partial f/\partial V)$. It should be emphasized, however, that the results of this linear stability analysis are only suggestive rather than predictive, since the formulation is in reference to a base case with negligible flow of heat and mass, and nonlinear effects are neglected. Nevertheless, Platt et al. (2014) demonstrated that the shear-zone width predicted by a nonlinear treatment that accounts for heat and mass transport (though without accounting for the coseismic evolution of Λ or α_{hy}) gives very similar results. For the entire range of hydraulic diffusivities plotted, even with the most dramatic frictional strengthening considered in Figure III.2 and the low value of Λ = 0.1 MPa/K chosen to correspond with the expansion coefficient at elevated temperatures and pore pressures,

the predicted shear width reaches a maximum of several centimeters in width.

In the next section, we reexamine the porothermoelastic constraints on the evolution of shear stress and show that the Mohr–Coulomb criteria predicts that the shear strength is exceeded in a broadening zone that can become much wider than the shear thickness predicted from the linear stability analysis leading to Equation (III.1). This leads us to propose an alternative model for shear-zone behavior that is characterized by a finite shear width even when the friction is rate weakening or velocity neutral.

III.3. Dynamic shearing model

Linear stability analysis predicts that rate-strengthening friction favors broader shear-zone widths w_{cr} that lower strain rate for a given total slip-rate. However, there are potential problems with this as a general explanation for the controls on shear-zone width throughout the seismogenic zone. Earthquake nucleation requires rate weakening (e.g., Chester and Chester, 1998; Scholz, 1988; Dieterich, 1994; Garagash and Germanovich, 2012; Viesca and Rice, 2012), whereas the simple theory predicts that only planar slip is stable in this case. Many exhumed faults appear to have finite shear zone thicknesses that are more than an order of magnitude larger than the median grain diameter; the linear analysis suggests that rate-strengthening, or some other mechanism must be invoked for significant coseismic shear in such zones to accumulate. Indeed, increases in fault temperature can cause an evolution to rate-strengthening friction (e.g., Blanpied et al., 1995), and there are several other independent indications that a transition may take place from pronounced rate weakening to rate-strengthening friction at coseismic slip rates. Such behavior emerges from treatments of progressive flash heating by the development and growth of thermally-activated weak layers along contact surfaces as in Chapter II (Rempel and Weaver, 2008; Chen and Rempel, 2014), particle dynamics models for shear

at low effective stresses (Kuwano and Hatano, 2011), and observed changes in resistance at large slip distances as melting conditions are approached in high-velocity rock friction experiments (Spray, 1987; Tsutsumi and Shimamoto, 1997; Hirose and Shimamoto, 2005; Brown and Fialko, 2012). However, momentum balance considerations are difficult to satisfy within a finite region that experiences a transition from rate-weakening to rate-strengthening, as the following simple argument shows.

III.3.1. Momentum balance

As long as the Terzaghi effective stress rule holds, the momentum balance requires that for regions where inertial effects are negligible, the shear stress must satisfy

$$\frac{\partial}{\partial y}[f(\sigma_{\mathrm{n}} - p)] = 0. \tag{III.2}$$

If we assume a constitutive relationship for friction where f depends only on the temperature T, and the strain rate $\dot{\gamma}$, the equation above can be expanded to

$$\frac{\partial f}{\partial T}\frac{\partial T}{\partial y} + \frac{\partial f}{\partial \dot{\gamma}}\frac{\partial \dot{\gamma}}{\partial y} = \frac{f}{\sigma_{\mathrm{n}} - p}\frac{\partial p}{\partial y}. \tag{III.3}$$

Inconsistencies arise if we attempt to solve $\dot{\gamma}$ from equation (III.3) using a frictional constitutive law with a transition from rate weakening to rate strengthening at a threshold in $\dot{\gamma}$ (similar arguments can be constructed if the rheological change coincides with a temperature threshold). If we consider $y = 0$ as the mid-plane of shearing, then for $y > 0$ we expect for our system that $\partial T/\partial y < 0$, $\partial p/\partial y < 0$, and as long as the friction f is temperature-weakening, this implies that

$$\frac{\partial f}{\partial \dot{\gamma}}\frac{\partial \dot{\gamma}}{\partial y} < 0.$$

If the shear zone is in a rate-strengthening regime $\partial f/\partial \dot{\gamma} > 0$, and we have $\partial \dot{\gamma}/\partial y < 0$. If $\dot{\gamma}(y)$ is continuous, it must monotonically decrease with $|y|$ and this implies that there is a distance L beyond which $\dot{\gamma}$ is small enough that the friction is rate-weakening. It follows that for $|y| > L$ we have $\partial \dot{\gamma}/\partial y > 0$, which leads to an improbable result that the strain rate begins to increase towards the shear-zone margins. If f is rate neutral then the problem is worse since there is no way to satisfy equation (III.3) in a zone of finite width with the expected direction of pore pressure and temperature gradients. Under typical seismogenic conditions, accounting for acceleration does not lead to a marked improvement since inertial effects are generally quite small (Platt et al., 2014). Together, these observations motivate further investigation into controls on shear-zone thickness that are suggested by porothermoelastic effects.

III.3.2. Conservation of fluid and heat

When the shear zone is deforming, frictional heat causes the pore fluid inside the gouge to expand, resulting in an outward fluid flow q_f as illustrated in Figure III.1. Ignoring dehydration reactions for simplicity, changes in the fluid mass inside the shear zone must be compensated by outward flow, so that continuity requires

$$\frac{\partial(\rho_\mathrm{f} n)}{\partial t} + \frac{\partial q_\mathrm{f}}{\partial y} = 0, \quad q_\mathrm{f} = -\frac{\rho_\mathrm{f} k}{\eta_\mathrm{f}} \frac{\partial p}{\partial y}, \tag{III.4}$$

where ρ_f is the density of pore fluid, n is the porosity, and the outward fluid flow q_f follows Darcy's law with permeability k, viscosity η_f, and pore pressure $p(y,t)$. As shown in Appendix B.1, if we assume that n only changes elastically, and further simplify the model by taking the fluid density ρ_f and fluid diffusivity $\alpha_\mathrm{hy} = k/[\eta_\mathrm{f} n(\beta_\mathrm{f} + \beta_\mathrm{n})]$ as spatially uniform, equation (III.4) can be written as

$$\frac{\partial p}{\partial t} - \Lambda \frac{\partial T}{\partial t} = \alpha_{\mathrm{hy}} \frac{\partial^2 p}{\partial y^2}, \tag{III.5}$$

where $\Lambda = (\lambda_{\mathrm{f}} - \lambda_{\mathrm{n}})/(\beta_{\mathrm{f}} + \beta_{\mathrm{n}})$. For clarity of presentation we treat Λ and α_{hy} as constant throughout the model domain. However, we note that the effects of damage can cause the drained compressibility and permeability to increase within the shear zone (e.g., Rice, 2006). We reserve further discussion of such complications until later, after first presenting the remaining essential components of our model.

For simplicity, we assume uniform thermal properties in both the shear zone and the ambient gouge. We consider a shear zone with thickness w that starts to deform with strain rate $\dot{\gamma}$ and overall slip rate V at $t = 0$. The conservation of energy requires that

$$\tau \dot{\gamma} = \rho C \frac{\partial T}{\partial t} + \frac{\partial q_{\mathrm{h}}}{\partial y}, \quad q_{\mathrm{h}} = -K \frac{\partial T}{\partial y}, \tag{III.6}$$

where the heat flow q_{h} depends on the thermal conductivity K, which we treat as spatially uniform. Defining the thermal diffusivity as $\alpha_{\mathrm{th}} \equiv K/(\rho C)$, and substituting in for τ using the Terzaghi effective stress rule, the temperature evolution within the shear zone is

$$\frac{\partial T}{\partial t} = \alpha_{\mathrm{th}} \frac{\partial^2 T}{\partial y^2} + \frac{f \dot{\gamma}}{\rho C} (\sigma_{\mathrm{n}} - p), \quad |y| \leq w/2, \tag{III.7}$$

while outside the shear zone, since there is no heat source, the temperature evolution is

$$\frac{\partial T}{\partial t} = \alpha_{\mathrm{th}} \frac{\partial^2 T}{\partial y^2}, \quad |y| > w/2. \tag{III.8}$$

For compatibility with the specified kinematic condition, we also require that the strain rate satisfy

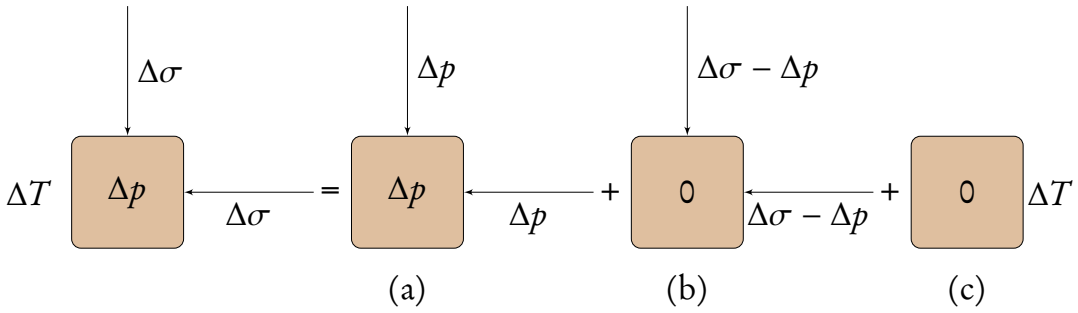

Figure III.3: Thermo-mechanical loading of porous material can be decomposed into three independent problems.

$$\int_{-\infty}^{\infty} \dot{\gamma}\, \mathrm{d}y = V. \tag{III.9}$$

III.3.3. Poroelastic effective stress variation

We can view shear-zone broadening as a process of mobilization in which the deformation might be expected to start (i.e., the shear-zone boundary propagates) when a mechanical threshold is reached. Macroscopically, the shear zone undergoes large finite deformation, but along its boundary while the strain is still small and reversible, we hypothesize that the essential features of mobilization can be determined from a poroelastic analysis. We next review how changes in pore pressure and temperature can cause the effective stress in the direction of shear to evolve more quickly than the effective stress normal to the shear plane, following the line of reasoning presented earlier by Rice (2006, see Appendix A). This difference will be shown in the next subsection to lead to a criterion for potential shear-zone thickness changes.

If the drained compressibility is β_d and the solid grain compressibility is β_s, for a control volume V_0 with porosity n, variations in the reference confining stress $\Delta\sigma_c = \sigma_c - \sigma_{c,o}$, the pore pressure $\Delta p = p - p_o$ and the temperature $\Delta T = T - T_o$ produce a change in total volume that can be expressed as

Table III.1: Variation of volume of the porous material and its constituents for the three independent problems in Figure III.3. The three problems are: (a) hydrostatic loading of saturated material, (b) effective stress loading on drained material, and (c) thermal heating of saturated material.

Problem	ΔV of constituents	
	fluid phase	solid phase
(a)	$-nV_0\beta_f\Delta p$	$-(1-n)V_0\beta_s\Delta p$
(b)		$-V_0\beta_s(\Delta\sigma-\Delta p)$
(c)	$nV_0\lambda_f\Delta T$	$(1-n)V_0\lambda_s\Delta T$

$$\Delta V/V_0 = \varepsilon_{kk} = -\beta_d\Delta\sigma_c + (\beta_d-\beta_s)\Delta p + \lambda_s\Delta T. \tag{III.10}$$

Here, the first term on the right is the drained volume change due to the confining stress variation, the second term represents the effects of pressure changes within the pore fluid, and the last term accounts for thermal expansion. When there is a deviation from the reference state, the coupled thermo-mechanical loading of porous material can be decomposed into three independent problems, as noted in Table III.1 and illustrated in Figure III.3. With these considerations, the solid volume variation is (Ghabezloo and Sulem, 2009)

$$\Delta V_s = -(1-n)V_0\beta_s\Delta p - V_0\beta_s(\Delta\sigma_c-\Delta p) + (1-n)V_0\lambda_s\Delta T. \tag{III.11}$$

The change in porosity n can be written as the difference between the total volume change and the volume change of the solid phase alone, so that

$$\begin{aligned}\Delta n =& \frac{\Delta V-\Delta V_s}{V_0}\\ =& -(\beta_d-\beta_s)\Delta\sigma_c + [\beta_d-(1+n)\beta_s]\Delta p + \lambda_s n\Delta T.\end{aligned} \tag{III.12}$$

At fixed confining stress σ_c equation (III.12) implies that the elastic change in n is

$$\mathrm{d}n = n(\beta_n \mathrm{d}p + \lambda_n \mathrm{d}T) \tag{III.13}$$

where $\beta_n = (\beta_d - \beta_s)/n - \beta_s$.

The shear zone is subjected to plane strain with confining stress in the y-direction, so the stress-strain relation can be written in terms of the deviatoric stress as

$$\sigma_{ij} - \sigma_{ij,o} - (\sigma_{kk} - \sigma_{kk,o})\delta_{ij}/3 = 2\mu(\varepsilon_{ij} - \varepsilon_{kk}\delta_{ij}/3). \tag{III.14}$$

Setting $\varepsilon_{kk} = \varepsilon_{yy}$ and identifying $\sigma_n = -\sigma_{yy}$, equation (III.14) can be used to show that

$$-(\sigma_{\mathrm{n}} - \sigma_{n,o}) - (\sigma_{kk} - \sigma_{kk,o})/3 = 4\mu\varepsilon_{yy}/3, \tag{III.15}$$

$$\text{and } \sigma_{xx} - \sigma_{xx,o} - (\sigma_{kk} - \sigma_{kk,o})/3 = -2\mu\varepsilon_{yy}/3, \tag{III.16}$$

which can be combined to write

$$\sigma_{xx} - \sigma_{xx,o} = -(\sigma_n - \sigma_{n,o}) - 2\mu\varepsilon_{yy}. \tag{III.17}$$

We interpret the confining stress σ_c as $-\sigma_{kk}/3$, and use the expression for ε_{kk} in terms of β_d and β_s from equation (III.10) to write

$$\begin{aligned} &\sigma_{xx} - \sigma_{xx,o} + (1 - \beta_s/\beta_d)\Delta p \\ &= -\frac{\nu_d}{1-\nu_d}[\Delta\sigma_{\mathrm{n}} - (1 - \beta_s/\beta_d)\Delta p] - \frac{2(1+\nu_d)}{3(1-\nu_d)}\mu\lambda_s\Delta T. \end{aligned} \tag{III.18}$$

Setting $\Delta\sigma_{\mathrm{n}} = \sigma_{\mathrm{n}} - \sigma_{n,o} = 0$ and assuming an initial isotropic stress state with $\sigma_{xx,o} \approx -\sigma_{n,o}$, the effective compressive stress in the deformation plane is

$$\begin{aligned}\overline{\sigma}_{xx} = -\sigma_{xx} - p =&(\sigma_{\mathrm{n}} - p) + \frac{1-2\nu_d}{1-\nu_d}(1-\beta_s/\beta_d)\Delta p \\ &+ \frac{2(1+\nu_d)}{3(1-\nu_d)}\mu\lambda_s\Delta T,\end{aligned} \tag{III.19}$$

where μ is the shear modulus, and the Poisson's ratio under drained conditions ν_d follows

$$\nu_d = \frac{3-2\mu\beta_d}{6+2\mu\beta_d}. \tag{III.20}$$

Alongside the effective stress components $\overline{\sigma}_{xx}$ and $\overline{\sigma}_{yy} = -\sigma_{yy} - p \approx \sigma_n - p$, the shear stress is $\tau_{xy} = f\overline{\sigma}_{yy}$.

A simple numerical illustration is useful for showing how changes in the effective stress components arise from porothermoelastic effects. Following Rice (2006) by taking $\beta_s = 1.6 \times 10^{-11}$ Pa^{-1}, $\lambda_s = 2.4 \times 10^{-5}$ K^{-1}, $\beta_d = 5.8 \times 10^{-11}$ Pa^{-1}, and $\mu = 13$ GPa, the effective stress in the deformation plane satisfies

$$-\sigma_{xx} - p \approx (\sigma_n - p) + 0.55\Delta p + 0.31\Delta T \text{ MPa/K}. \tag{III.21}$$

Equation (III.21) clearly predicts that pore pressure increases Δp and temperature increases ΔT cause the effective stress parallel to the shearing direction $\overline{\sigma}_{xx} \equiv -\sigma_{xx} - p$ to undergo larger changes than the effective stress $\overline{\sigma}_{yy} \equiv \sigma_n - p$ in the direction normal to shear. The Mohr–Coulomb criterion will next be used to examine how the resulting changes to the stress state can determine whether a region is poised to become mobilized or required to stay substantially undeformed.

III.3.4. Mohr–Coulomb criterion

The stress state described above implies that the principle stresses can be written as

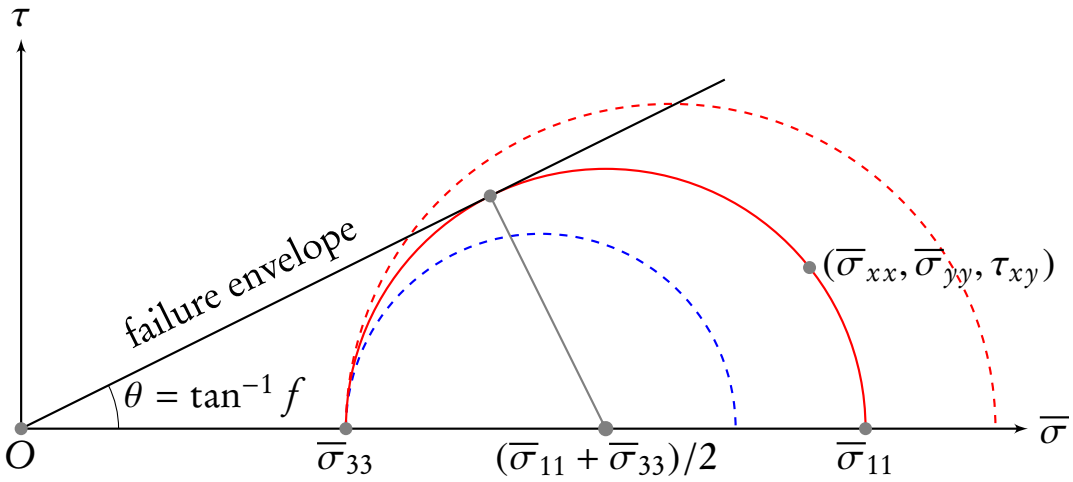

Figure III.4: Mohr circle of the stress state and the failure criterion. The failure envelope with friction f passes through the origin because the cohesion is zero for existing fractures. The blue dash circle is a stress state that will not result in failure, and the red dashed circle is a stress state beyond failure.

$$\sigma_{11} = \overline{\sigma}_{xx}\cos^2\psi + 2\tau_{xy}\sin\psi\cos\psi + \overline{\sigma}_{yy}\sin^2\psi \tag{III.22}$$

$$\sigma_{33} = \overline{\sigma}_{xx}\sin^2\psi - 2\tau_{xy}\sin\psi\cos\psi + \overline{\sigma}_{yy}\cos^2\psi, \tag{III.23}$$

where the rotation angle ψ is determined by setting $\tau_{13} = 0$, which gives $\tan(2\psi) = 2\tau_{xy}/(\bar{\sigma}_{yy} - \bar{\sigma}_{xx})$. Treating the cohesion as zero within the highly comminuted gouge for simplicity, the Mohr–Coulomb criterion illustrated in Figure III.4 is satisfied when

$$\frac{\sigma_{11} + \sigma_{33}}{2}\sin\theta = \frac{|\sigma_{11} - \sigma_{33}|}{2}, \tag{III.24}$$

where $\tan\theta = f$. Equation (III.21) is of the form $\overline{\sigma}_{xx} = \overline{\sigma}_{yy} + A\Delta p + B\Delta T$, which motivates the definition of $r \equiv \overline{\sigma}_{xx}/\overline{\sigma}_{yy} - 1$ to gauge the evolution of the stress state as changes take place to the local pore pressure and temperature. Substituting equations (III.22) and (III.23) for the principle stresses into equation (III.24) and performing a sequence of manipulations, it can be shown that the Mohr–Coulomb criterion is satisfied

at $r_c = 2f^2$ so that $\tan(2\psi) = -f^{-1}$. Previously unmobilized gouge is incorporated within an expanding zone that is poised for shear failure once r reaches r_c on its boundary and the Mohr circle intersects with the failure envelope (Figure III.4). This boundary can be tracked as the location where

$$\begin{aligned}\tau &= f(\sigma_n - p) \\ &= \frac{1-2\nu_d}{1-\nu_d}(1-\beta_s/\beta_d)\frac{\Delta p}{2f} + \frac{2(1+\nu_d)}{3(1-\nu_d)}\mu\lambda_s\frac{\Delta T}{2f}.\end{aligned} \tag{III.25}$$

In Figure III.5 we illustrate how the shear resistance $\tau = f(\sigma_n - p)$ and the driving force from poroelastic effects determine the mobilization, or Mohr–Coulomb boundary. Thermal pressurization increases the pore pressure and hydraulic diffusion controls its decrease towards ambient levels far from the shear zone, leading to corresponding decreases to the effective stress and hence the frictional strength. At the same time, pressure and temperature increases enhance the driving force for mobilization described by the right side of equation (III.25) as the symmetry plane is approached. Inside the Mohr–Coulomb boundary, the driving force is greater than the frictional strength that opposes shear so the granules throughout this region are poised for mobilization.

III.3.5. Distributed shear

We have shown that the Mohr–Coulomb boundary defines the region with the potential for failure. However, with velocity-weakening or rate neutral friction, the shear stress cannot be equated with the frictional strength $\tau(y,t) = f[\sigma_{\mathrm{n}} - p(y,t)]$ while simultaneously satisfying the momentum balance throughout this region. Figure III.5 suggests that force equilibrium would approximately hold with the near-constant values of frictional strength in a much thinner zone where the pore pressure gradient is negli-

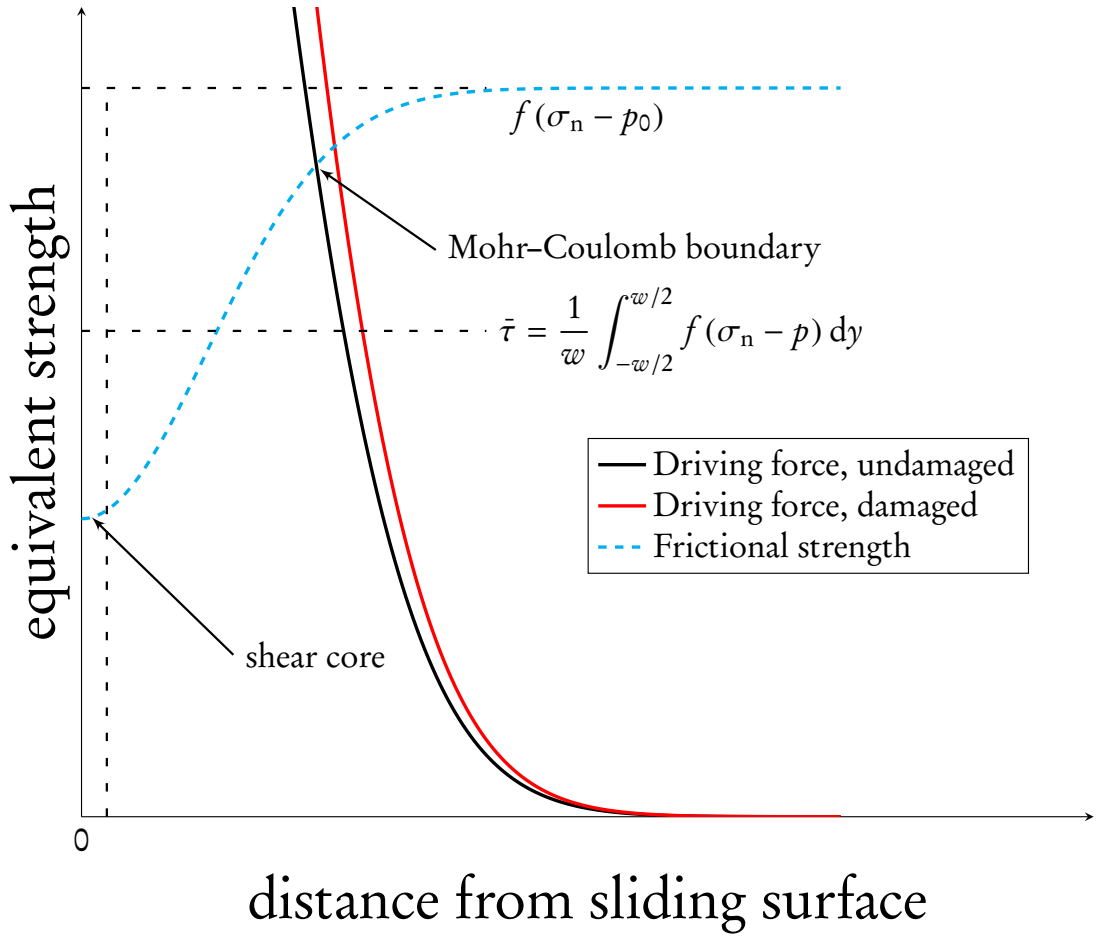

Figure III.5: A diagram of the Mohr–Coulomb boundary. The solid curves represent the driving force resulting from poroelastic effects when the fault is damaged and undamaged, which is a linear combination of pore pressure and temperature change. The dash curve is the frictional resisting force. The intersection is the boundary inside which Mohr–Coulomb failure will develop and material is poised to shear. The shear core boundary is where the shear stress $\tau = f(\sigma_n - p)$ starts to deviate significantly. The overall shear strength of the shear zone, however, lies between the minimum strength at the sliding surface and the ambient strength.

gible. However, between this "shear core" and the Mohr-Coulomb boundary, there is a significant gradient in frictional strength.

Since all potential contact surfaces inside the Mohr–Coulomb boundary are mechanically unstable, in principle slip could occur anywhere within this region. To avoid violating local momentum-balance constraints during sliding with the shear stress equal to the frictional strength, we suggest that shearing might be considered to take place along numerous instantaneous local shear zones that are thin, possibly planar, and transient. Over each local shear zone, pore pressure changes are small enough that fault-parallel frictional forces are approximately balanced. Our continuum modeling approach cannot capture all of the detailed mechanical interactions that take place at the granular scale, but we can define a strain-rate function that is designed to approximate the overall shearing behavior. Evidence that finite shear zones along natural faults do not deform uniformly throughout a particular slip event comes, for example, from detailed observations of the narrow bands gently inclined to the strike of the main fault, known as Riedel shears (Logan and Teufel, 1986). Laboratory observations of the force chains that arise in a shear zone full of granules (Daniels and Hayman, 2008) also exhibit notable transient local behavior that might be responsible for enabling the angles of Riedel structures to differ from the rotation angle ψ. We expect finite microstructures such as these to prohibit localization to the idealized mathematical plane predicted from linear-stability considerations in a continuum treatment.

We propose that distributed shear can be viewed as the superposition of numerous transient shears throughout the mechanically unstable region defined by the Mohr–Coulomb boundary. In a continuum treatment, the cumulative affect of this deformation can be approximated by defining a macroscopic strain-rate distribution. We examine two candidate distributions: (1) uniform shearing, in which transient shears are equally likely throughout the growing mechanically unstable region; and (2) Gaussian shearing,

in which transient shears occur preferentially in places where the effective stress is lowest. For the first case, we approximate a uniform strain-rate distribution by setting

$$\dot{\gamma}(y, w) = \frac{V}{2w} - \frac{V}{2w} \operatorname{erf}\left[k_\gamma \left(\frac{2|y|}{w} - 1\right)\right], \tag{III.26}$$

which approaches a step function with large $k_\gamma \sim 100$, and the shear zone thickness w is set by the Mohr–Coulomb boundary at $y = w/2$. For the second case, we use a Gaussian distribution centered on the symmetry plane and set the standard deviation to $\sigma = w/6$ so that the strain rate is negligible outside the shear zone,

$$\dot{\gamma}(y, w) = \sqrt{\frac{2}{\pi}} \frac{3V}{w \operatorname{erf}(3/\sqrt{2})} \exp\left(-\frac{18y^2}{w^2}\right). \tag{III.27}$$

Both equation (III.26) and (III.27) satisfy the integral kinematic constraint from equation (III.9). In this framework, the overall coseismic shear strength along the fault is the weighted integral of local strength

$$\bar{\tau} = \frac{1}{V} \int_{-\infty}^{\infty} f(\sigma_\mathrm{n} - p)\dot{\gamma} \, \mathrm{d}y. \tag{III.28}$$

For our prescribed uniform and Gaussian strain-rate distributions, $\dot{\gamma} \approx 0$ for $|y| > w/2$, so the overall shear strength is the equivalent uniform strength that would generate the same amount of frictional heat. This corresponds with the fault strength that would be inferred from long-term observations of the heat anomaly (e.g., Lachenbruch, 1980; Lachenbruch and Sass, 1980).

III.3.6. Effects of Damage

The essential equations that describe our model have already been presented. However, in choosing representative parameter values it is important to note that damage can play a central role in modifying local conditions during earthquakes. When a mature fault

is slipping, the ultracataclastic core where slip is concentrated can have altered poroelastic properties compared with the material outside the damaged zone (Evans et al., 1997; Wibberley and Shimamoto, 2003). New flow passages can form to increase both the permeability and compressibility as a result of: (a) fault dilatancy during coseismic slip (Marone et al., 1991) (b) breakage of water-swelling clays and alteration of veins formed during the interseismic period (Chester et al., 1993); (c) porosity increases due to elevated pore pressure (Seront et al., 1998; Lockner et al., 2000; Wibberley and Shimamoto, 2003; Mizoguchi et al., 2008); and (d) local fracturing and activation of the damage zone along and near the shear zone walls as a result of large stress fluctuations in the vicinity of the propagating rupture tip (Rice, 1980; Poliakov et al., 2002; Rice et al., 2005b; Faulkner and Armitage, 2013; Candela et al., 2014).

Within a damaged shear zone the drained compressibility is expected to increase and this affects the value of $\beta_n^{dmg} = (\beta_d^{dmg} - \beta_s)/n - \beta_s$, whereas we identify $\lambda_n^{dmg} \approx \lambda_n \approx \lambda_s$. We expect the damaged compressibility β_d^{dmg} to be significantly higher than the compressibility of the surrounding bulk framework β_d (Wibberley, 2002). When a contrast in these parameters takes place across the shear zone boundary, Λ and α_{hy} must also change. However, numerical tests demonstrate that expected contrasts in these parameters have a limited impact on the pore pressure evolution described by equation (III.5).

In the damaged region, the effective compressive stress takes the same form as equation (III.19), but β_d and ν_d are replaced by β_d^{dmg} and ν_d^{dmg}, defined as above with equation (III.20). If we follow Rice (2006) and let $\beta_d^{dmg} = 2\beta_d$, and keep all other parameters the same as those used for equation (III.21), the fault-parallel effective stress in the damaged zone is

$$-\sigma_{xx}^{dmg} - p \approx (\sigma_n - p) + 0.86\Delta p + 0.21\Delta T \text{ MPa/K}. \tag{III.29}$$

Comparison with equation (III.21) reveals that there is an enhanced contribution from pore pressure changes, while temperature changes are less important than when intact gouge parameters are employed. The analysis suggests that damage might produce appreciable changes in constitutive behavior and influence the propagation of the Mohr–Coulomb boundary. Depending on how the fault zone responds to the passage of the rupture tip, we can envision a fault zone where all properties are relatively unaffected, or a fault with damaged properties only in the shearing zone, or a fault that is totally damaged even in the unmobilized region. These three possibilities are explored further in the results section below.

III.4. Results

Using the parameters listed in Table III.2, we simulated the temperature and pore pressure evolution during coseismic shear described by equations (III.5), (III.7) and (III.8), fixing the strain-rate distribution with either equation (III.27) or (III.26), where the shear-zone width is required to satisfy equation (III.25). Details of the computational method are described more fully in Appendix B.2. Except where specified otherwise, for the illustrations that follow we initiate fault motion at constant sliding rate $V = 1$ m/s and impose an initial shear zone thickness of $w = 0.2$ mm, with a uniform weakened friction of $f = 0.2$. The strain inside the shear zone is assumed uniform, which is approximated using a smooth error function as in equation (III.26). We note that although our calculation specifies an arbitrary initial shear-zone thickness, Figure III.6 illustrates that different initial thickness values do not affect the thickness evolution at later times.

Figure III.7a shows how the temperature inside the shear zone increases, and Figure III.7b shows that the pore pressure approaches lithostatic conditions. Figure III.6 shows how the shear zone thickness is predicted to broaden and reach a finite thickness

Table III.2: Parameters used in the simulation. The thermal properties are typical values taken from Rice (2006) and Rempel and Weaver (2008) for novaculite.

Parameters		Value	Reference
V	(m/s)	1	
ρ	(g/cm^3)	2.65	Rempel and Weaver (2008)
C	(J/(kg°C))	732	*ibid.*
α_{th}	(mm^2/s)	2.2	*ibid.*
α_{hy}	(mm^2/s)	44	
p_0	(MPa)	70	Rice (2006)
T_0	(°C)	210	*ibid.*
σ_{n}	(MPa)	126	*ibid.*
Λ	(MPa/°C)	0.92	*ibid.*
β_d	(Pa^{-1})	5.8×10^{-11}	*ibid.*
β_s	(Pa^{-1})	1.6×10^{-11}	*ibid.*
μ	(GPa)	13	*ibid.*
λ_s	(°C^{-1})	2.4×10^{-5}	*ibid.*

that is similar in scale to that predicted by the idealized linear stability presented in Section III.2.3. However, in the present case the friction coefficient has been treated as constant and heat and fluid flow are integral to the model results, whereas the finite thicknesses predicted by the linear stability analysis were for rate-strengthening friction and a reference base state was chosen that neglected loss of heat and fluid. As the shear zone broadens in our model, heat is able to dissipate over larger gouge volumes and this has the effect of lowering the maximum temperature rise. As a result, only a modest temperature rise of less than 200 °C is predicted for the mid-plane of the shear zone. This is much lower than the case in which the thickness is kept constant (Figure III.8).

From Equation (III.25), the friction coefficient plays a central role in controlling the growth of the shear zone. Higher friction requires a larger increase in pore pressure and temperature for the Mohr–Coulomb criterion to be satisfied, and consequently results in a slower shear-zone growth, as demonstrated in Figure III.9. If the friction coefficient in the unmobilized gouge is assigned the higher value of 0.6 instead of the 0.2 used for

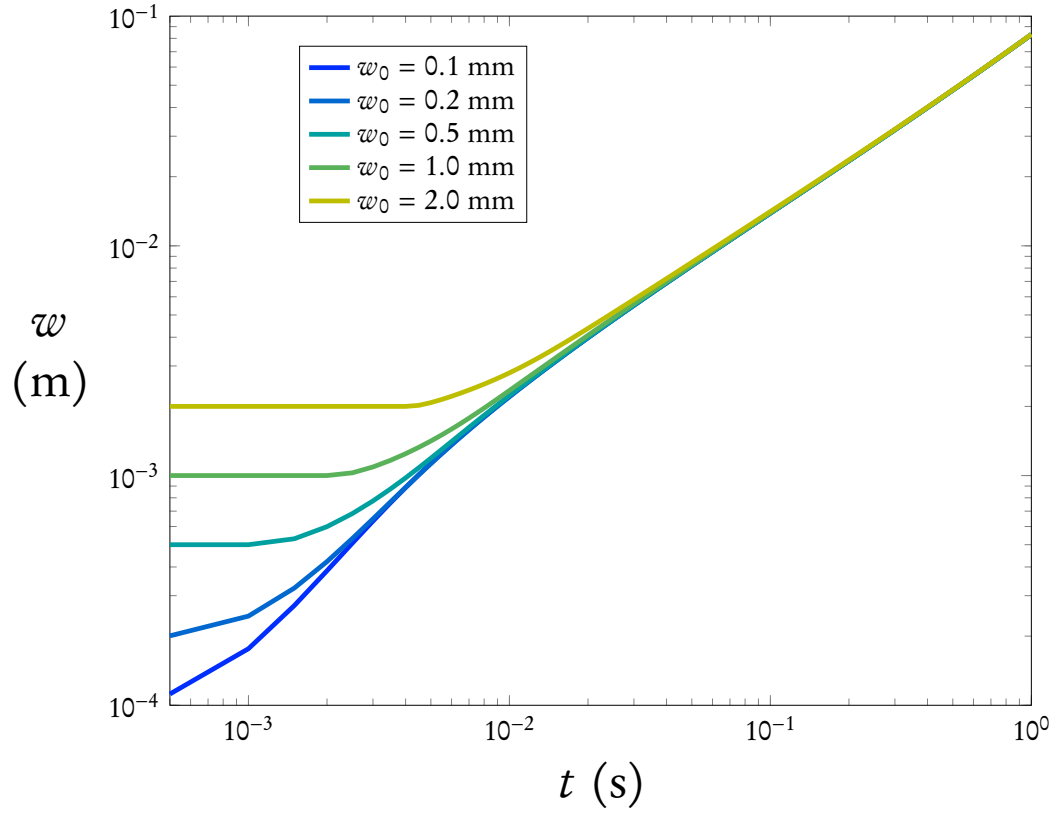

Figure III.6: Thickness evolution with different initial value. It is clear that as long as the initial value is much smaller than the final thickness, the curves will collapse to one after the starting period.

Figures III.7 and III.6, then the predicted shear-zone width after 1 s of slip is expected to drop from ~ 55 mm to ~ 15 mm.

The hydraulic diffusivity α_{hy} and thermal diffusivity α_{th} also have a significant influence on the model behavior. With higher hydraulic diffusivity, the pressurized fluid flows away much more easily so that the pore pressure perturbation expands outwards more rapidly, and this results in the correspondingly broader shear zones illustrated by Figure III.10. However, higher α_{hy} also improves shear-zone drainage so that the fault strength remains relatively high and more frictional heat is generated. In the calculations shown here, the net result is an increase to the maximum temperature (Figure III.11). If

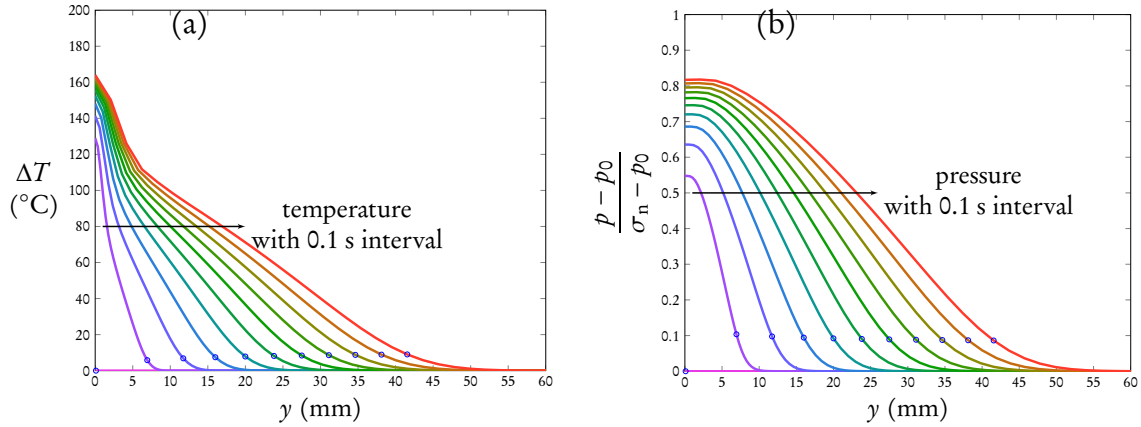

Figure III.7: Modeled evolution of (a) temperature and (b) normalized pore pressure evolution during 1 s using the Gaussian strain-rate distribution described by equation (III.27). The empty circles indicate the location of the Mohr–Coulomb boundary. The pore pressure perturbation propagates faster than the temperature perturbation, since α_{hy} is greater than α_{th}, as noted in Table III.2.

we use a Gaussian strain distribution, the higher strain rate concentrated near the central plane will lead to a larger temperature rise, but it is still relative modest (~ 300°C).

III.5. Discussion

III.5.1. Modest temperature rise

When the shear zone broadens with time, the sliding plane where maximum temperature occurs undergoes a smaller temperature rise than would be expected if the thickness were assumed fixed at its initial value. It is possible that shear-zone broadening might dissipate sufficient heat to be partially responsible for preventing macroscopic melting and explaining the apparent lack of pseudotachylytes along mature faults. In Figure III.11 we can see that when the ambient temperature is 210°C (a typical ambient value for a fault at 7 km depth) the maximum temperature rise in the shear zone is around 250°C, which keeps the temperature in the shear zone lower than the melting temperature for common fault constituents (i.e. ~ 1000°C). Moreover, because the coseismic temperature rise

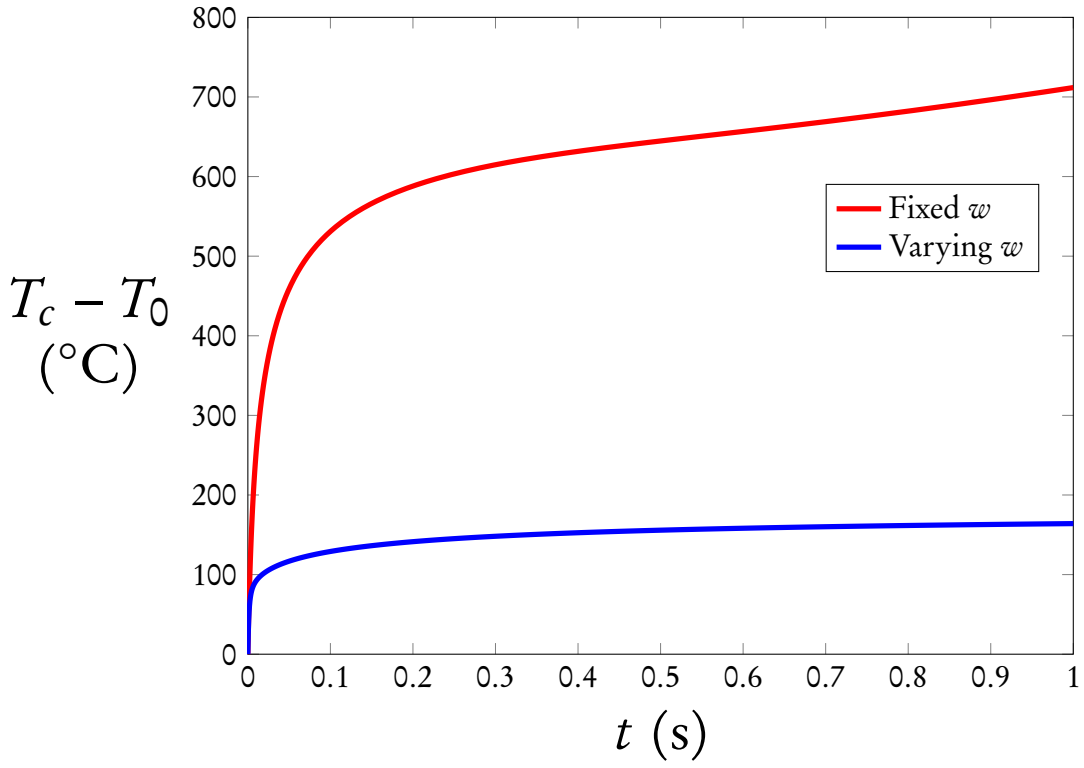

Figure III.8: The temperature rise on the central plane for varying shear zone thickness (blue) and fixed shear zone thickness. With an expanding shear zone, the temperature rise barely reached 200 °C, but it will reach about 800 °C if the shear zone is not expanding.

can sometimes be inferred or at least bounded from petrological analyses and laboratory experiments (e.g Kuo et al., 2011; den Hartog et al., 2012; Rowe et al., 2012), predictions of shear zone thickness and observations along well-characterized faults also hold potential as a test of model behavior.

Similarly, in recent JFAST studies, the abundance of smectite (Ujiie et al., 2013) suggests that the temperature on the Tohoku-Oki megathrust never became very high enough (~ 200° C) for illitization to occur (Pollastro, 1993). This observation is not consistent with existing models, which tend to predict much higher temperature (Fulton et al., 2013). Although it is still very challenging for our model to reach this low temperature, our model does efficiently limit the highest temperature in the shear zone.

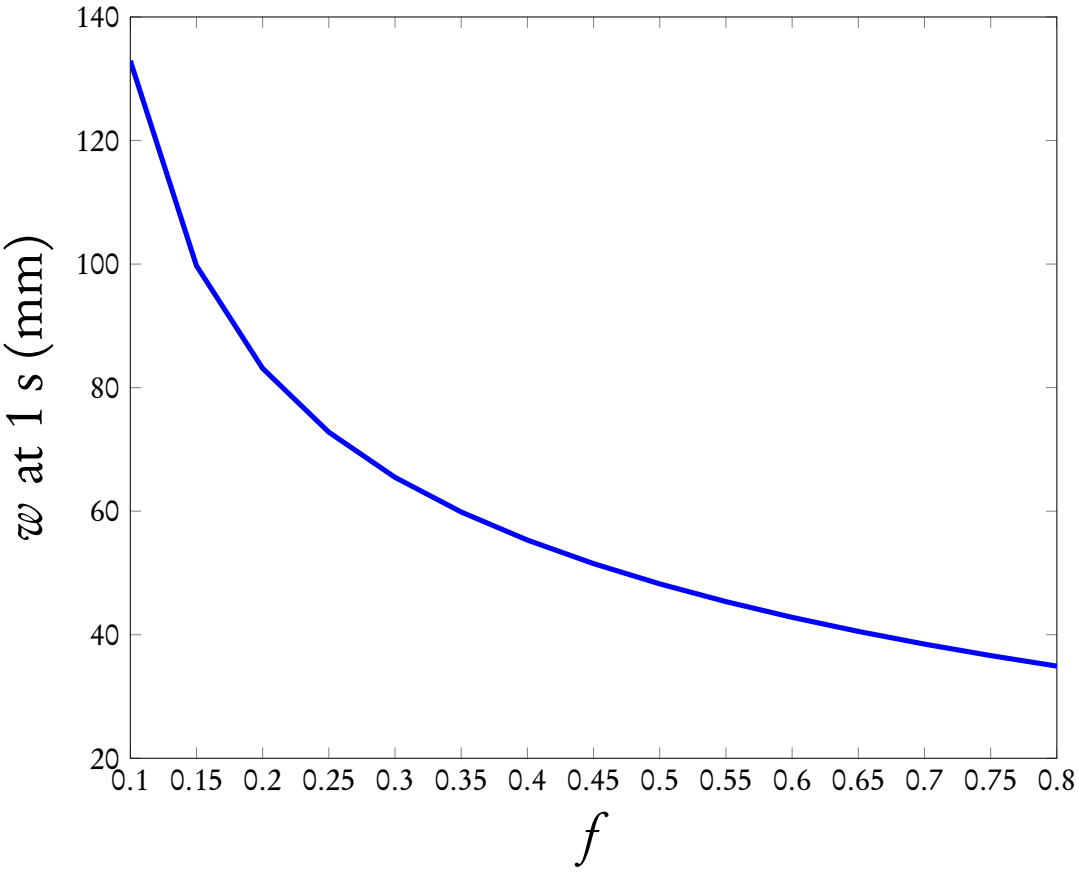

Figure III.9: Shear zone thickness at 1 s with different friction value. As the friction increases, it becomes more difficult for the shear zone to expand. But still, the shear zone expands even with high friction.

III.5.2. Other frictional behavior

It must be noted that although we calculate using a constant friction, this model can work with other friction constitutive laws. For example, our model predicts very high pore pressure, so we expect the rate-strengthening observed in granular systems at low effective stress (e.g., Kuwano and Hatano, 2011) may also play an important role in causing shear zone broadening and limiting further temperature increases. At the same time, various mechanisms may also decrease the friction, such as the solid-state transitions that produce weaker mineral phases (Kohli et al., 2011), enhanced plastic yielding at

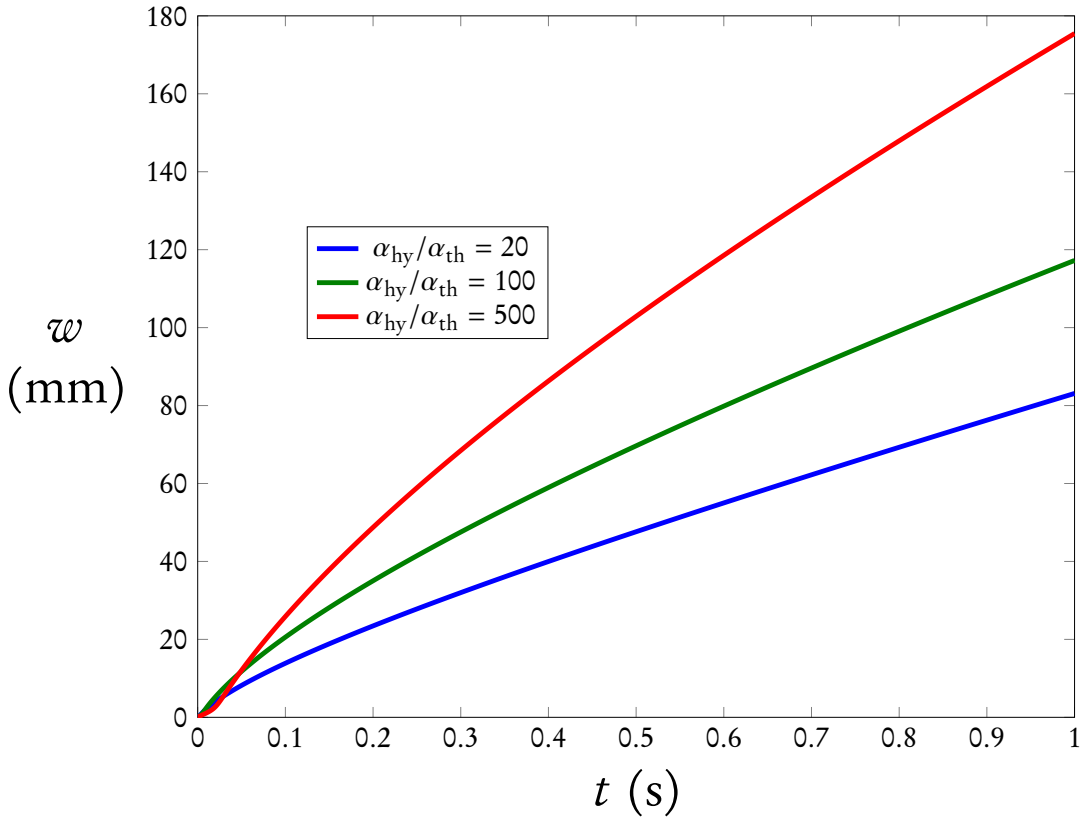

Figure III.10: Shear zone thickness increases when the ratio of α_{hy}/α_{th} changes from 20 to 500. Higher α_{hy} allows faster propagation of the pore pressure perturbation, which facilitates the mobilization.

elevated temperatures (Brown and Fialko, 2009), or mechanical lubrication by silica gel (Di Toro et al., 2004; Goldsby and Tullis, 2011). There are also models which features a transition from rate-weakening to rate-strengthening at coseismic slip rates.

In FigureIII.11, we compare the maximum temperature with constant friction with the results using a friction constitutive law with a temperature dependence (Chen and Rempel, 2014) (see Chapter II). As the friction decreases with increasing temperature, the frictional heat is reduced, and the maximum temperature is decreased. As for the shear zone thickness, we have already shown that the friction can control the shear zone growth rate, so changes in friction models will influence the shear zone growth, but the

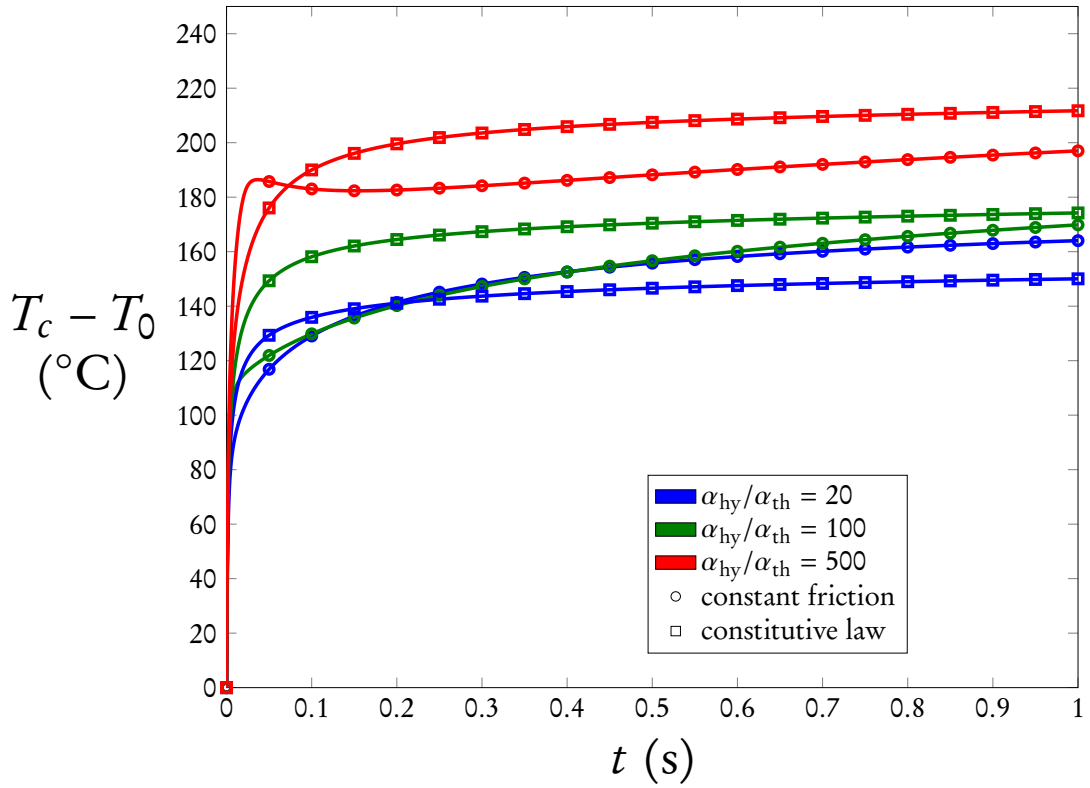

Figure III.11: Maximum temperature in the shear zone thickness increases when the ratio of α_{hy}/α_{th} changes from 20 to 500. Higher α_{hy} keeps the shear zone more drained, and maintains higher heat generation. When the friction weakens with temperature according to the constitutive law developed in Chapter II, the temperature is reduced because less heat is generated.

shear zone will broaden nevertheless. In Appendix B.3 we have further discussion on the asymptotic behavior of the shear zone thickness, and we can show for a reaction-diffusion system as our model, the shear zone thickness always tends to converge to a steady value, either a finite thickness or zero.

III.6. Conclusion

In this work we have summarized our mechanical model, which explores the effects of poroelasticity on the expansion of shear zone thickness and demonstrates that its role

in limiting temperature rise agrees with field and experimental observations of finite shear zones, and helps to explain the lack of pseudotachylytes in exhumed faults and the abundance of smectite along the Tohoku-Oki fault at 800 mbsf. Based on rate-strengthening friction and thermal-pressurization, stress variations induced by poroelasticity cause the development of a zone that is unstable to shear, which propagates into the undeformed surrounding gouge and causes mobilization to occur. We acknowledge that this mechanism is only one possible process among the various mechanical and chemical mechanisms occurring during earthquakes, but we argue that similar results can be obtained as long as the shear zone is described as a reaction-diffusion system.

CHAPTER IV

CONCLUSIONS

In this dissertation we have developed theoretical and numerical models to simulate fault strength evolution, and help to unravel some of the complicated processes that occur during earthquakes. As shown in Chapter II and III, we break the problem into different scales, and build our model upon the basic physics with reasonable assumptions. Although our modeling is idealized and involves considerable simplifications such as the use of the spatially independent parameters, we obtain results consistent with field and laboratory observations, and our models have the potential to explain observations that previous models do not. I will end my dissertation by summarizing the conclusions and implications, and discussing the next steps in this research.

IV.1. Dissertation Summary

In Chapter II, I start from a simple micromechanical model of asperity contacts to obtain the average shear resistance of a contact surface. The model is then compared with published experimental data to confirm that the fit results are consistent with a priori parameter estimates. As pointed out in Section II.4.2, although each asperity is weakened over time, the overall friction can still be rate strengthening. In the modeling, the asperity weakening is attributed to melt layer development, but in fact other weakening

mechanisms for asperities can also lead to rate-strengthening.

The fault strength evolution is the main topic in Chapter III, and I develop a model which allows the shear zone thickness to evolve during earthquakes. The overall fault strength is treated as the collective effect of the shear resistance between the granules, but unlike in Chapter II, we are faced with a discrepancy. We can view the fault zone as a continuum in which the fault strength is spatially uniform, or we can view the fault zone as consisting of numerous granules and the fault strength is only the average of the shear resistance on the contact surfaces of granules. We mitigate the difference between the two views by considering the cumulative effect of numerous transient shear events, and obtain results that are consistent with observations from the field and experiments.

IV.2. Future Research

IV.2.1. Effects of inhomogeneity and anisotropy

Our models are based on simplified physical assumptions, but in the real world, whether these assumptions always hold is questionable. One big simplification we made in all the models is that fault materials are homogeneous, and the properties are isotropic. As we have discussed in previous chapters, inhomogeneities can cause appreciable change in the model. It is expected that inhomogeneities can have different influences on different scales. First, in Chapter II we compared our model against experimental data which were obtained using both monomineralic rocks (quartzite and novaculite) and polymineralic rocks (granite and gabbro). We used averaged parameters from Rempel and Weaver (2008), which approximate the contributions from minor constituents. We also discussed the effects of anisotropy of the thermal properties of quartz, and argued that it does not affect the model. In Chapter III, however, the comminution during earthquakes will result in significant changes in hydraulic properties near the shear core. We showed that the

ratio of $\alpha_{\mathrm{hy}}/\alpha_{\mathrm{th}}$ has a strong control on the maximum temperature and the shear zone thickness, but in fact this ratio is expected to vary across the shear zone, and depend on the slip history. A model that incorporates the evolution of permeability will be helpful for understanding the kinematics of fault during earthquakes.

IV.2.2. Shear Resistance from Stick-Slip Movement

Laboratory observations found that shearing is not uniformly distributed in the thin shear zone (Dieterich, 1981). Instead, slip propagates throughout the whole damaged zone in a "stick-slip" pattern, and the shear core is a region where slip occurs more often. In Chapter III, we interpreted the distributed fault shearing as the superstition of numerous transient shears on the granular contact surfaces inside the Mohr–Coulomb boundary, but in our model the shear resistance on these transient shearing interfaces does not explicitly take into account the stick-slip movement. When an interface is "stuck", the resistance is the static frictional strength, which can be significantly greater than the dynamic frictional strength when the interface is slipping, and when the interface begins slipping, the episodic movement of the granules can result in significant stress drops (Daniels and Hayman, 2008). It is possible to allow stick-slip to occur in our shear zone broadening model, and see what changes the stick-slip movement will bring in the results.

IV.2.3. Continental-Scale Simulation with Fault Strength Model

It will be very helpful to actually apply the fault strength model we developed in a continental scale simulation. I have begun a finite element modeling of the Cascadia subdution zone, and I have summarized the technical details of this project in Appendix C. The models presented in previous chapters focus on the coseismic deformation, but if we incorporate the history-dependent evolution of fault parameters, it is possible to simulate

how the fault strength will change the interseismic deformation in a long earthquake cycle.

APPENDIX A

SUPPLEMENTAL INFORMATION FOR CHAPTER II

A.1. Numerical Approach

We first normalize the equations by defining

$$\tilde{T} = \frac{T - T_{\text{amb}}}{T_w - T_{\text{amb}}},\ \tilde{y} = \frac{y}{D}\sqrt{\frac{DV_w}{\pi\alpha}},\ \tilde{v} = \frac{\pi V}{V_w},\ \text{and}\ \tilde{t} = \frac{tV_w}{\pi D}.$$

The initial temperature profile for $|\tilde{y}| > \tilde{w}_0/2$ from equation (II.10) is

$$\tilde{T}(\tilde{t}_w, \tilde{y}) = \tilde{v}\left[\sqrt{\frac{\tilde{t}_w}{\pi}}\exp\left(-\frac{\tilde{y}^2}{4\tilde{t}_w}\right) - \frac{\tilde{y}}{2}\text{erfc}\left(\frac{\tilde{y}}{2\sqrt{\tilde{t}_w}}\right)\right],$$

while for $|\tilde{y}| < \tilde{w}_0/2$, equation (II.12) gives

$$\tilde{T}(\tilde{t}_w, \tilde{y}) = 1 + \tilde{v}\frac{\left(\tilde{w}_0^2 - 4\tilde{y}^2\right)}{8\tilde{w}_0}\text{erfc}\left(\frac{\tilde{w}_0}{4\sqrt{\tilde{t}_w}}\right).$$

The initial position of the phase boundary is set by $\tilde{w}_0/2 = R\tilde{v}/2$, where R is defined as

$$R = \frac{\eta\alpha\rho^3 C^3 (T_w - T_{\text{amb}})^3}{D^2\tau_c^4} = \frac{V_w^2}{\pi V_p^2}.$$

From (II.14), the normalized governing equations become

$$\frac{\partial \tilde{T}}{\partial \tilde{t}} = \frac{\partial^2 \tilde{T}}{\partial \tilde{y}^2} + \frac{R\tilde{v}^2}{\tilde{w}^2}, \quad 0 < \tilde{y} < \tilde{w}/2, \tag{A.1}$$

$$\frac{\partial \tilde{T}}{\partial \tilde{t}} = \frac{\partial^2 \tilde{T}}{\partial \tilde{y}^2}, \quad \tilde{y} > \tilde{w}/2. \tag{A.2}$$

These must be solved subject to the Stefan condition from equation (II.15)

$$\frac{S}{2}\frac{\mathrm{d}\tilde{w}}{\mathrm{d}\tilde{t}} = \left.\frac{\partial \tilde{T}}{\partial \tilde{y}}\right|_{\tilde{w}/2^+} - \left.\frac{\partial \tilde{T}}{\partial \tilde{y}}\right|_{\tilde{w}/2^-},$$

and the boundary conditions

$$\left.\frac{\partial \tilde{T}}{\partial \tilde{y}}\right|_{\tilde{y}=0} = 0, \quad \tilde{T}|_{\tilde{w}/2} = 1, \text{and} \quad \tilde{T}|_{\tilde{y}\to\infty} = 0.$$

From the solution to these equations we obtain the evolution of the weak layer thickness and calculate the macroscopic friction from equation (II.17) as

$$\mu/f_0 = \tilde{v}\tilde{t}_w + R\tilde{v}^2 \int_{\tilde{t}_w}^{1/\tilde{v}} \frac{\mathrm{d}\tilde{t}}{\tilde{w}}. \tag{A.3}$$

For our numerical scheme, we transform the space variables to fix the moving boundary, then discretize using centered differences in space and solve for the time evolution at the nodal locations using the `ode` toolbox in Matlab. The moving boundary is fixed by variable transform $\xi = 2\tilde{y}/\tilde{w}$ and $\tau = \tilde{t}$. We divide the domain $[0, \infty)$ into three parts: $[0, \tilde{w}/2)$, $[\tilde{w}/2, Z\tilde{w}/2]$ and $[Z\tilde{w}/2, \infty)$. When $y \in [0, Z\tilde{w}/2)$, ξ_i are equally spaced, and when $\tilde{y} \in [Z\tilde{w}/2, \infty)$, we use a different transform $\zeta = Z\tilde{w}/(2\tilde{y}) \in (0, 1]$. We use M intervals within $\tilde{w}/2$ and $M + N$ intervals within $\tilde{y} < Z\tilde{w}/2$. By choosing $M + N + 1$ intervals in $[Z\tilde{w}/2, \infty)$ we ensure that for equally spaced ζ_j, the first interval in $[Z\tilde{w}/2, \infty)$ has the same size $\tilde{w}/(2M)$ as all the intervals at smaller $\tilde{y}$.

The transformed equations are

$$\frac{\partial \tilde{T}}{\partial \tau} = \xi\Gamma\frac{\partial \tilde{T}}{\partial \xi} + \frac{4}{\tilde{w}^2}\frac{\partial^2 \tilde{T}}{\partial \xi^2} + \frac{R\tilde{v}^2}{\tilde{w}^2}, \quad 0 \le \xi \le 1, \tag{A.4}$$

$$\frac{\partial \tilde{T}}{\partial \tau} = \xi\Gamma\frac{\partial \tilde{T}}{\partial \xi} + \frac{4}{\tilde{w}^2}\frac{\partial^2 \tilde{T}}{\partial \xi^2}, \quad 1 < \xi \le Z, \tag{A.5}$$

$$\frac{\partial \tilde{T}}{\partial \tau} = \left(\frac{8\zeta^3}{Z^2\tilde{w}^2} - \zeta\Gamma\right)\frac{\partial \tilde{T}}{\partial \zeta} + \frac{4\zeta^4}{Z^2\tilde{w}^2}\frac{\partial^2 \tilde{T}}{\partial \zeta^2}, \quad 0 < \zeta < 1, \tag{A.6}$$

where $\Gamma = (1/\tilde{w})\mathrm{d}\tilde{w}/\mathrm{d}\tau$ is the scaled growth rate of the melt zone. The boundary conditions are

$$\left.\frac{\partial \tilde{T}}{\partial \xi}\right|_{\xi=0} = 0, \quad \tilde{T}|_{\xi=1} = 1, \text{and} \quad \tilde{T}|_{\zeta\to 0} = 0,$$

and the Stefan condition becomes

$$\frac{\mathrm{d}\tilde{w}}{\mathrm{d}\tau} = \frac{4}{S\tilde{w}}\left(\left.\frac{\partial \tilde{T}}{\partial \xi}\right|_{\xi=1^+} - \left.\frac{\partial \tilde{T}}{\partial \xi}\right|_{\xi=1^-}\right).$$

All calculations shown here were performed with $M = 5$ and $N = 5000$.

A.2. Self-similar solutions

By setting $\tilde{y} = 2\xi\sqrt{\tilde{t}}$, $\tilde{w} = 2\lambda\sqrt{\tilde{t}}$, the governing equations now become

$$-\xi\frac{\mathrm{d}\tilde{T}}{\mathrm{d}\xi} = \frac{1}{2}\frac{\mathrm{d}^2\tilde{T}}{\mathrm{d}\xi^2} + \frac{R\tilde{v}^2}{2\lambda^2}, \quad 0 < \xi < \lambda/2,$$

$$-\xi\frac{\mathrm{d}\tilde{T}}{\mathrm{d}\xi} = \frac{1}{2}\frac{\mathrm{d}^2\tilde{T}}{\mathrm{d}\xi^2}, \quad \xi > \lambda/2.$$

Assume $\tilde{T}$ for $0 < \xi < \lambda/2$ has a solution

$$\frac{\mathrm{d}\tilde{T}}{\mathrm{d}\xi} = C(\xi)e^{-\xi^2},$$

which gives

$$C(\xi) = -\frac{R\tilde{v}^2}{\lambda^2}\int_0^{\xi} e^{\xi_1^2}\mathrm{d}\xi_1 = -\frac{\sqrt{\pi}R\tilde{v}^2}{2\lambda^2}\,\mathrm{erfi}(\xi),$$

and

$$\tilde{T}(\xi < \lambda/2) = 1 + \frac{\sqrt{\pi} R \tilde{v}^2}{2\lambda^2} \int_{\xi}^{\lambda/2} \mathrm{erfi}(\xi_1) e^{-\xi_1^2} \mathrm{d}\xi_1.$$

For $\xi > \lambda/2$, the solution is

$$\tilde{T} = \frac{\mathrm{erf}(\xi) - 1}{\mathrm{erf}(\lambda/2) - 1}.$$

At the weakening boundary, if there is no phase change,

$$\frac{\mathrm{d}\tilde{T}}{\mathrm{d}\xi}\Big|_{\lambda/2+0} = \frac{\mathrm{d}\tilde{T}}{\mathrm{d}\xi}\Big|_{\lambda/2-0},$$

which is

$$\frac{\pi^2 V^2}{2\lambda^2 V_p^2} \mathrm{erfi}(\lambda/2) - \frac{2}{\mathrm{erfc}(\lambda/2)} = 0,$$

for $V = 1\,\mathrm{m/s}$, $V_p = 20\,\mathrm{m/s}$, $\lambda \approx 0.0035$. The friction is calculated by

$$\mu/\mu_0 = \tilde{v}\tilde{t}_w + R\tilde{v}^2 \int_{\tilde{t}_w}^{1/\tilde{v}} \frac{\mathrm{d}\tilde{t}}{\tilde{w}} = \tilde{v}\tilde{t}_w + \frac{\pi V^2}{V_p^2 \lambda} \sqrt{\tilde{t}}\Big|_{\tilde{t}_w}^{1/\tilde{v}}$$

The treatments above also apply to the melting scenario.

It should be noted that the solution within the weak layer can be expressed in a series

$$\int_0^x \mathrm{erfi}(\xi) e^{-\xi^2} \mathrm{d}\xi \approx \frac{1}{\sqrt{\pi}} \left(x^2 - \frac{x^4}{3} + \frac{4x^6}{45} + O(x^7) \right),$$

so as a first-order approximation,

$$\tilde{T}(\xi < \lambda/2) = 1 + \frac{R\tilde{v}^2(\lambda^2 - 4\xi^2)}{8\lambda^2},$$

which is a parabolic profile.

APPENDIX B

SUPPLEMENTAL INFORMATION FOR CHAPTER III

B.1. Linear stability analysis

From the conservation of energy (III.6), we assume a uniform shear distribution, with strain rate $\dot{\gamma} = V/w$ within the gouge zone. Defining the thermal diffusivity as $\alpha_{\mathrm{th}} \equiv K/(\rho C)$, the temperature evolution within the gouge zone $|y| \leq w/2$ is

$$T_t = \alpha_{\mathrm{th}} T_{yy} + \frac{fV}{\rho C h}[\sigma_{\mathrm{n}} - p_0(t)], \quad |y| \leq w/2, \tag{B.1}$$

while outside the gouge zone, since there is no heat source, the temperature evolution is

$$\frac{\partial T}{\partial t} = \alpha_{\mathrm{th}} \frac{\partial^2 T}{\partial y^2}, \quad |y| > w/2. \tag{B.2}$$

Here we assume that the thermal diffusivity in the ambient rocks and in the gouge zone is the same.

The conservation of fluid mass is described in equation (III.4). Changes to the porosity n can have both elastic and plastic components, $\mathrm{d}n = \mathrm{d}n^{\mathrm{elastic}} + \mathrm{d}n^{\mathrm{plastic}}$. To simplify the derivation, we assume $\mathrm{d}n^{\mathrm{plastic}} \approx 0$. We introduce the compressibility β and the expansivity λ for the fluid (subscript f), and porosity (subscript n) as

$$\beta_{\mathrm{n}} = \frac{1}{n}\frac{\partial n}{\partial p},\ \beta_{\mathrm{f}} = \frac{1}{\rho_{\mathrm{f}}}\frac{\partial \rho_{\mathrm{f}}}{\partial p},\ \lambda_{\mathrm{n}} = \frac{1}{n}\frac{\partial n}{\partial T},\ \lambda_{\mathrm{f}} = -\frac{1}{\rho_{\mathrm{f}}}\frac{\partial \rho_{\mathrm{f}}}{\partial T},$$

so

$$\frac{\partial n}{\partial t} = \frac{\partial n}{\partial p}\frac{\partial p}{\partial t} + \frac{\partial n}{\partial T}\frac{\partial T}{\partial t} = n\beta_{\mathrm{n}}\frac{\partial p}{\partial t} + n\lambda_{\mathrm{n}}\frac{\partial T}{\partial t} \tag{B.3}$$

$$\frac{\partial \rho_{\mathrm{f}}}{\partial t} = \frac{\partial \rho_{\mathrm{f}}}{\partial p}\frac{\partial p}{\partial t} + \frac{\partial \rho_{\mathrm{f}}}{\partial T}\frac{\partial T}{\partial t} = \rho_{\mathrm{f}}\beta_{\mathrm{f}}\frac{\partial p}{\partial t} - \rho_{\mathrm{f}}\lambda_{\mathrm{f}}\frac{\partial T}{\partial t} \tag{B.4}$$

and (III.4) can be rewritten as

$$\begin{aligned}\frac{\partial \rho_{\mathrm{f}} n}{\partial t} &= \frac{\partial \rho_{\mathrm{f}}}{\partial t} n + \rho_{\mathrm{f}}\frac{\partial n}{\partial t} \\ &= \rho_{\mathrm{f}} n\left[(\beta_{\mathrm{f}} + \beta_{\mathrm{n}})\frac{\partial p}{\partial t} + (-\lambda_{\mathrm{f}} + \lambda_{\mathrm{n}})\frac{\partial T}{\partial t}\right] \\ &= \frac{\partial}{\partial y}\left(\frac{\rho_{\mathrm{f}} k}{\eta_{\mathrm{f}}}\frac{\partial p}{\partial y}\right).\end{aligned}$$

Treating the fluid density ρ_{f} and fluid diffusivity $\alpha_{\mathrm{hy}} = k/[\eta_{\mathrm{f}} n(\beta_{\mathrm{f}} + \beta_{\mathrm{n}})]$ as spatially uniform, this simplifies further to

$$\frac{\partial p}{\partial t} - \Lambda\frac{\partial T}{\partial t} = \alpha_{\mathrm{hy}}\frac{\partial^2 p}{\partial y^2} \tag{B.5}$$

where $\Lambda = \dfrac{\lambda_{\mathrm{f}} - \lambda_{\mathrm{n}}}{\beta_{\mathrm{f}} + \beta_{\mathrm{n}}}$, and we use α_{hy} to describe the hydraulic diffusivity outside the gouge zone as well.

The entire domain starts with a uniform ambient temperature and a hydrostatic pressure use

$$T(y, 0) = T_{\mathrm{amb}}, \quad p(y, 0) = p_0.$$

In the far field negligible heat and fluid disturbance occur so the temperature and pressure remain unchanged at

$$T(\infty, t) = T_{\text{amb}}, \quad p(\infty, t) = p_0.$$

The model is symmetric with respect to the central plane, so we also have

$$\left.\frac{\partial T}{\partial y}\right|_{y=0} = \left.\frac{\partial p}{\partial y}\right|_{y=0} = 0.$$

Neglecting inertia, the momentum conservation requires that

$$\frac{\partial}{\partial y}[f(\sigma_{\text{n}} - p)] = 0. \tag{B.6}$$

In the base state, we assume the velocity, pressure and temperature correspond with conditions for undrained, adiabatic, uniform shear so that

$$V(y, t) = V_0(y) = \dot{\gamma}_0 y,$$
$$p(y, t) = p_0(t),$$
$$T(y, t) = T_0(t),$$

and (B.6) is satisfied automatically. The other two governing equations become

$$\frac{\partial T_0}{\partial t} = \frac{\dot{\gamma}_0 f(\dot{\gamma}_0, T_0)}{\rho c}(\sigma_{\text{n}} - p_0) = \frac{\dot{\gamma}_0 \tau_0}{\rho c},$$
$$\frac{\partial p_0}{\partial t} = \Lambda \frac{\partial T_0}{\partial t}.$$

If we let $f_0 = f(\dot{\gamma}_0, T_{\text{amb}})$ and $H = \dfrac{f_0 \Lambda}{\rho\, c}$, then

$$\frac{\partial T_0}{\partial t} = \frac{\dot{\gamma}_0 \tau_0 H}{\Lambda f_0}, \quad \frac{\partial p_0}{\partial t} = \frac{\dot{\gamma}_0 \tau_0 H}{f_0}.$$

With small perturbations around T_{amb} and $\dot{\gamma}_0$, the friction coefficient is

$$f(\dot{\gamma}, T_0) \doteq f(\dot{\gamma}_0, T_{\text{amb}}) + \left.\frac{\partial f}{\partial \dot{\gamma}}\right|_{\dot{\gamma}_0, T_0} (\dot{\gamma} - \dot{\gamma}_0) + \left.\frac{\partial f}{\partial T}\right|_{\dot{\gamma}, T_{\text{amb}}} (T_0 - T_{\text{amb}}),$$

and the equations above can be approximated as

$$\frac{\partial T_0}{\partial t} = \left[1 + \frac{f_T}{f_0}(T_0 - T_{\text{amb}})\right](\sigma_{\text{n}} - p_0)\frac{\dot{\gamma}_0 H}{\Lambda}, \tag{B.7}$$

$$\frac{\partial p_0}{\partial t} = \left[1 + \frac{f_T}{f_0}(T_0 - T_{\text{amb}})\right](\sigma_{\text{n}} - p_0)\dot{\gamma}_0 H. \tag{B.8}$$

If we define a time scale τ_p such that

$$\frac{1}{\tau_p} = \left[1 + \frac{f_T}{f_0}(T_0 - T_{\text{amb}})\right]\dot{\gamma}_0 H$$

then (B.8) gives

$$\begin{aligned}
\sigma_{\text{n}} - p_0(t) &= \bar{\sigma}_{\text{n}} \exp\left(-\int_0^t \frac{\mathrm{d}u}{\tau_p}\right) \\
&= \bar{\sigma}_{\text{n}} \exp\left[-\frac{t}{\tau_p} - \frac{t^2}{2}\left(\frac{1}{\tau_p}\right)'\Big|_{\xi}\right] \\
&= \bar{\sigma}_{\text{n}} \exp(-t/\tau_p) \exp\left[\frac{t^2}{2}\left(\frac{1}{\tau_p}\right)'\Big|_{\xi}\right],
\end{aligned}$$

where $\xi \in [0, t]$. When $t^2(1/\tau_p)'/(t/\tau_p) = (t/\tau_p)(\mathrm{d}\tau_p/\mathrm{d}t) = O(1)$, the residue can be neglected, and the equations can be further simplified as

$$\sigma_{\text{n}} - p_0(t) = \bar{\sigma}_{\text{n}} \exp(-t/\tau_p),$$

and

$$\frac{\partial T_0}{\partial t} = \frac{\bar{\sigma}_{\text{n}}}{\Lambda \tau_p} \exp(-t/\tau_p).$$

Imposing small perturbations, designated with subscript 1,

$$V(y,t) = V_0(y) + V_1(y,t) = \dot{\gamma}_0 y + V_1(y,t),$$

$$p(y,t) = p_0(t) + p_1(y,t),$$

and $$T(y,t) = T_0(t) + T_1(y,t),$$

the governing equations can be rewritten as

$$\begin{aligned}
0 &= (\sigma_n - p_0)\frac{\partial}{\partial y}\left(f_{\dot{\gamma}}\frac{\partial V_1}{\partial y} + f_T T_1\right) \\
&\quad - [f_0 + f_{\dot{\gamma}}(\gamma - \dot{\gamma}_0) + f_T(T_0 - T_{amb})]\frac{\partial p_1}{\partial y}, \\
\frac{\partial T_1}{\partial t} &= \frac{H}{\Lambda}\left[1 + \frac{f_{\dot{\gamma}}}{f_0}(\dot{\gamma} - \dot{\gamma}_0) + \frac{f_T}{f_0}(T_0 - T_{amb})\right](\sigma_n - p_0)\frac{\partial V_1}{\partial y} \\
&\quad + \frac{H\dot{\gamma}_0}{\Lambda}\left(\frac{f_{\dot{\gamma}}}{f_0}\frac{\partial V_1}{\partial y} + \frac{f_T}{f_0}T_1\right)(\sigma_n - p_0) \\
&\quad - \frac{H\dot{\gamma}_0}{\Lambda}\left[1 + \frac{f_T}{f_0}(T_0 - T_{amb})\right]p_1 + \alpha_{th}\frac{\partial^2 T_1}{\partial y^2}, \\
\text{and} \quad \frac{\partial p_1}{\partial t} &= \alpha_{hy}\frac{\partial^2 p_1}{\partial y^2} + \Lambda\frac{\partial T_1}{\partial t},
\end{aligned}$$

where the term $f_{\dot{\gamma}}(\gamma - \dot{\gamma}_0)$ can be ignored because $\gamma - \dot{\gamma}_0 = \partial V_1/\partial y$ is infinitesimal. Then the simplified equations are

$$\begin{aligned}
0 &= (\sigma_n - p_0)\frac{\partial}{\partial y}\left(f_{\dot{\gamma}}\frac{\partial V_1}{\partial y} + f_T T_1\right) \\
&\quad - [f_0 + f_T(T_0 - T_{amb})]\frac{\partial p_1}{\partial y}, \\
\frac{\partial T_1}{\partial t} &= \frac{H}{\Lambda}\left[1 + \frac{f_T}{f_0}(T_0 - T_{amb})\right](\sigma_n - p_0)\frac{\partial V_1}{\partial y} \\
&\quad + \frac{H\dot{\gamma}_0}{\Lambda}\left(\frac{f_{\dot{\gamma}}}{f_0}\frac{\partial V_1}{\partial y} + \frac{f_T}{f_0}T_1\right)(\sigma_n - p_0) \\
&\quad - \frac{H\dot{\gamma}_0}{\Lambda}\left[1 + \frac{f_T}{f_0}(T_0 - T_{amb})\right]p_1 + \alpha_{th}\frac{\partial^2 T_1}{\partial y^2}, \\
\text{and} \quad \frac{\partial p_1}{\partial t} &= \alpha_{hy}\frac{\partial^2 p_1}{\partial y^2} + \Lambda\frac{\partial T_1}{\partial t}.
\end{aligned}$$

We next express the perturbations in the form

$$p_1 = \hat{p}_1 \exp(s\,t)\, \exp\left(\frac{2\pi i y}{\lambda}\right),$$
$$T_1 = \hat{T}_1 \exp(s\,t)\, \exp\left(\frac{2\pi i y}{\lambda}\right),$$
$$\text{and} \quad \frac{\partial V_1}{\partial y} = \hat{V}_1' \exp(st) \exp\left(\frac{2\pi i y}{\lambda}\right),$$

with $\mathcal{A} = 1 + f_T(T_0 - T_{\text{amb}})/f_0 = f(\dot{\gamma}_0, T_0)/f_0$ and $\mathcal{B} = f_T(\sigma_N - p_0)/(f_0\Lambda)$. The perturbed governing equations can be rewritten in a compact matrix form, and the solution to the equations above exists if the determinant is zero, which is

$$s^2 + \left[\mathcal{A}(\mathcal{B} - \mathcal{A})H\frac{f_0}{f_{\dot{\gamma}}} + \frac{4\pi^2(\alpha_{\text{th}} + \alpha_{\text{hy}})}{\lambda^2}\right] s + \frac{16\pi^4\alpha_{\text{th}}\alpha_{\text{hy}}}{\lambda^4} + \frac{4\pi^2\alpha_{\text{hy}}H f_0\mathcal{A}\mathcal{B}}{f_{\dot{\gamma}}\lambda^2} = 0. \quad \text{(B.9)}$$

In stable cases, the real part of s is negative and the perturbations decay with time. If the quadratic equation has real roots, the same system can evolve into two different results, one stable, and the other one unstable. If the equation has complex root, the real part is

$$\Re(s) = \mathcal{A}(\mathcal{A} - \mathcal{B})H\frac{f_0}{2f_{\dot{\gamma}}} - \frac{2\pi^2(\alpha_{\text{th}} + \alpha_{\text{hy}})}{\lambda^2},$$

and since $\sigma_{\text{n}} - p_0(t) = \bar{\sigma}_{\text{n}} \exp(-t/\tau_p)$, $\Re(s) = -1/\tau_p = -\mathcal{A}H\dot{\gamma}_0$. Therefore the critical wavelength is

$$\lambda_{\text{cr}} = 2\pi\sqrt{\frac{\alpha_{\text{th}} + \alpha_{\text{hy}}}{\mathcal{A}H\left[\frac{f_0}{f_{\dot{\gamma}}}(\mathcal{A} - \mathcal{B})\right] + 2\dot{\gamma}_0}}.$$

In the case of uniform shearing, $\dot{\gamma}_0 = V/w_{\mathrm{cr}}$, and $w_{\mathrm{cr}} = \lambda_{\mathrm{cr}}$. The friction is assumed to depend on the slip rate, so

$$f_{\dot{\gamma}} = \frac{\mathrm{d}f}{\mathrm{d}V}\frac{\mathrm{d}V}{\mathrm{d}\dot{\gamma}} \approx \frac{V}{\dot{\gamma}_0}\frac{\mathrm{d}f}{\mathrm{d}V} = w_{\mathrm{cr}}\frac{\mathrm{d}f}{\mathrm{d}V},$$

and the critical thickness can be simplified as

$$w_{\mathrm{cr}} \approx \frac{4\pi^2\rho c(\alpha_{\mathrm{hy}} + \alpha_{\mathrm{th}})}{f\Lambda\left(2V\dfrac{\mathrm{d}f}{\mathrm{d}V} + f - \dfrac{\mathrm{d}f}{\mathrm{d}T}\dfrac{\sigma_{\mathrm{n}} - p_0}{\Lambda}\right)}\frac{\mathrm{d}f}{\mathrm{d}V}. \tag{B.10}$$

B.2. Numerical method

To simplify the calculation, the pore pressure p and temperature T are first normalized to

$$\tilde{T} = \Lambda\frac{T - T_0}{\sigma_{\mathrm{n}} - p_0}, \quad \text{and} \quad \tilde{p} = \frac{p - p_0}{\sigma_{\mathrm{n}} - p_0},$$

so that the normalized governing equations are

$$\begin{aligned}\frac{\partial\tilde{p}}{\partial t} &= \alpha_{\mathrm{hy}}\frac{\partial^2\tilde{p}}{\partial y^2} + \frac{\partial\tilde{T}}{\partial t},\\ \frac{\partial\tilde{T}}{\partial t} &= \alpha_{\mathrm{th}}\frac{\partial^2\tilde{T}}{\partial y^2} + \frac{\Lambda f\dot{\gamma}}{\rho C}(1 - \tilde{p}).\end{aligned} \tag{B.11}$$

And the strain rate distribution satisfies $\dot{\gamma}|_{|y|>w/2} \to 0$. The initial conditions are

$$\tilde{T} = 0, \quad \tilde{p} = 0,$$

and the boundary conditions are

$$\left.\frac{\partial\tilde{T}}{\partial y}\right|_{\tilde{y}=0} = 0, \quad \left.\frac{\partial\tilde{p}}{\partial y}\right|_{\tilde{y}=0} = 0, \qquad \tilde{T}|_{y\to\infty} = 0, \quad \text{and} \quad \tilde{p}|_{y\to\infty} = 0.$$

From these equations, we further use a scaling transform $\xi = 2y/w$ and $\tau = t$ to fix the moving boundary, then apply centered difference to the transformed space. The transformed equations are

$$\begin{aligned}\frac{\partial \tilde{p}}{\partial \tau} &= \frac{4\alpha_{\mathrm{hy}}}{w^2}\frac{\partial^2 \tilde{p}}{\partial \xi^2} + \frac{\partial \tilde{T}}{\partial \tau} + \xi\Gamma\left(\frac{\partial \tilde{p}}{\partial \xi} - \frac{\partial \tilde{T}}{\partial \xi}\right),\\ \frac{\partial \tilde{T}}{\partial \tau} &= \frac{4\alpha_{\mathrm{th}}}{w^2}\frac{\partial^2 \tilde{T}}{\partial \xi^2} + \xi\Gamma\frac{\partial \tilde{T}}{\partial \xi} + \frac{\Lambda f \dot{\gamma}}{\rho C}(1-\tilde{p}),\end{aligned} \tag{B.12}$$

where $\Gamma = (1/w)\mathrm{d}w/\mathrm{d}\tau$ is the relative broadening rate of the shear zone.

The equations are discretized by using centered difference for the space, and we solve for the discretized temperature and pressure through time using the `ode` toolbox in Matlab. This enables the value of r to be tracked to impose the Mohr–Coulomb criterion $r = r_c$ on the shear zone boundary from equation (III.25) and determine its evolving width w. The strain rate $\dot{\gamma}$ is assumed to follow the Gaussian distribution in equation (III.27) or the uniform distribution approximated by equation (III.26).

B.3. Equivalent boundary of shearing

The thickness predicted by this model and the linear stability analysis is actually an "equivalent boundary", so is the result of Brantut and Sulem (2012). The pattern of the result $w \sim t$ curve resembles the prediction of other models (e.g., Brantut and Sulem, 2012; Rempel, 2006). The equivalent boundary is a function of state variables, such as the temperature, pore pressure, chemical potential, sliding time, etc., which are used to describe the sliding fault. The similarities may come from the reaction-diffusion system itself.

From the perspective of dimensional analysis, the Buckingham Pi theorem (Middleton and Wilcock, 1994) states that a physical problem can be cast in dimensionless form as

$$\psi = F(\Pi_0, \Pi_1, \ldots, \Pi_n), \tag{B.13}$$

where ψ is a physical state variable, and $\Pi_0,\ \Pi_1, \ldots,\ \Pi_n$ are dimensionless.

If we let $\Pi_0 = l/\sqrt{\alpha_{\text{th}} t}$ where l is a characteristic length scale, and eliminate t using $t \sim l^2/\alpha_{\text{th}}$ in the remaining dimensionless parameters, then the intermediate asymptotic behavior tells whether the problem becomes steady as $t \to \infty$. Barenblatt and Zel'Dovich (1972) pointed out that there are three categories of asymptotic behavior with $\Pi_0 \to 0$. The first one has nonsingular F and well defined $F(0, \Pi_1, \ldots, \Pi_n)$ at $\Pi_0 = 0$, which will lead to steady state. In the second case, the problem becomes singular as $\Pi_0 \to 0$

$$\psi \sim \Pi_0^{-\alpha} G\left(\frac{\Pi_1}{\Pi_0^{\alpha_1}}, \ldots, \frac{\Pi_n}{\Pi_0^{\alpha_n}}\right), \tag{B.14}$$

where the exponents cannot be determined by dimensional analysis. There are also possibilities not included in the two cases above, but they are not for reaction-diffusion systems. We argue that even for the asymptotic behavior of the second kind, if the system is bounded, the problem still becomes steady as time goes.

Following the typical self-similar transform, we assume the solution of the equations

$$\begin{cases} \dfrac{\partial \psi}{\partial t} & = \kappa \dfrac{\partial^2 \psi}{\partial x^2} + p(t, \psi) + q(t, x), \\ \psi|_{x \in \partial\Omega} & = 0 \quad \left(\text{or } \dfrac{\partial \psi}{\partial \nu}\Big|_{x \in \partial\Omega} = 0\right), \\ \psi|_{t = t_0} & = \psi_{t_0}(x), \end{cases} \tag{B.15}$$

can be expressed in the form

$$\psi = \frac{Q}{\sqrt{\kappa t}} F(\xi, \eta, \boldsymbol{\epsilon}), \quad \xi = \frac{x}{\sqrt{\kappa t}}, \quad \eta = \frac{l}{\sqrt{\kappa t}},$$

where $\boldsymbol{\epsilon}$ is a dimensionless matrix characterizing the variations in the material property in the region Ω. In the limit of $t \to \infty$, $\eta \to 0$, the dimensionless function F can be represented as

$$F(\xi, \eta, \boldsymbol{\epsilon}) = \eta^{\alpha} f(\xi, \boldsymbol{\epsilon}) + O(\eta^{\alpha}),$$

where $O(\eta^{\alpha})$ means higher order infinitesimal or lower order infinitesimal depending on the sign of α. The asymptotic form of the solution can be written as

$$\psi = \frac{Q l^{\alpha}}{(\kappa t)^{(1+\alpha)/2}} f(\xi, \boldsymbol{\epsilon}), \tag{B.16}$$

where the exponent α depends on $\boldsymbol{\epsilon}$. If $\alpha < -1$, ψ will grow to infinity as $t \to \infty$, which is not bounded. So for models where the state variables ψ satisfy equations (B.15) it must be $\alpha \geq -1$, and ψ will evolve towards steady state as $t \to \infty$, which means that any new variable w calculated from the state variables will also converge to a steady state, either a finite thickness or zero.

B.4. Significance of advection

One hidden assumption for the energy conservation equation (III.7) to hold is that the advection of heat is negligible compared to the conduction. This is true when the permeability of the shear zone is low, but whether advection can still be ignored when we put the ratio of $\alpha_{\mathrm{hy}}/\alpha_{\mathrm{th}}$ to 500 requires a more careful examination. The heat advection rate in the fluid is

$$q_a \sim q_{\mathrm{f}} C_{\mathrm{f}} \Delta T \sim -\frac{\rho_{\mathrm{f}} k C_{\mathrm{f}} \Delta T}{\eta_{\mathrm{f}}} \frac{\Delta p}{\Delta y} = -\rho_{\mathrm{f}} \alpha_{\mathrm{hy}} n \beta (\sigma_{\mathrm{n}} - p_0) C_{\mathrm{f}} \frac{\Delta T}{\Delta y},$$

while the heat conduction rate is

$$q_h \sim -K\frac{\Delta T}{\Delta y} = -\rho_s C_s \alpha_{th}\frac{\Delta T}{\Delta y},$$

where the subscript s denotes the properties of the shear zone. Let $q_a/q_h \ll 1$, we have

$$\alpha_{hy}/\alpha_{th} \ll \frac{\rho_s C_s}{n\rho_f C_f \beta(\sigma_n - p_0)},$$

and if we take the porosity n as 5% – 10%, the ratio is at least 1650, which means that for our model, as long as $\alpha_{hy} \ll 1650\,\alpha_{th}$, the advection of heat is not important.

APPENDIX C

FINITE ELEMENT MODELING OF CASCADIA SUBDUCTION ZONE: A TECHNICAL MEMOIR

This appendix contains the technical details of the dataset and modeling scheme of my project of modeling the Cascadia subduction zone. The aim is to simulate the interseismic deformation of Juan de Fuce plate from the ridge to the Basin and Range, and study the stress variation at the subduction interface with the geodetic observations as constraints.

C.1. Geometry and Material Properties of the Model

Recent results from seismic imaging and tomography that focused on the subducted oceanic lithosphere helped to identify the geometry of the slab interface. We build our model using data from seismicity, seismic imaging, and tomography.

Our model covers a region of 2000 km by 1000 km by 400 km, containing most of the Juan de Fuca plate and extending to the Basin and Range (see Figure C.1).

For the shallow part of the subduction slab, McCrory et al. (2012) compiled the data from seismic imaging and seismicity and produced a detailed contour map of the slab down to 100 km (Figure C.2). This is the place containing the locked portion of the fault.

The deeper section of the slab is constrained using tomography data. Specifically,

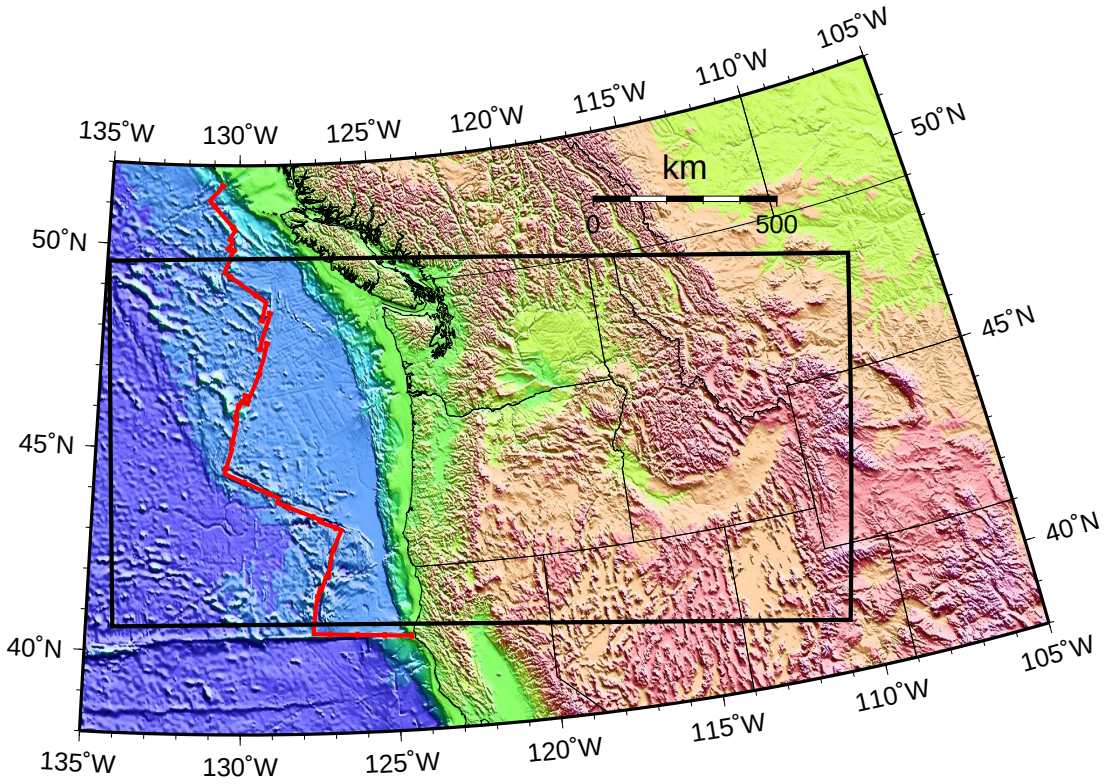

Figure C.1: The region covered in our model.

Schmandt and Humphreys (2010) used body wave tomography to study the upper mantle of the western United States. Although at large depth (~ 400 km), the slab only shows as discontinous fragments and the boundary is blurred due t thermal diffusion, the tomography indicates the approximate location of the slab (Figure C.3).

We simplified the oceanic lithosphere before it meets the trench as a sheet with constant thickness. The thickness is scaled with the slab age (pp. 317, Turcotte and Schubert, 2014)

$$y_T \sim 2.32\sqrt{\kappa t}, \tag{C.1}$$

where $\kappa \sim 1$ mm^{2}s^{-1} is the thermal diffusivity, and t is the age of the slab. From Wilson (2002), the age of slab when the trench starts is around 10 Ma (Figure C.1), so the thickness of oceanic lithosphere at the trench is approximately 40 km.

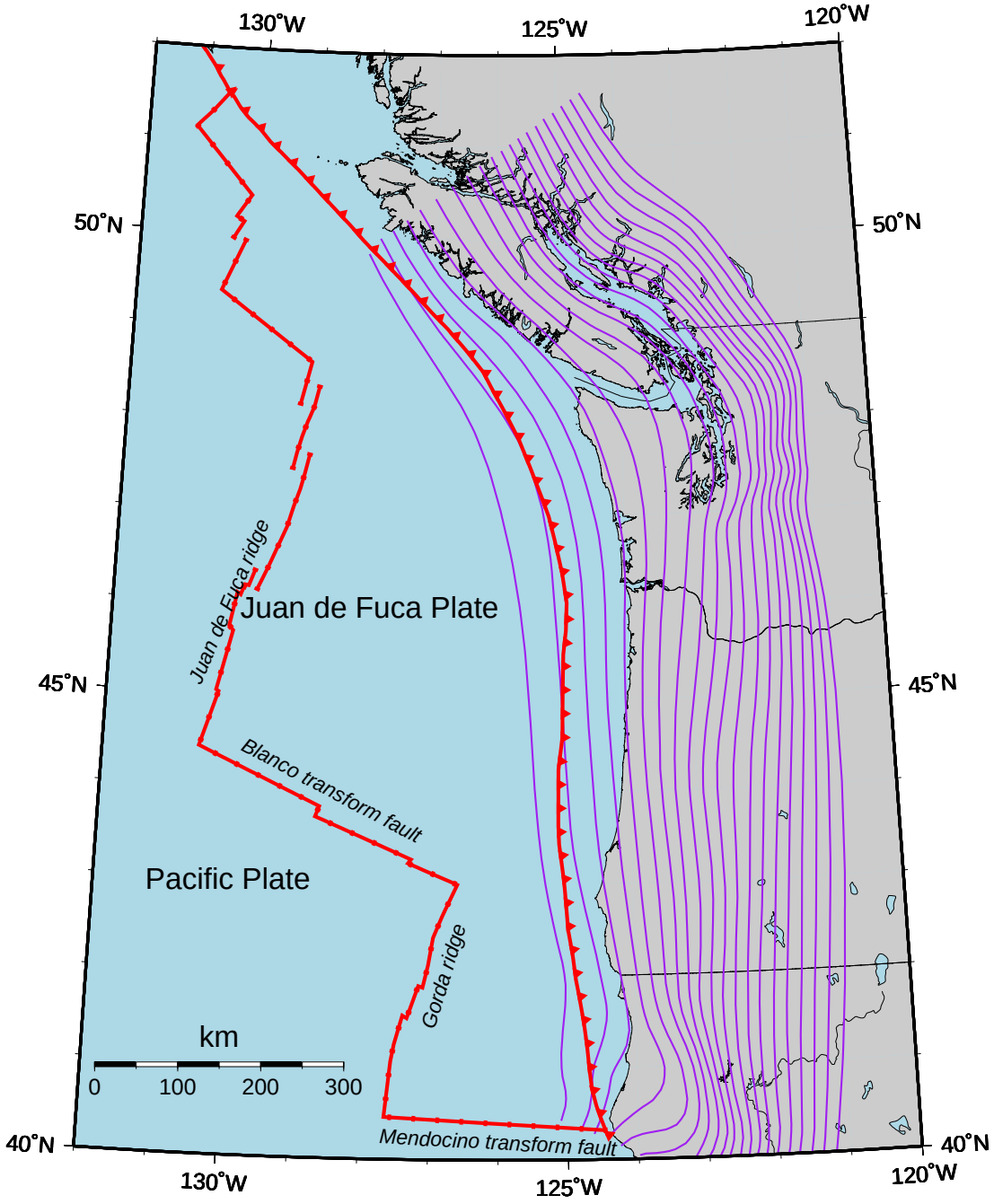

Figure C.2: The contour of Cascadia slab. The contours start at 5 km depth, with an interval of 5 km (McCrory et al., 2012).

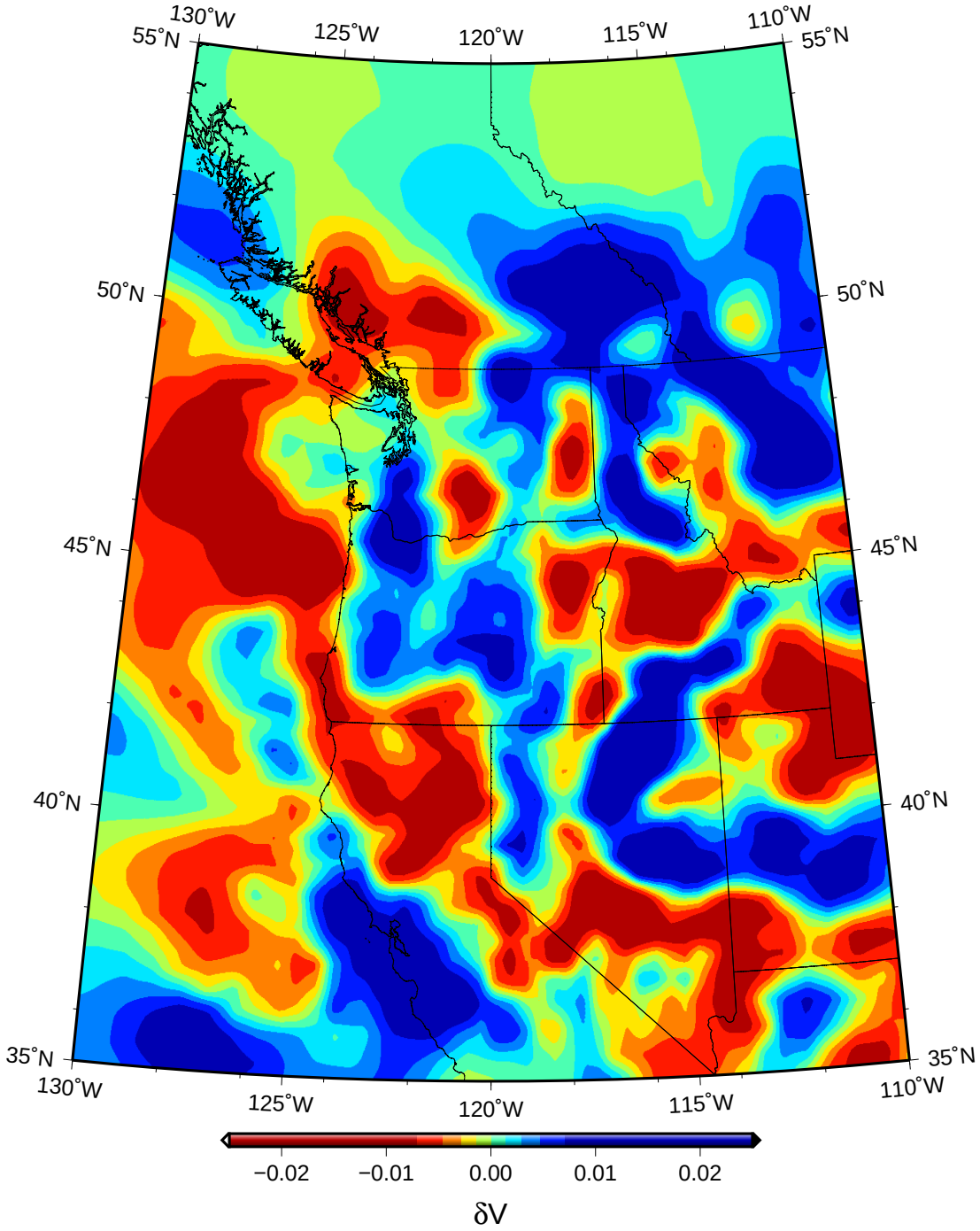

Figure C.3: The tomography of Cascadia slab at 435 km depth from Schmandt and Humphreys (2010). The high velocity region beneath Oregon and Washington is where the slab locates.

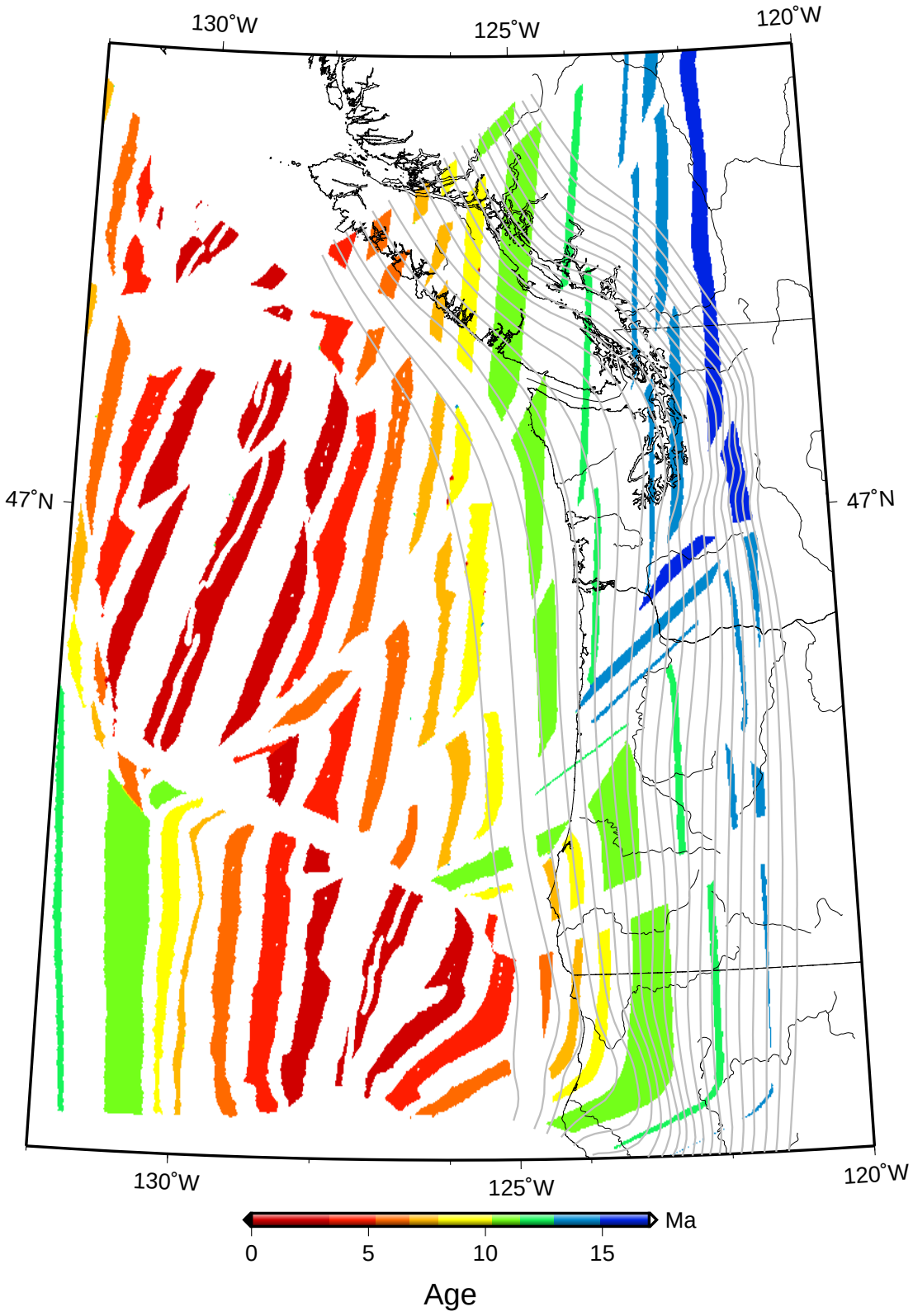

Figure C.4: The age of the seafloor and Cascadia slab. The age data is from Wilson (2002).

On the continent, we constrain the lithosphere thickness using the lithosphere-asthenosphere boundary data from Levander and Miller (2012).

The datasets are used to construct a geometry model in Cubit (Figure C.6).

Due to the irregular geometry, we choose to mesh the model using tetrahedral elements. In the subduction wedge, the mesh size is 10 km, and toward the edge of the model, the mesh becomes sparse with a bias factor of 1.2 (Figure C.7)

C.2. Finite element modeling

The material properties we use in our model also come from tomography results. The elastic properties of continental and oceanic lithosphere are from the work of Gao et al. (2011), and the continental and oceanic mantle are modeled as homogeneous, isotropic, and viscoelastic, which can be changed to other viscoelastic relationships if needed.

We use the finite element package Pylith to simulate the interseismic deformation of the subduction zone for a time frame of 300 years. Pylith uses cohesive cells to implement displacement across faults, and provides several linear and nonlinear solvers depending on the problem type. In our model, we use geometric algebraic multigrid (GAMG) preconditioning of the displacement sub-block with a full Schur complement factorization using the PETSc FieldSplit preconditioner.

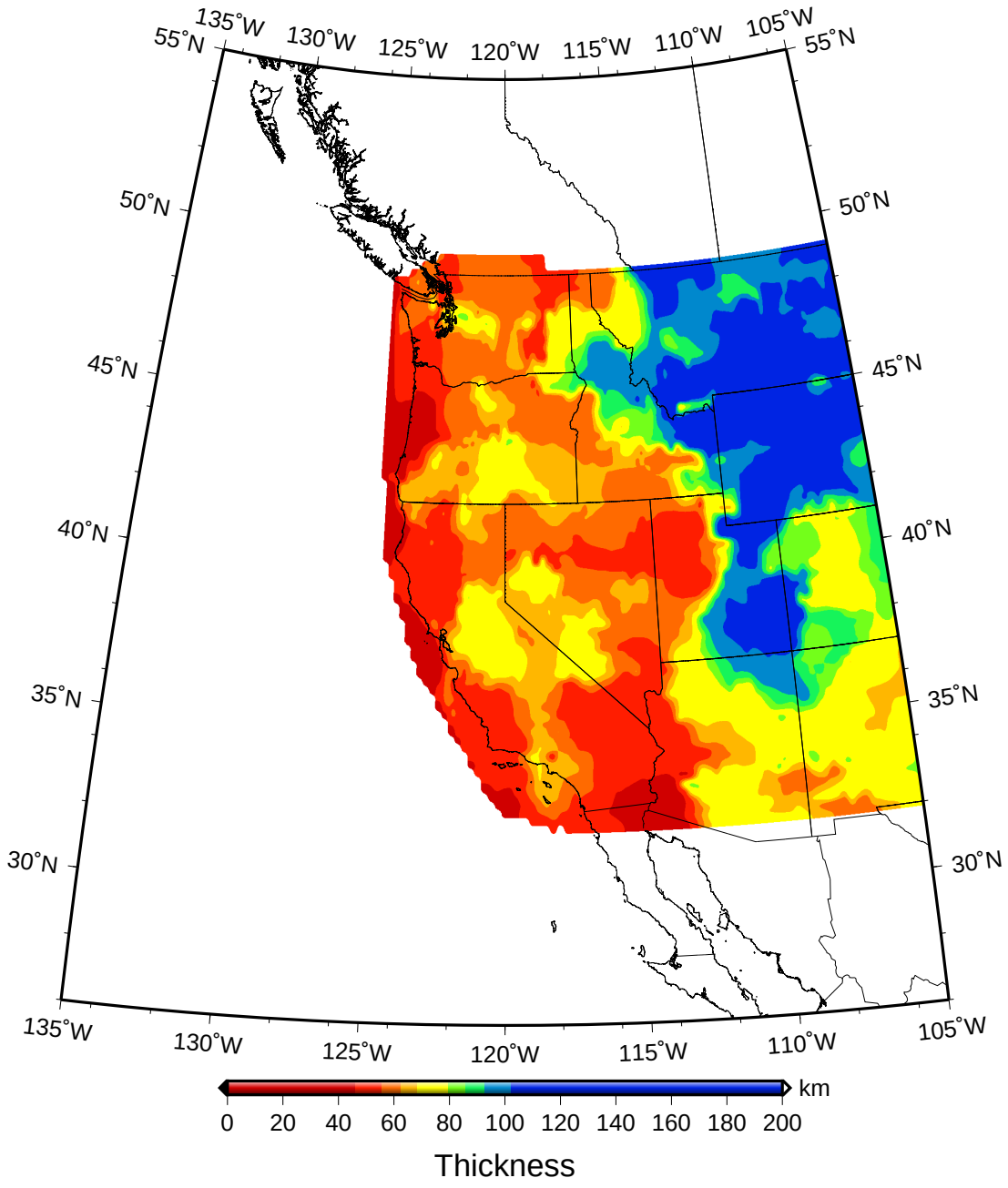

Figure C.5: The lithosphere-asthenosphere boundary depth in the western United States. The data is from Levander and Miller (2012).

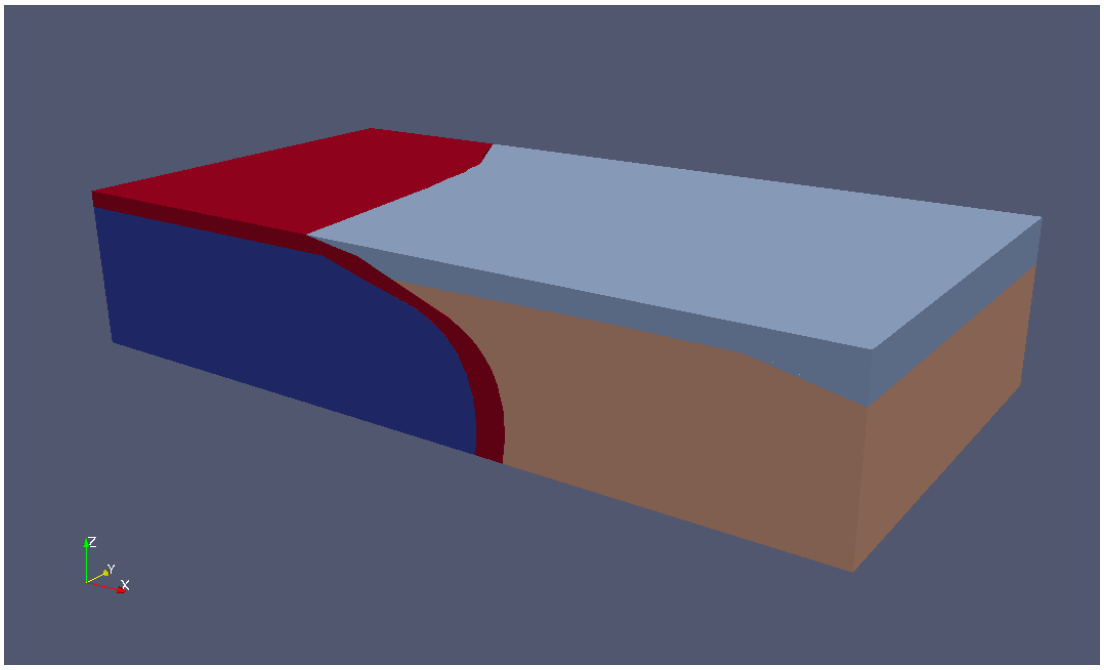

Figure C.6: The geometry model of the subduction zone.

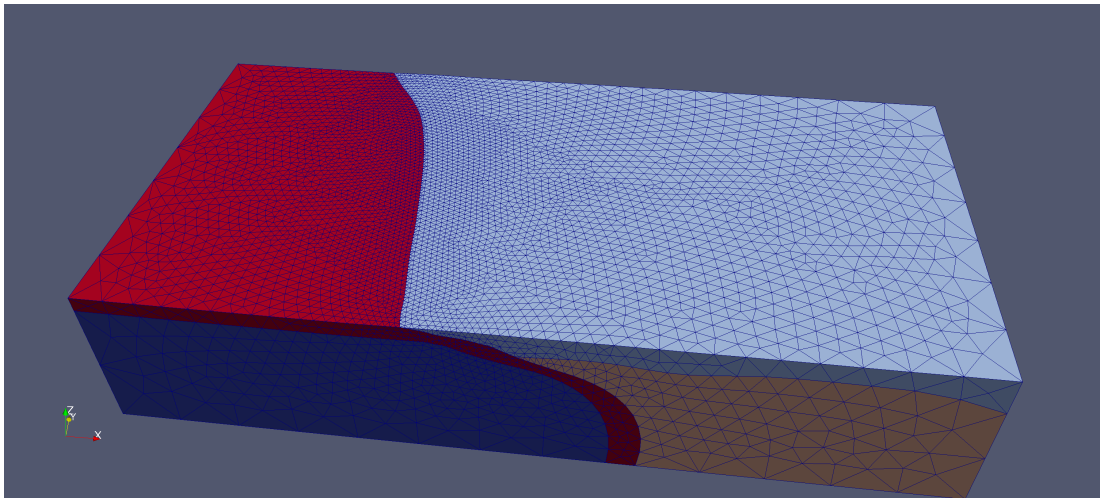

Figure C.7: The mesh of the subduction zone. Near the wedge, the mesh is dense with a size of 10 km, and the mesh size increases as it progresses far from the wedge.

REFERENCES CITED

Abe, S. and Mair, K. (2009). Effects of gouge fragment shape on fault friction: New 3d modelling results. *Geophys. Res. Lett.*, 36:L23302–.

Archard, J. (1959). The temperature of rubbing surfaces. *Wear*, 2(6):438–455.

Barenblatt, G. and Zel'Dovich, Y. B. (1972). Self-similar solutions as intermediate asymptotics. *Annual Review of Fluid Mechanics*, 4(1):285–312.

Beeler, N. M., Tullis, T. E., and Goldsby, D. L. (2008). Constitutive relationships and physical basis of fault strength due to flash heating. *J. Geophys. Res. Solid Earth*, 113(B1):B01401.

Ben-Zion, Y. and Sammis, C. G. (2003). Characterization of fault zones. *Pure Appl. Geophys.*, 160(3-4):677–715.

Blanpied, M. L., Lockner, D. A., and Byerlee, J. D. (1995). Frictional slip of granite at hydrothermal conditions. *J. Geophys. Res.*, 100(B7):13045–13064.

Boullier, A.-M., Yeh, E.-C., Boutareaud, S., Song, S.-R., and Tsai, C.-H. (2009). Microscale anatomy of the 1999 chi-chi earthquake fault zone. *Geochemistry, Geophysics, Geosystems*, 10(3):Q03016–.

Bowden, F. and Tabor, D. (1950). *The friction and lubrication of solids*, volume 1. Clarendon Press, Oxford.

Bowden, F. P. and Thomas, P. H. (1954). The surface temperature of sliding solids. *Proceedings of the Royal Society of London. Series A. Mathematical and Physical Sciences*, 223(1152):29–40.

Brace, W. F. and Kohlstedt, D. L. (1980). Limits on lithospheric stress imposed by laboratory experiments. *J. Geophys. Res.*, 85(B11):6248–6252.

Brantut, N., Schubnel, A., Corvisier, J., and Sarout, J. (2010). Thermochemical pressurization of faults during coseismic slip. *J. Geophys. Res.*, 115(B5):B05314–.

Brantut, N. and Sulem, J. (2012). Strain localization and slip instability in a strain-rate hardening, chemically weakening material. *J. Appl. Mech.*, 79(3):031004–10.

Brown, K. and Fialko, Y. (2009). Friction and plasticity at seismic slip speeds: Experiments and theory. In *Eos, Transactions American Geophysical Union, Fall Meeting Supplement*, volume 90, page 52.

Brown, K. M. and Fialko, Y. (2012). 'melt welt' mechanism of extreme weakening of gabbro at seismic slip rates. *Nature*, 488(7413):638–641.

Broz, M. E., Cook, R. F., and Whitney, D. L. (2006). Microhardness, toughness, and modulus of mohs scale minerals. *American Mineralogist*, 91(1):135–142.

Candela, T., Brodsky, E. E., Marone, C., and Elsworth, D. (2014). Laboratory evidence for particle mobilization as a mechanism for permeability enhancement via dynamic stressing. *Earth Planet. Sci. Lett.*, 392(0):279–291.

Carslaw, H. S. and Jaeger, J. C. (1959). *Conduction of heat in solids*. Oxford University Press, New York, 2nd edition.

Chen, J. and Rempel, A. W. (2014). Progressive flash heating and the evolution of high-velocity rock friction. *J. Geophys. Res. Solid Earth*, 119(4):3182–3200.

Chester, F., Chester, J., Kirschner, D., Schulz, S., and Evans, J. (2004). Structure of large-displacement, strike-slip fault zones in the brittle continental crust. In *Rheology and Deformation in the Lithosphere at Continental Margins*, pages 223–260. Columbia University Press.

Chester, F. M. and Chester, J. S. (1998). Ultracataclasite structure and friction processes of the punchbowl fault, san andreas system, california. *Tectonophysics*, 295(1-2):199–221.

Chester, F. M., Evans, J. P., and Biegel, R. L. (1993). Internal structure and weakening mechanisms of the san andreas fault. *J. Geophys. Res. Solid Earth*, 98(B1):771–786.

Chester, J. S., Kronenberg, A. K., Chester, F. M., and Guillemette, R. N. (2003). Characterization of natural slip surfaces relevant to earthquake mechanics. In *Eos, Transactions American Geophysical Union, Fall Meeting Supplement*, page C185.

Clauser, C. and Huenges, E. (1995). Thermal conductivity of rocks and minerals. In *Rock Physics & Phase Relations*, pages 105–126. American Geophysical Union.

Cowan, D. S. (1999). Do faults preserve a record of seismic slip? a field geologist's opinion. *J. Struct. Geol.*, 21(8-9):995–1001.

Daniels, K. E. and Hayman, N. W. (2008). Force chains in seismogenic faults visualized with photoelastic granular shear experiments. *J. Geophys. Res. Solid Earth*, 113(B11):B11411.

Del Gaudio, P., Di Toro, G., Han, R., Hirose, T., Nielsen, S., Shimamoto, T., and Cavallo, A. (2009). Frictional melting of peridotite and seismic slip. *J. Geophys. Res. Solid Earth*, 114:B06306.

den Hartog, S., Niemeijer, A., and Spiers, C. (2012). New constraints on megathrust slip stability under subduction zone p-t conditions. *Earth Planet. Sci. Lett.*, 353–354(0):240–252.

Di Toro, G., Goldsby, D. L., and Tullis, T. E. (2004). Friction falls towards zero in quartz rock as slip velocity approaches seismic rates. *Nature*, 427(6973):436–439.

Di Toro, G. and Pennacchioni, G. (2004). Superheated friction-induced melts in zoned pseudotachylytes within the adamello tonalites (italian southern alps). *J. Struct. Geol.*, 26(10):1783–1801.

Dieterich, J. H. (1981). Constitutive properties of faults with simulated gouge. In *Mechanical Behavior of Crustal Rocks, Geophys. Monogr. Ser.*, volume 24, pages 103–120. American Geophysical Union, Washington, DC.

Dieterich, J. H. (1994). A constitutive law for rate of earthquake production and its application to earthquake clustering. *J. Geophys. Res. Solid Earth*, 99(B2):2601–2618.

Dieterich, J. H. and Kilgore, B. D. (1994). Direct observation of frictional contacts—new insights for state-dependent properties. *Pure Appl. Geophys.*, 143(1–3):283–302.

Erismann, T., Heuberger, H., and Preuss, E. (1977). Der bimsstein von kÃűfels (tirol), ein bergsturz-âĂIJfriktionitâĂİ. *Tschermaks Mineral. Petrogr. Mitt.*, 24(1–st2):67–119.

Evans, J. P., Forster, C. B., and Goddard, J. V. (1997). Permeability of fault-related rocks, and implications for hydraulic structure of fault zones. *J. Struct. Geol.*, 19(11):1393–1404.

Faulkner, D. and Armitage, P. (2013). The effect of tectonic environment on permeability development around faults and in the brittle crust. *Earth Planet. Sci. Lett.*, 375(0):71–77.

Fulton, P. M., Brodsky, E. E., Kano, Y., Mori, J., Chester, F., Ishikawa, T., Harris, R. N., Lin, W., Eguchi, N., Toczko, S., Expedition 343, T., and Scientists, K.-. (2013). Low coseismic friction on the tohoku-oki fault determined from temperature measurements. *Science*, 342(6163):1214–1217.

Gao, H., Humphreys, E. D., Yao, H., and van der Hilst, R. D. (2011). Crust and lithosphere structure of the northwestern u.s. with ambient noise tomography: Terrane accretion and cascade arc development. *Earth Planet. Sci. Lett.*, 304(1–2):202–211.

Garagash, D. I. and Germanovich, L. N. (2012). Nucleation and arrest of dynamic slip on a pressurized fault. *J. Geophys. Res.*, 117(B10):B10310–.

Ghabezloo, S. and Sulem, J. (2009). Stress dependent thermal pressurization of a fluid-saturated rock. *Rock Mech. Rock Engng.*, 42(1):1–24.

Goldsby, D. L. and Tullis, T. E. (2002). Low frictional strength of quartz rocks at subseismic slip rates. *Geophys. Res. Lett.*, 29(17):1844–.

Goldsby, D. L. and Tullis, T. E. (2011). Flash heating leads to low frictional strength of crustal rocks at earthquake slip rates. *Science*, 334(6053):216–218.

Han, R., Hirose, T., Shimamoto, T., Lee, Y., and Ando, J.-i. (2011). Granular nanoparticles lubricate faults during seismic slip. *Geology*, 39(6):599–602.

Henyey, T. L. and Wasserbu, G. J. (1971). Heat flow near major strike-slip faults in california. *J. Geophys. Res.*, 76(32):7924–7946.

Hirose, T. and Shimamoto, T. (2003). Fractal dimension of molten surfaces as a possible parameter to infer the slip-weakening distance of faults from natural pseudotachylytes. *J. Struct. Geol.*, 25(10):1569–1574.

Hirose, T. and Shimamoto, T. (2005). Growth of molten zone as a mechanism of slip weakening of simulated faults in gabbro during frictional melting. *J. Geophys. Res. Solid Earth*, 110(B5):B05202.

Hirth, G. and Kohlstedt, D. (2003). Rheology of the upper mantle and the mantle wedge: A view from the experimentalists. In *Geophys. Monogr. Ser.*, volume 138, pages 83–105. American Geophysical Union, Washington, DC.

Holland, T. H. (1900). *The Charnockite Series: A Group of Archæan Hypersthenic Rocks in Peninsular India*, volume 28, chapter Part 2. Geological Survey of India, Calcutta.

Hui, H. and Zhang, Y. (2007). Toward a general viscosity equation for natural anhydrous and hydrous silicate melts. *Geochim. Cosmochim. Acta*, 71(2):403–416.

Kanamori, H., Fujii, N., and Mizutani, H. (1968). Thermal diffusivity measurement of rock-forming minerals from 300Âř to 1100Âřk. *J. Geophys. Res.*, 73(2):595–605.

Kirkpatrick, J. D. and Rowe, C. D. (2013). Disappearing ink: How pseudotachylytes are lost from the rock record. *J. Struct. Geol.*, 52(0):183–198.

Kobranova, V. N. (1990). *Petrophysics*. New York, NY (USA); Springer-Verlag New York Inc.

Kohli, A. H., Goldsby, D. L., Hirth, G., and Tullis, T. (2011). Flash weakening of serpentinite at near-seismic slip rates. *J. Geophys. Res.*, 116(B3):B03202–.

Kuo, L.-W., Song, S.-R., Huang, L., Yeh, E.-C., and Chen, H.-F. (2011). Temperature estimates of coseismic heating in clay-rich fault gouges, the chelungpu fault zones, taiwan. *Tectonophysics*, 502(3-4):315–327.

Kuwano, O. and Hatano, T. (2011). Flash weakening is limited by granular dynamics. *Geophys. Res. Lett.*, 38(17):L17305–.

Lachenbruch, A. H. (1980). Frictional heating, fluid pressure, and the resistance to fault motion. *J. Geophys. Res.*, 85(B11):6097–6112.

Lachenbruch, A. H. and Sass, J. H. (1980). Heat flow and energetics of the san andreas fault zone. *J. Geophys. Res.*, 85(B11):6185–6222.

Lachenbruch, A. H. and Sass, J. H. (1992). Heat flow from cajon pass, fault strength, and tectonic implications. *J. Geophys. Res.*, 97(B4):4995–5015.

Levander, A. and Miller, M. S. (2012). Evolutionary aspects of lithosphere discontinuity structure in the western u.s. *Geochemistry, Geophysics, Geosystems*, 13(7):Q0AK07–.

Lockner, D., Naka, H., Tanaka, H., Ito, H., and Ikeda, R. (2000). Permeability and strength of core samples from the nojima fault of the 1995 kobe earthquake. In H. Ito, K. Fujimoto, H. T. and Lockner, D., editors, *Proceedings of the international workshop on the Nojima fault core and borehole data analysis*, pages 22–23. US Geol. Sur.

Logan, J. and Teufel, L. (1986). The effect of normal stress on the real area of contact during frictional sliding in rocks. *Pure Appl. Geophys.*, 124(3):471–485–.

Mair, K. and Abe, S. (2008). 3d numerical simulations of fault gouge evolution during shear: Grain size reduction and strain localization. *Earth Planet. Sci. Lett.*, 274(1-2):72–81.

Mair, K. and Marone, C. (2000). Shear heating in granular layers. *Pure Appl. Geophys.*, 157(11-12):1847–1866.

Marone, C. J., Scholtz, C. H., and Bilham, R. (1991). On the mechanics of earthquake afterslip. *J. Geophys. Res.*, 96(B5):8441–8452.

McCrory, P. A., Blair, J. L., Waldhauser, F., and Oppenheimer, D. H. (2012). Juan de fuca slab geometry and its relation to wadati-benioff zone seismicity. *J. Geophys. Res.*, 117(B9):B09306–.

Middleton, G. V. and Wilcock, P. R. (1994). *Mechanics in the Earth and Environmental Sciences*. Cambridge University Press, Cambridge.

Mizoguchi, K., Hirose, T., Shimamoto, T., and Fukuyama, E. (2008). Internal structure and permeability of the nojima fault, southwest japan. *J. Struct. Geol.*, 30(4):513–524.

Morgenstern, N. and Tchalenko, J. (1967). Microscopic structures in kaolin subjected to direct shear. *Geotechnique*, 17(4):309–328.

Muir Wood, D. (2002). Some observations of volumetric instabilities in soils. *Int. J. Solids Struct.*, 39(13-14):3429–3449.

Noda, H. and Shimamoto, T. (2005). Thermal pressurization and slip-weakening distance of a fault: an example of the hanaore fault, southwest japan. *Bulletin of the Seismological Society of America*, 95(4):1224–1233.

Otsuki, K., Monzawa, N., and Nagase, T. (2003). Fluidization and melting of fault gouge during seismic slip: Identification in the nojima fault zone and implications for focal earthquake mechanisms. *J. Geophys. Res. Solid Earth*, 108(B4):2192.

Platt, J., Rice, J. R., and Rudnicki, J. W. (2010). Strain localization within a fluid-saturated fault gouge layer during seismic shear. In *Eos, Transactions American Geophysical Union, Fall Meeting Supplement*, volume 91, page D3.

Platt, J. D., Rudnicki, J. W., and Rice, J. R. (2014). Stability and localization of rapid shear in fluid-saturated fault gouge: 2. localized zone width and strength evolution. *J. Geophys. Res. Solid Earth*, 119(5):4334–4359.

Poliakov, A. N. B., Dmowska, R., and Rice, J. R. (2002). Dynamic shear rupture interactions with fault bends and off-axis secondary faulting. *J. Geophys. Res.*, 107(B11):2295–.

Pollastro, R. M. (1993). Considerations and applications of the illite/smectite geothermometer in hydrocarbon-bearing rocks of miocene to mississippian age. *Clays Clay Miner.*, 41(2):119–133.

Rempel, A. W. (2006). The effects of flash-weakening and damage on the evolution of fault strength and temperature. In *Radiated Energy and the Physics of Earthquake Faulting, Geophys. Monogr. Ser.*, volume 170, pages 263–270. American Geophysical Union.

Rempel, A. W. and Rice, J. R. (2006). Thermal pressurization and onset of melting in fault zones. *J. Geophys. Res. Solid Earth*, 111(B9):B09314.

Rempel, A. W. and Weaver, S. L. (2008). A model for flash weakening by asperity melting during high-speed earthquake slip. *J. Geophys. Res. Solid Earth*, 113(B11):B11308.

Rice, J. (1980). The mechanics of earthquake rupture. In Dziewonski, A. and Boschi, E., editors, *Physics of the Earth's Interior*, pages 555–649. Italian Physical Society, North-Holland, New York.

Rice, J., Rudnicki, J., and Tsai, V. (2005a). Shear localization in fluid-saturated fault gouge by instability of spatially uniform, adiabatic, undrained shear. In *Eos, Transactions American Geophysical Union, Fall Meeting Supplement*, volume 86, page E5.

Rice, J. R. (1999). Flash heating at asperity contacts and rate-dependent friction. In *Eos, Transactions American Geophysical Union, Fall Meeting Supplement*, volume 80, page F471.

Rice, J. R. (2006). Heating and weakening of faults during earthquake slip. *J. Geophys. Res. Solid Earth*, 111(B5):B05311.

Rice, J. R., Rudnicki, J. W., and Platt, J. D. (2014). Stability and localization of rapid shear in fluid-saturated fault gouge: 1. linearized stability analysis. *J. Geophys. Res. Solid Earth*, 119(5):4311–4333.

Rice, J. R., Sammis, C. G., and Parsons, R. (2005b). Off-fault secondary failure induced by a dynamic slip pulse. *Bulletin of the Seismological Society of America*, 95(1):109–134.

Robertson, E. C. (1988). *Thermal properties of rocks*. US Department of the Interior, Geological Survey, Reston, Virginia.

Robie, R. A. and Hemingway, B. S. (1995). Thermodynamic properties of minerals and related substances at 298.15 K and 1 bar (10^5 Pascals) pressure and at higher temperatures. *U.S. Geol. Surv. Bull.*, 2131:461pp.

Rowe, C. D., Fagereng, Ã., Miller, J. A., and Mapani, B. (2012). Signature of coseismic decarbonation in dolomitic fault rocks of the naukluft thrust, namibia. *Earth Planet. Sci. Lett.*, 333-334(0):200–210.

Schmandt, B. and Humphreys, E. (2010). Complex subduction and small-scale convection revealed by body-wave tomography of the western united states upper mantle. *Earth Planet. Sci. Lett.*, 297(3-4):435–445.

Scholz, C. H. (1988). The brittle-plastic transition and the depth of seismic faulting. *Geol. Rundsch.*, 77(1):319–328.

Scholz, C. H. (1998). Earthquakes and friction laws. *Nature*, 391(6662):37–42.

Schrank, C. E., Handy, M. R., and Fusseis, F. (2008). Multiscaling of shear zones and the evolution of the brittle-to-viscous transition in continental crust. *J. Geophys. Res.*, 113(B1):B01407–.

Scott, J. S. and Drever, H. I. (1954). Frictional fusion along a himalayan thrust. In *Proceedings of the Royal Society of Edinburgh Section B: Biological Sciences*, volume 65, pages 121–142.

Seront, B., Wong, T.-F., Caine, J. S., Forster, C. B., Bruhn, R. L., and Fredrich, J. (1998). Laboratory characterization of hydromechanical properties of a seismogenic normal fault system. *J. Struct. Geol.*, 20(7):865–881.

Sibson, R. (1973). Interactions between temperature and pore-fluid pressure during earthquake faulting and a mechanism for partial or total stress relief. *Nature*, 243(126):66–68.

Sirono, S., Satomi, K., and Watanabe, S. (2006). Numerical simulations of frictional melting: Small dependence of shear stress drop on viscosity parameters. *J. Geophys. Res. Solid Earth*, 111(B6):B06309.

Sone, H. and Shimamoto, T. (2009). Frictional resistance of faults during accelerating and decelerating earthquake slip. *Nature*, 2:705–708.

Spray, J. G. (1987). Artificial generation of pseudotachylyte using friction welding apparatus: simulation of melting on a fault plane. *J. Struct. Geol.*, 9(1):49–60.

Spray, J. G. (1988). Generation and crystallization of an amphibolite shear melt: an investigation using radial friction welding apparatus. *Contributions to Mineralogy and Petrology*, 99(4):464–475–.

Spray, J. G. (1993). Viscosity determinations of some frictionally generated silicate melts: Implications for fault zone rheology at high strain rates. *J. Geophys. Res.*, 98(B5):8053–8068.

Spray, J. G. (1995). Pseudotachylyte controversy: Fact or friction? *Geology*, 23(12):1119–1122.

Spray, J. G. (2005). Evidence for melt lubrication during large earthquakes. *Geophys. Res. Lett.*, 32(7):L07301–.

Spray, J. G. (2010). Frictional melting processes in planetary materials: From hypervelocity impact to earthquakes. *Annual Review of Earth and Planetary Sciences*, 38(1):221–254.

Stebbins, J. F., Carmichael, I. S. E., and Weill, D. E. (1983). The high temperature liquid and glass heat contents and the heats of fusion of diopside, albite, sanidine and nepheline. *American Mineralogist*, 68(7–8):717–730.

Terzaghi, K. v. (1936). The shearing resistance of saturated soils and the angle between the planes of shear. In *Proceedings of the 1st International Conference on Soil Mechanics and Foundation Engineering*, volume 1, pages 54–56.

Tsutsumi, A. and Shimamoto, T. (1997). High-velocity frictional properties of gabbro. *Geophys. Res. Lett.*, 24(6):699–702.

Turcotte, D. L. and Schubert, G. (2014). *Geodynamics*. Cambridge University Press.

Ujiie, K., Tanaka, H., Saito, T., Tsutsumi, A., Mori, J. J., Kameda, J., Brodsky, E. E., Chester, F. M., Eguchi, N., Toczko, S., 343, E., and Scientists, T. (2013). Low coseismic shear stress on the tohoku-oki megathrust determined from laboratory experiments. *Science*, 342(6163):1211–1214.

Ujiie, K. and Tsutsumi, A. (2010). High-velocity frictional properties of clay-rich fault gouge in a megasplay fault zone, nankai subduction zone. *Geophys. Res. Lett.*, 37(24):L24310–.

Viesca, R. C. and Rice, J. R. (2012). Nucleation of slip-weakening rupture instability in landslides by localized increase of pore pressure. *J. Geophys. Res.*, 117(B3):B03104–.

Wibberley, C. A. and Shimamoto, T. (2003). Internal structure and permeability of major strike-slip fault zones: the median tectonic line in mie prefecture, southwest japan. *J. Struct. Geol.*, 25(1):59–78.

Wibberley, C. A. J. (2002). Hydraulic diffusivity of fault gouge zones and implications for thermal pressurization during seismic slip:. *Earth Planets Space*, 54(11):1153–1171.

Wilson, D. S. (2002). The juan de fuca plate and slab: Isochron structure and cenozoic plate motions. In Stephen Kirby, K. W. and Dunlop, S., editors, *The Cascadia Subduction Zone and Related Subduction Systems — Seismic Structure, Intraslab Earthquakes and Processes, and Earthquake Hazards*, volume 2, page 9. US Geol. Surv. Open-File Rept.

Yuan, F. and Prakash, V. (2008a). Slip weakening in rocks and analog materials at co-seismic slip rates. *J. Mech. Phys. Solids*, 56(2):542–560.

Yuan, F. and Prakash, V. (2008b). Use of a modified torsional kolsky bar to study frictional slip resistance in rock-analog materials at coseismic slip rates. *Int. J. Solids Struct.*, 45(14–15):4247–4263.

Yuan, F. and Prakash, V. (2012). Laboratory observations of transient frictional slip in rock-analog materials at co-seismic slip rates and rapid changes in normal stress. *Tectonophysics*, 558–559(0):58–69.

Zoback, M. D., Zoback, M. L., Mount, V. S., Suppe, J., Eaton, J. P., Healy, J. H., Oppenheimer, D., Reasenberg, P., Jones, L., Raleigh, C. B., Wong, I. G., Scotti, O., and Wentworth, C. (1987). New evidence on the state of stress of the san-andreas fault system. *Science*, 238(4830):1105–1111.